Univerza v Ljubljani
Fakulteta za Matematiko in Fiziko

Doktorska Disertacija

Ruben Verheyden

2015

University of Ljubljana
Faculty of Mathematics and Physics
Department of Physics

Ruben Verheyden

Development of a PET Module with DOI Encoding Using Silicon Photomultipliers

Doctoral thesis

Advisor: Prof. Dr. Samo Korpar

Ljubljana, 2015

Univerza v Ljubljani
Fakulteta za Matematiko in Fiziko
Oddelek za Fiziko

Ruben Verheyden

Detektor PET s silicijevimio fotopomnoževalkami

Doktorska Disertacija

Mentor: Prof. Dr. Samo Korpar

Ljubljana, 2015

Izjava o avtorstvu in objavi elektronske oblike

Podpisani Ruben Verheyden izjavljam:

- da sem doktorsko disertacijo z naslovom *Detektor PET s silicijevimio fotopomnoževalkami* izdelal kot rezultat lastnega raziskovalnega dela pod mentorstvom prof. dr. Sama Korparja,
- da je elektronska oblika dela identična s tiskano obliko in
- da Fakulteti za matematiko in fiziko Univerze v Ljubljani dovoljujem objavo elektronske oblike svojega dela na spletnih straneh Repozitorija Univerze v Ljubljani.

Ljubljana, 9. julij 2015

Ruben Verheyden

First and foremorst, I would like to thank my advisor Prof. Dr. Samo Korpar for his valuable guidance during this work. In addition, I would like to thank Prof. Dr. Peter Križan for giving me the opportunity to work in the field of experimental particle physics. Without their advice, assistence, and patience this work would not be possible. A thank you is also in order for the colleagues at the department of experimental particle physics. In particular, I would like to thank Rok, Eva, Andrej, Jure for their discussions and technical support. The leadership of the Marie Curie - Particle Detectors (MC-PAD) project also deserves a thank you. Thanks to them, I had excellent training opportunities in the field of particle detectors. Finally, I would like to thank Natalia Belova for her patience and support during this work.

Abstract

The depth of interaction (DOI) effect of gamma rays in scintillator crystals gives rise to the so-called parallax error which negatively affects the quality of positron emission tomography (PET) images. In this work, a novel PET detector module is studied which aims to reduce this parallax error. A novel light sensor (Silicon photomultiplier (SiPM)) is combined with a specially segmented crystal structure which provides a DOI encoding. Reconstruction techniques were studied through Monte Carlo simulations and compared to a more typical type of scintillator crystal array. The performance of the proposed PET module and reconstruction techniques, in terms of tube of response (TOR) resolution, is shown to provide an improvement in resolution outside the central region of a PET scanner. Measurements were performed with a prototype PET module consisting of scintillation crystal with the proposed segmentation coupled to an array of SiPMs. Through these measurements a proof of concept is provided, illustrating the feasibility to reduce the parallax error.

Keywords: DOI, parallax error, PET, SiPM, TOR

PACS: 07.07.Df, 07.85.-m, 29.40.Mc, 29.40.Wk

Povzetek

Pri pozitronski tomografiji (PET) na kakovost slike daleč od osi tomografa pomembno vpliva tako imenovana napaka zaradi paralakse. Do te napake pride, ker v scintilacijskem kristalu, detektorju žarkov gama, običajno ne izmerimo globine interakcije (DOI, depth of interaction). V pričujočem delu sem razvil in preučeval novo vrsto detektorskega modula za PET, pri katerem je bil cilj zmanjšati to napako zaraqdi paralakse. V detektorkem modulu sem uporabil novo vrsto svetlobnega senzorja, silicijevo fotopomnoževalko (SiPM), v kombinaciji s posebej segmentirani kristalno strukturo, ki preko porazdelitve svetlobe zagotavlja kodiranje globine interakcije. Rekonstrukcijske metode za tak detektorski modul sem preučeval s pomočjo računalniške simulacije. Porimerjava novega tipa modula z detektorjem s standardnim segmentiranim je pokazala, da zagotavlja nov tip detektorja izboljšanje resoluciojo izven osrednjega območja PET skenerja. Delovanje prototipa sem uspešno preveril tudi s serijo meritev, ki so potrdile rezultate računalniške simulacije.

Ključne besede: Pozitronska tomografija PET, Silicijeve fotopomnoževalke SiPM, Globina interakcije DOI, Napaka zaradi paralakse.

PACS: 07.07.Df, 07.85.-m, 29.40.Mc, 29.40.Wk

Contents

Chapter 1

Introduction

1.1 Positron Emission Tomography

Positron Emission Tomography (PET) is a non-invasive medical imaging technique for in-depth and in-vivo imaging of live tissue. It provides a three-dimensional image which can be used to track physiological processes in the body. A radioactive tracer is injected into a patient, most commonly fluorodeoxyglucose (FDG), which is a glucose molecule marked with a positron emitting isotope. Emitted positrons will, within a short distance from the emission point, undergo a positron-electron annihilation inside the tissue. This annihilation results in the emission of two 511 keV back-to-back gamma rays. Detection of both gamma rays in coincidence and within an adequate energy window allows to build an image reflecting the FDG distribution in the tissue [1, 2].

These annihilation gamma rays are usually detected indirectly through the use of gamma cameras. Typically gamma cameras for a PET scanner consist of an inorganic crystal in which the gammas are converted into scintillation light. Photodetectors, like photomultiplier tubes (PMTs), are coupled to these scintillation crystals to convert the scintillation light into electric pulses. One or more rings of such gamma cameras are then placed around a patient to obtain an as large as possible field of view (FOV) to construct a three-dimensional image of the radioactive tracer.

While the quality of PET imaging is already very good, there is still a need to further enhance the spatial resolution and signal-to-noise (S/N) ratio of PET scanner technologies. Current technologies for PET scanners generally suffer from the so-called parallax error. This error arises from the lack of detailed information regarding the location of the annihilation gamma interaction inside the scintillator crystals.

1.2 Parallax Error

Most gamma cameras only have the ability to reconstruct the gamma interaction points in the plane of the photodetector. Annihilation gammas which enter the scintillation camera at perpendicular angles to the front surface of the crystal generally do not pose an issue. For such gammas, the camera can achieve it best possible resolution.

Generally, the radioactive tracer is distributed in a large volume within this ring. Combined with the randomized momentum directions of the annihilation gammas, it leads to a substantial amounts of gammas which will enter the scintillation crystals under an angle with respect to the normal of the front surface of the camera, fig. 1.1.

Gamma rays entering a scintillation crystal will pass through it for some distance, determined by the mean attenuation length of the crystal, before depositing its energy. Typical gamma cameras are not capable to measure this distance, known as the depth of interaction (DOI), but are only able to reconstruct the interaction point in the plane of the photodetector.

The schematic in fig. 1.1, provides an exaggerated illustration of the par-

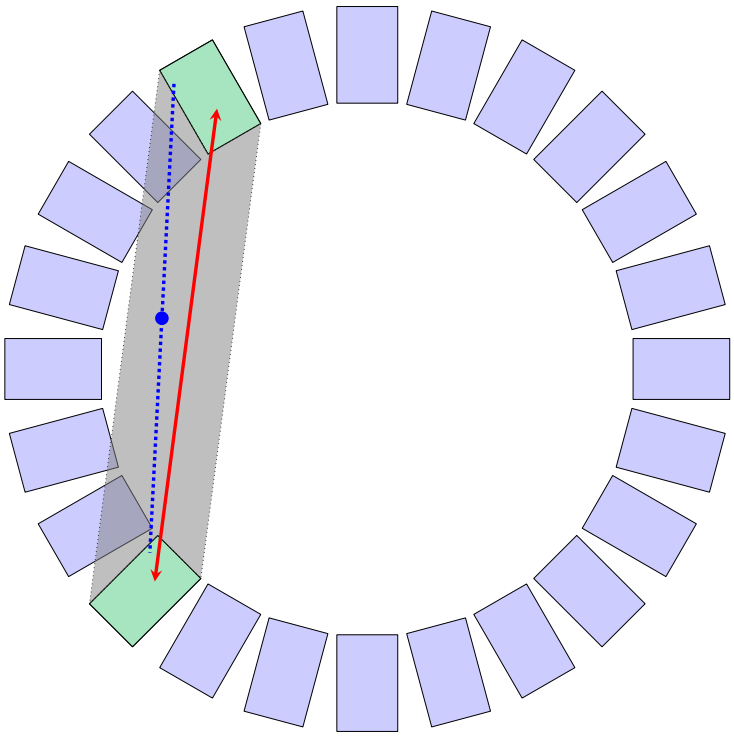

Figure 1.1: Schematic representation of the parallax error introduced due to a lack of depth of interaction (DOI) information from the measured position. The blue dot and lines indicate the real path of the emitted gammas. The assumed line of response (LOR) is indicated by the red line.

allax error. It uses simple gamma cameras consisting of monolithic scintillator crystals which are coupled to single channel photodetector, i.e. no capability to measure position. Detection of the annihilation gammas (blue dashed lines) is thus limited to the knowledge of which gamma cameras were hit. As a result, the line of response (LOR) (full red line) is merely a line connecting both devices. Here, the LOR was estimated by connecting the two centers, in the plane of the front face, at an average DOI. Clearly, the true LOR (blue) and the reconstructed LOR (red) do not line up, leading to a blurring of the image. In effect, the shaded area between both detectors represents the possible area where the annihilation event actually occurred. This area is known as the TOR and for devices without DOI reconstruction it is considerable larger for events occurring at large radial distance from the central axis of the scanner.

1.3 Objectives and Layout of the Thesis

In this thesis, a novel positron emission tomography (PET) detector module is studied with a novel light sensor (Silicon photomultiplier (SiPM)) and a specially segmented crystal structure is proposed which provides a DOI encoding to reduce the parallax error.

Through Monte Carlo simulations, the performance of the crystal structure and specific reconstruction techniques are investigated, in terms of LOR and TOR resolution. The performance of the proposed crystal is compared to a more typical type of scintillator crystal array, which consists of a matrix of finely spaced, but optically isolated scintillation crystals. Finally, a prototype PET module was constructed to provide a proof of concept for the proposed crystal.

The layout of the thesis is as follows:

- The idea of the DOI encoding is presented in chapter 2.
- Chapter 3 discusses technical details of the simulation of the detector response and its basic performance.
- The reconstruction methods and their performance on simulated events are presented in chapters 4 and 5.
- Chapters 6 and 7 present the experimental setup and its calibration.
- Chapter 8 discusses the comparison of simulated and measured data.
- Finally, in chapter 9, the DOI reconstruction on measured data is discussed.

Chapter 2

Depth of Interaction Encoded PET Module

2.1 PET Module

Gamma cameras are required to convert annihilation gammas into detectable signals. The general principle of a gamma camera is to convert the initial gamma ray into a pulse of optical photons, traditionally done with a scintillation crystal. These optical photons are then guided to a photodetector which converts them into an electrical signal.

A PET module is a particular class of gamma cameras which are specially designed for use in PET scanners. Of particular interest for PET modules is that they should have:

- good 2D positional resolution to ensure a good reconstruction of the line of response (LOR),
- good energy resolution for 511 keV gammas to minimize the contribution of in-tissue Compton scattered gammas,
- good timing resolution when time of flight (TOF) information is of importance, e.g. in TOF-PET.

2.1.1 Scintillator

The purpose of the scintillation crystal is to convert the annihilation gammas into optical photons which can then be detected by a photodetector which is optically coupled to the scintillator crystal. To ensure that the PET module achieves a good position resolution, the scintillator crystal is usually cut into small segments. Various configurations for the segmentation of the crystal exist. Traditionally a scintillator crystal was coupled to several PMTs, however the number of PMTs was usually well below the number of

segmentations. To extract the location of the gamma interaction it is necessary to construct the segmentations in such a way that the location can be extracted from the light sharing over the PMTs. Novel light sensor technologies now make it possible to increase the number of photodetectors coupled to the scintillator crystal. This opens up the possibility for new crystal configurations with the aim to reconstruct the depth of interaction (DOI) of the gamma.

Several methods for DOI extraction exist depending on the configuration type of scintillation crystal used. Light spread distributions in monolithic [3, 4] or strong light sharing crystal configurations [5] have been shown to be related to the DOI. Phoswhich scintillator configurations, discrete slabs with different light pulse shapes or continuously varying along the depth [6], allow the DOI to be extracted based on pulse shape analysis. Continuous phoswhich scintillators (CPS) offer a continuous method for DOI measurement, but require complex readout electronics and the development of stable methods to grow crystals with varying doping levels.

Multilayer crystal configurations, on the other hand, offer a simple means of DOI encoding where each layer has a distinct segmentation pattern [7, 8]. The light pattern read out by the photodetector array then allows the identification of the gamma conversion layer. In the present work, a novel version of a similar concept is investigated.

2.1.2 Photodetector

As already discussed, the function of the photodetector is to convert the optical photons produced in the scintillation crystal into a measurable signal. For decades, the PMT was the standard photodetector. However, new applications of PET scanners become possible if novel light sensors are used. There is, for example, a need for new multimodal imaging (MMI) systems to increase the potential of medical imaging systems [9, 10] for the following reasons:

- particular situations require sets of complementary data from different imaging techniques to perform an accurate diagnosis,
- data fusion can provide improved images compared to the individual source images,
- aid the planning of therapeutic procedures, as well as provide a method for monitoring during treatment.

Ideally MMI systems should have the capability to perform the tasks listed above. Due to technical and operational limitations, diagnostic and therapeutic systems are generally separated. The separation of these systems

commonly leads to issues regarding spatial and temporal alignment of the data reducing the quality of the data fusion. Two approaches exist to achieve effective data fusion, the software and hardware approach.

The "software" approach is the more versatile of the two. It allows to fuse data from various sources. However, it requires the alignment of the data through clues from image properties, tissue geometry, and tissue texture. This alignment is susceptible to noise and artifacts as a result from the presence of geometrical distortions in one image, non-rigid motion, anatomical variation between individuals, etc.

With the "hardware" approach, a combination of two or more imaging modalities in a single device is utilized to obtain sets of complementary data. This approach circumvents the issue of spatial and temporal alignment of the image data through the simultaneous acquisition of the data. While it solves the issue of the data alignment it does come with technical limitations on the hardware. In particular, the combination of PET with magnetic resonance imaging (MRI) requires magnetic insensitive photodetectors. Due to the basic operating principle of electron multiplication in a PMT, namely the acceleration of electrons towards dynodes, they are inherently highly sensitive to magnetic fields. Thus alternative photodetectors are required for creation of a PET-MRI hybrid scanner.

2.2 Silicon Photomultiplier

A Silicon photomultiplier (SiPM) is a Geiger-mode avalanche photodiode (G-APD) based device, which is also known as multi pixel photon counter (MPPC). Their use as the photodetector in PET modules offers several advantages over a conventional PMT, including application in a magnetic field, more compact and sturdy design and a potential for reduced production costs. These advantages make the SiPM a strong candidate to replace the conventional PMT.

Currently, SiPMs can only be produced with a smaller sensitive area compared to PMTs, which requires arrays of SiPMs to obtain a comparable active area as a PMT. While initially this can be considered a disadvantage in terms of overall cost, i.e. increased number of photodetectors and electronics per area, it comes with a substantial increase in granularity. This level of increase is difficult to obtain with the other technologies. As for the increase in needed electronics, fortunately the advances in readout technologies, i.e. ASICs and FPGAs [11], have kept pace with the increase in photodetector granularity.

The increased granularity of the photodetector allows to take advantage of the smaller and specially structured segmentations of the scintillator crystal. For instance, with a SiPM array it is feasible to have a one-to-one mapping

of small scintillator segments to single SiPM channels. With classical PMTs a one-to-one mapping is highly impractical. Either the crystal segmentations need to be large, resulting in a diminished positional sensitivity, or small PMTs would have to be used which would result in a considerable loss in sensitive area fraction caused by the PMT housing.

2.2.1 Characteristics

A SiPM is a novel photodetector created from an array of G-APDs. They are avalanche photodiodes (APDs) which are operated in the Geiger mode [12]. Those G-APDs are often referred to as cells. Essentially a G-APD consists of a p-n junction diode which can be operated at a high reverse bias to provide a high internal amplification, also known as APD gain. However, the Geiger mode operation of the G-APD cells, results in a total discharge of the cell. This limits its operation to the detection of a single photon until the cell has recharged sufficiently. Recharge time τ for a G-APD depends on the cells properties, with typical values in the range 10 ns–300 ns. For this reason a SiPM is always constructed as an array of G-APDs (cells), usually arranged in a matrix. The resulting signal which is proportional to the number of fired cells, thus depends on the number of detected photons.

A schematic of a SiPM is shown in fig. 2.1 illustrating how the array of avalanche photodiodes are connected internally. Each photodiode is placed in a series with a quenching resistor R_q, while all photodiodes and their quenching resistors are connected together in parallel. A common reverse bias is applied to the photodiodes, set slightly above the photodiode breakdown.

The role of the quenching resistor is to halt the avalanche. Once an

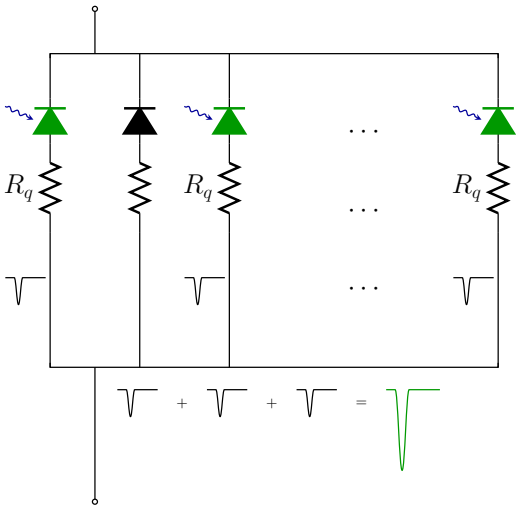

Figure 2.1: Sketch of the principle of operation of a SiPM for an ideal light pulse.

avalanche is triggered by a particle, i.e. a photon, the avalanche current causes a potential drop across the quenching resistor. A sufficiently large value for the quenching resistor will cause the potential across the photodiode to drop below the required bias to produce avalanches in the photodiode. Due to this drop in potential across the photodiode, the internal electric field in the photodiode will not accelerate the carriers enough for breakdown to occur.

For each G-APD detecting a photon the signal will propagate towards the readout. Due to the parallel connection between all G-APDs, all G-APD signal amplitudes A_i of simultaneously fired G-APDs will constructively add together to produce a summed signal A. This signal A is equal to the average amplification factor M times the number of photodiodes which fired N_{fired}. For an ideal scintillation light pulse, i.e. when all scintillation photons are detected at the same time, the total SiPM output signal becomes

$$A = \sum A_i = q \cdot M \cdot N_{fired} \ , \tag{2.1}$$

where q is the elementary charge and M is the average amplification factor of a single G-APD in the SiPM. This G-APD amplification factor M depends on the G-APD capacitance C, the applied reverse bias V_{R}, and V_{BR}, the G-APD breakdown voltage, and is given by

$$M = \frac{C \cdot (V_{\mathrm{R}} - V_{\mathrm{BR}})}{q} \ . \tag{2.2}$$

Typical G-APD gains are in the range of 10^5 to 10^7. Under ideal circumstances the full gain of a SiPM is given by eq. (2.1). However, a realistic SiPM signal behaves non-linearly and is described by

$$A \approx N_{fired} = N_{total} \cdot \left(1 - e^{-\frac{\mathrm{PDE} \cdot N_{phot}}{N_{total}}}\right) \ . \tag{2.3}$$

where N_{total} is the total number of SiPM cells, and N_{phot} the number of photons in the light pulse. The photon detection efficiency (PDE) of the SiPM is a combination of the quantum efficiency (QE) of the active area of the device, a geometric factor ϵ accounting for the active area v.s. total device area, and the probability for a photon to trigger a breakdown P_{trig},

$$PDE = QE \cdot \epsilon \cdot P_{trig} \ . \tag{2.4}$$

These non-linear effects can mostly be attributed to:

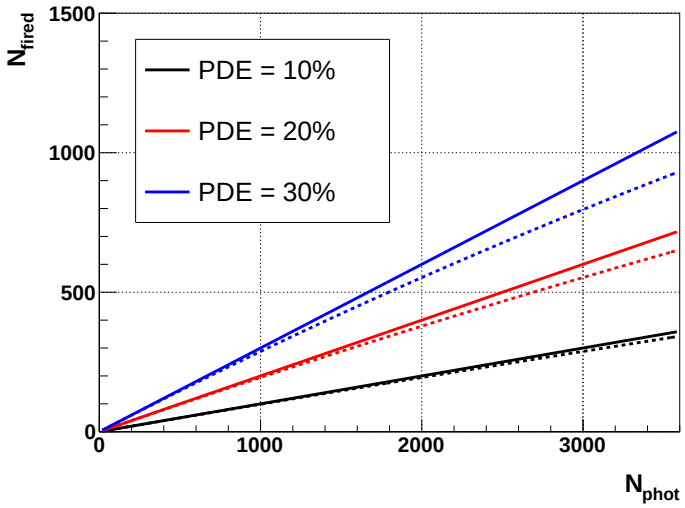

Figure 2.2: Illustration of the non-linearity of the SiPM response for various PDE. The full lines indicate the response if the device would behave in a linear fashion. Dashed lines represent the non-linear behaviour of the SiPM.

- The finite number of cells, which is the dominant factor when the number of photons is no longer small compared to the number of cells.
- The non-zero recovery time of cells leads to a loss of photons due to multiple photon impacting the same cell before the cell has fully recovered.
- Drop in ΔV due to significant signal current on the external series resistance.

In fig. 2.2 the non-linear behaviour of a SiPM device is illustrated for a device with 3600 cells. As can be seen from the figure, an increased PDE will result in an increase of the non-linear behaviour. Regardless of this effect, a larger PDE will result in a higher detected number of photons which will eventually result in a better energy resolution.

2.2.2 Dimensions

For this work a S11830-3344MT(X) from Hamamatsu Photonics K.K. was chosen as photodector. It consists of an array of 16 SiPMs in a monolithic package, see fig. 2.3. The SiPMs have an active area of $3 \times 3\,\mathrm{mm}^2$ and they are arranged in a 4×4 matrix with the SiPM pitch of 3.2 mm. Each SiPM consists of a 60×60 array of single cells, 3600 cells in total, with a cell pitch of 50 µm. The entire SiPM array is combined into a monolithic package with a 0.3 mm layer of protective glass epoxy and mounted onto a surface-mountable PCB with a thickness of 1 mm.

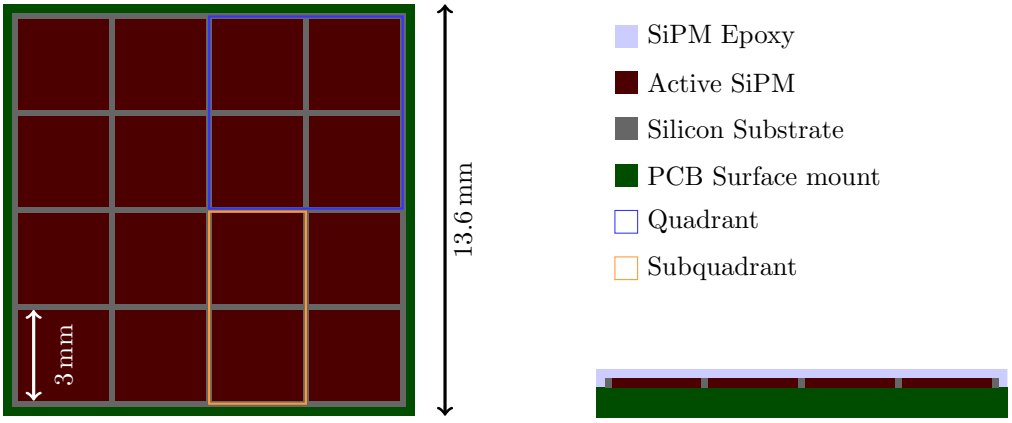

Figure 2.3: Sketches of the dimensions of the SiPM array. (a) Top view of the array, with basic dimensions marked. A single quadrant is outlined by a blue square, while in orange a subquadrant is outlined. The subquadrant outline denotes the orientation of crystal layer 3. (a) Side view of the SiPM array. The terms quadrant and subquadrant indicated in the figure will be defined at a later stage.

2.3 DOI Encoded Scintillator Crystal

The principle behind the DOI encoding is the variation in light sharing between the channels of the SiPM array which depends on the depth at which the gamma interaction occurs. The DOI encoded scintillator crystal, as developed within this work, consists of a monolithic block made from a Cerium-doped Lutetium Yttrium Orthosilicate (LYSO) scintillation crystal. Several cuts with varying depths were made in this block resulting in 4 layers with varying degrees of segmentation. These cuts start at the sensor side of the scintillation crystal, and are made in such a way that the segmentation becomes finer when getting closer to the sensor. A schematic of each layer is shown in fig. 2.4 with a description of each layer as follows:

- L1: The top layer has no segmentation to allow light sharing over all the SiPM channels. It is also the layer closest to the source (i.e. furthest away from the SiPM array) with the entry face of the crystal being the side of this layer closest to the source. The thickness of the layer is 6 mm.

- L2: The second layer has a 2×2 segmentation by making two perpendicular cuts starting at layer 4, i.e. from the sensor side of the crystal, up to a depth of 14 mm. The thickness of this layer is 5 mm and it consists of four quadrants (Qs). In fig. 2.4a a single Q is marked in blue.

- L3: The third layer has a 2×4 segmentation by making two additional, but parallel cuts. Location of the cuts is in the middle of the segmentations of layer 2. Again the cuts start at layer 4 and are made 9 mm deep. The thickness of this layer is 5 mm, and the layer consists of eight subquadrants (SQs). Similarly as for layer 2, a single SQ is marked in orange in fig. 2.4a.

- L4: The fourth and final layer has a 4×4 segmentation by making two additional, but parallel cuts that are perpendicular to the additional cuts for layer 3. Location of these cuts are made such that it results in 16 equally sized segments matching the dimension of the underlying SiPM array. Due to these segments lining up with the SiPM array they will be referred to as channels (CHs). The final cuts are 4 mm deep resulting in a thickness of 4 mm. The bottom side of this layer is called the exit face and is coupled to the SiPM array. Once again, for clarity a single CH is marked in green in fig. 2.4a.

Finally a 3D model is presented in fig. 2.4d to illustrate a fully assembled PET module with the proposed DOI encoding segmented scintillation crystal. The entry face of the scintillation crystal is situated on the top side of the figure while the exit face of the scintillation crystal can be seen on the bottom side. In addition, the SiPM array is shown without support and protective layers. A cutout is made in the SiPM array to uncover the exit face of the segmented crystal structure.

The main idea behind the DOI encoding is to observe how ratios of various combinations of signals of the SiPM channels change as a function of depth. To illustrate the principle behind the DOI encoding, a simplified model for the light sharing is presented. In this model, at each point of photon emission inside the crystal, the solid angles for each channel of the light sensor are estimated. These estimates are obtained by modelling the segmented crystal volume as two 2D planar modules each having four channels. Those two planar modules correspond to the two different directions as shown in figs. 2.4b and 2.4c. Approximated solid angles for all the 16 channels are then obtained by multiplying the channels from these 2D planar modules. A detailed description for the calculation of these 2D solid angles can be found in appendix A.

With these approximated solid angles, the solid angles for the channels in a Q and SQ are added together. From these values, the following ratios are then calculated for each point of emission,

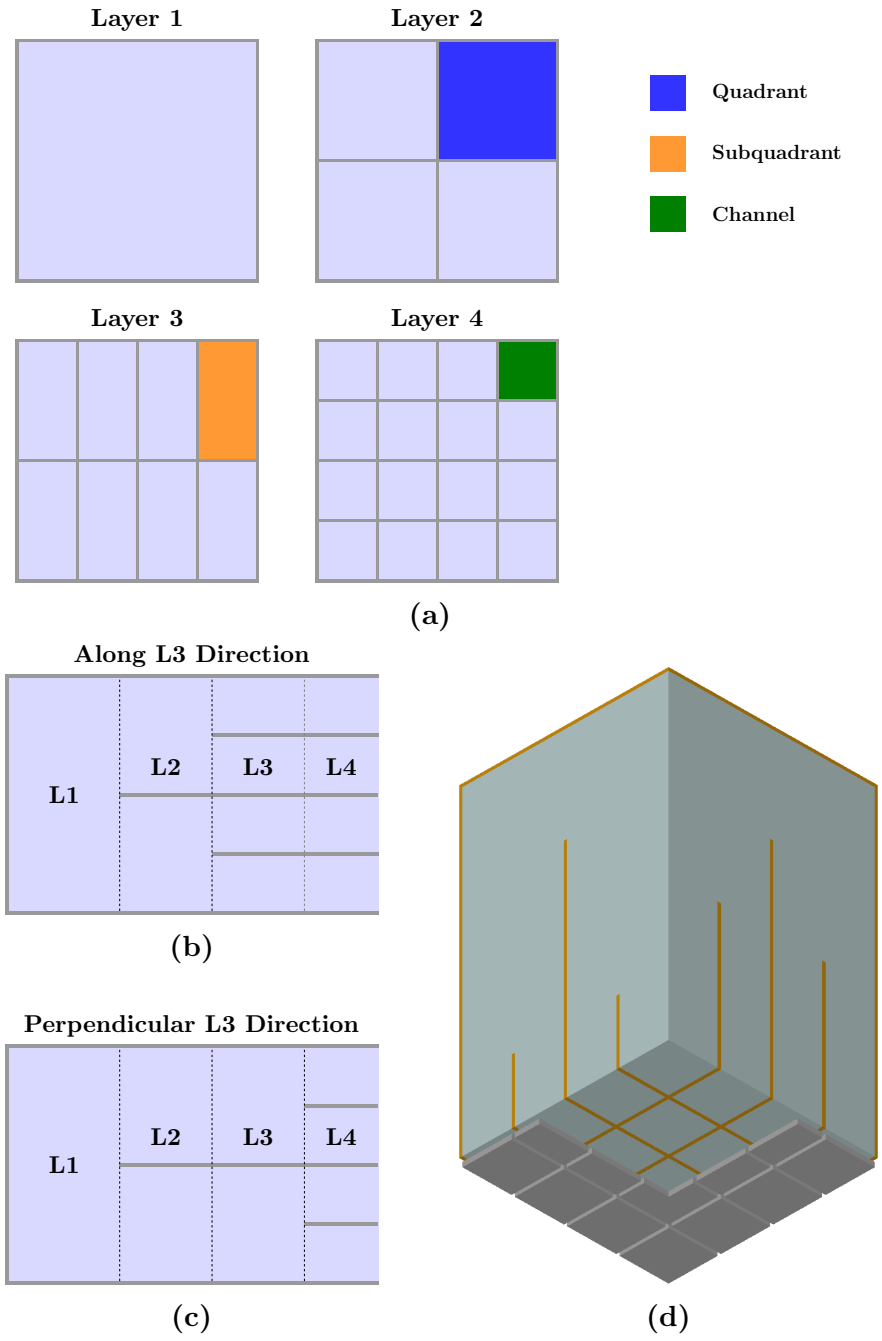

Figure 2.4: Segmentation for the four different layers: (a) top view of the four different layers, (b) side view of the crystal along the maximal segmentation of layer 3, (c) side view which is perpendicular to the maximal segmentation of layer 3. (d) 3D model of the proposed segmented crystal for the PET module.

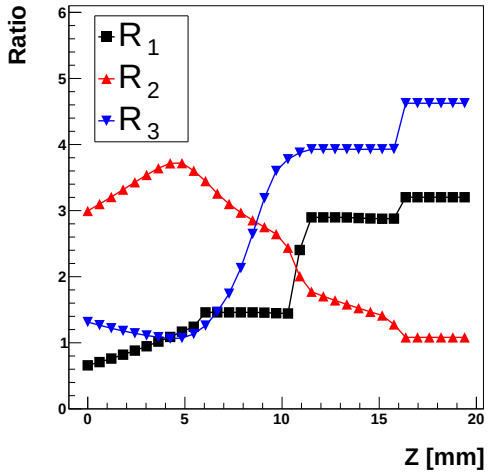

Figure 2.5: Approximated ratios as a function of the depth of the points of emission.

$$R_1 = \frac{Q_{max}}{\sum_{q \neq max} Q_q} \ , \tag{2.5}$$

$$R_2 = \frac{Q_{max}}{CH_{max}} \ , \tag{2.6}$$

$$R_3 = \frac{SQ_{max}}{SQ_{neighbour}} \ . \tag{2.7}$$

where Q_{max} (SQ_{max}) is the Q (SQ resp.) with the maximum sum, $SQ_{neighbour}$ being the neighbouring SQ which is in the same Q as SQ_{max}, and CH_{max} the channel with the maximum fraction of detected photons. These values of these ratios are then plotted as a function of the depth of the point of emission. Figure 2.5 shows the resulting ratios and they show a clear variation along the depth of the segmented crystal.

This is clearly a simplified picture which will be investigated in more detail by Monte Carlo simulations and by a prototype set-up. Also, reconstruction methods are developed to take advantage of these ratios to reconstruct the DOI of the annihilation gamma rays.

2.4 Terminology

It is necessary to define some terminology which is used throughout this work. Some of these terms were already mentioned before in this section, but are properly introduced in what follows. A separation is made between terms

directly related to the PET module layout and terms which are related to the reconstruction techniques.

2.4.1 Module Layout

Due to the specific layout of the entire module, i.e. crystal with SiPM, there are several naturally formed elements. These elements were already marked in figs. 2.3 and 2.4. Below follow the definitions of each element:

quadrant (Q) The grouping together of four neighbouring channels as illustrated in figs. 2.3 and 2.4 is defined as a quadrant. Four such groups can be made for the entire module. A certain level of symmetry exists between each quadrant.

subquadrant (SQ) Neighbouring channels are grouped together in a pairwise manner, figs. 2.3 and 2.4, to form the subquadrants. Such grouping together provides 8 subquadrants in total. These groups are naturally formed by the crystal segmentations of the third layer (L3). Subquadrants are the elements which effectively introduce a non-symmetrical orientation to the module. For this reason two new terms are introduced to refer to the orientation of the module.

- **Along** In this orientation the point of view is such that it looks along the segmentations of the third layer (L3). Figure 2.4b provides an illustration as to how a source placed on this side of the module would see the crystal structure.
- **Perpendicular** Here, the point of view is perpendicular to the segmentations of the third layer (L3), illustrated by fig. 2.4c.

channel (CH) This term refers to an active SiPM channel, fig. 2.3, as well as to the smallest segmentation of the crystal, fig. 2.4. The identical dimensions in the detector plane of both the SiPM and the crystal element allows to use this term for both without confusion. In total there are 16 channels for the entire module.

2.4.2 Reconstruction Layouts

During the introduction and discussion of the reconstruction methods, several terms are introduced which play a critical role.

Cube One of the reconstruction methods, which will be introduced later, depends on a virtual segmentation of the scintillator crystal into equally sized parts. These segments are called cubes and they are formed by dividing the crystal into four equally thick layers along the length of

the crystal. Each of these layers is then divided into 16 equal boxes. In total, this produces 64 cubes, i.e. 16 cubes per layer and four layers.

Layer This term can refer both to the real layer segmentations of the crystal, fig. 2.4a, or to the layer divisions introduced for the cubes. Both terms are nearly identical, but in reality there is a small difference in dimensions. The cube layers all have a thickness of 5 mm as opposed to the real layer segmentations which have varying thicknesses. To avoid confusion, the use of cube layer will be clearly marked in the remainder of this work. The cube layer numbering follows the same system as the real layer segmentations, i.e. layer 1 (layer 4) is furthest from (closest to resp.) the detector array.

Box Each layer of cube divisions consists of a 4×4 matrix of boxes. These boxes nearly match the SiPM channel dimensions, however the presence of the reflectors between the segmentations results in a slight mismatch in dimension. Nonetheless, the boxes in each layer follow the identical numbering system as the SiPM channel numbering.

Pillar Grouping together of several cubes, results in the formation of a pillar. Each pillar effectively groups four cubes together, reducing the original 64 cubes to 16 pillars. Later in this work, two types of experimental measurements will be introduced to study the performance of the module. For each type of measurement, the pillars combine the cubes together which are situated in line from the point of view of the source. This results in the definition of the following two types of pillars.

- **XY** Cubes of all layers with identical box numbers are combined together in one pillar. Effectively, there are 16 pillars in a 4×4 grid which extend from the front side of the crystal to the exit surface (detector side).
- **DOI** Here, cubes are combined together which are in the same layer and in line with each other from the point of view of the source.

Slice Similarly as for the cube layers, slices are virtual divisions of the crystal along the length of the crystal. However, the slice divisions are made with a finer granularity compared to the cube layers. Slices are introduced for the DOI reconstruction methods, where the dimensions of the slices will be defined.

Mapping

To aid the understanding of the presentation style of future results, the two most prominent used mappings are defined. Whenever several figures are pre-

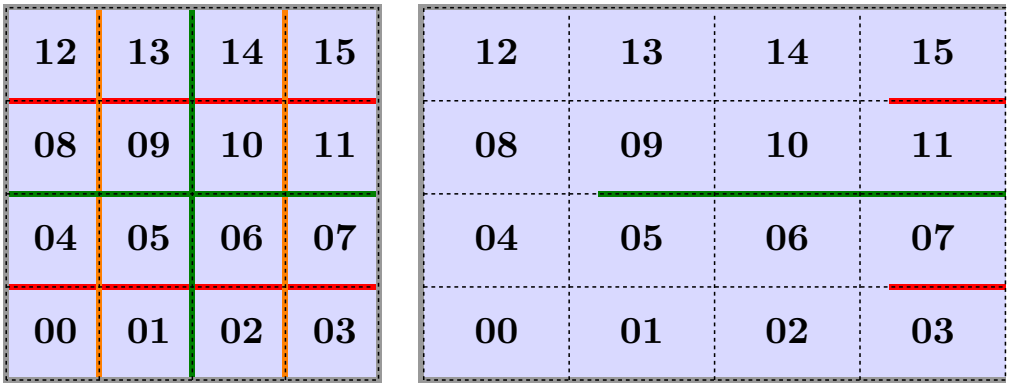

Figure 2.6: Schematic of the box and pillar mappings used throughout this work. It represents the mapping of the box IDs used for the cube divisions within the layers. The pillar mapping for the XY scan directions follow the exact same mapping.

sented in a grid pattern, the locations of each figure in that grid corresponds to the element (box, cubes, pillar) as shown in these mappings.

Figure 2.6a shows the mapping of the box indices of the cubes inside each layer. This mapping is identical to the channel mapping in the SiPM array and is primarily used to describe the mapping for the XY style measurements.

The mapping for the DOI type measurements is presented in fig. 2.6b and correspond to how the pillars are mapped when the point of view is from the side of the module.

Chapter 3

Simulation: Details and Basic Performance

Simulations are an excellent tool to dissect and understand the various influences of all involved parameters of the detector for the reconstruction of the DOI. The Geant4 toolkit [13, 14] provides a framework to simulate the passage of particles through matter. It is a very mature framework which is widely used in the field of high energy physics, astrophysics, and medical physics.

Various PET modules, illustrated in fig. 3.1 and 3.2, were implemented in the Geant4 toolkit, each consisting of a scintillator, optical coupling grease and a photodetector (a single SiPM or a SiPM array). A single SiPM type module was used to cross-check the basic physics performance, while a single SiPM array type module was used to study the DOI capabilities of the proposed LYSO scintillator segmentation.

This chapter starts with a description of the construction of the detector, the physics processes used and the parameters for the material characteristics. Afterwards, the basic physics of the simulation are checked to ensure that the results are realistic.

3.1 Simulation Parameters

The simulations were performed using the Geant4 toolkit. Due to the dependence of Geant4 on additional software packages a complete list of the relevant used packages with their version numbers is provided:

Geant4: Particle Physics Simulation toolkit 4.10.p02 [15]

CLHEP: Class Library for High Energy Physics 2.2.0.3 [16]

G4EMLOW: Low Energy Electromagnetic Processes 6.35 [17, 18]

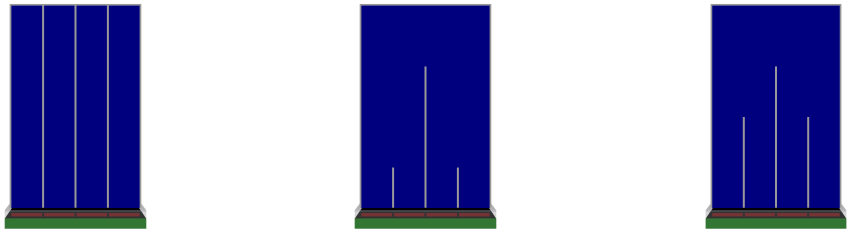

3.1 **3.2a** **3.2b**

Figure 3.1 & 3.2: Various PET modules implemented in geant for the simulations: (3.1) A scintillator array type module used for comparison with the DOI encoded scintillation crystal. (3.2a) and (3.2b) provide two different sideviews of the DOI encoded scintillator type module.

G4PII: Impact Ionisation 1.3 [18]

Real Surface: Measured Optical Surface Reflectance LUT 1.0 [18, 19]

3.1.1 Physics List

Geant4 requires the selections of particles and physics processes to include in the simulation. Ideally, only physics processes and particles relevant to the simulation should be included. For these simulations, the Livermore physics models were selected for the low energy electromagnetic processes. These include the following models for the relevant particles:

Gamma Particles: Photoelectric Effect, Compton Scattering, Gamma Conversion, and Rayleigh Scattering

Electrons: Multiple Scattering, Coulomb Scattering, Ionisation, and Bremsstralhung

Optical Photons: Absorption and Boundary processes

Atomic de-excitations are by default enabled in the Livermore physics models. In addition, only the scintillation process was used for the production of optical photons. Cherenkov photon yield is considerably lower than the scintillation photon production.

The so-called *unified model* from Geant4 and the *lookup tables (LUTs)* provided by the Real Surface software package were used to simulate the optical interfaces. Between two optically transparent dielectric materials the *unified model* only requires the user to set refractive indices for both materials.

On the other hand, the LUTs were used to simulate the reflective optical interfaces. These LUTs rely on data obtained through measurements of several types of commonly used reflective materials, [19–21]. These LUTs allow

to simulate a variety of reflective surfaces without explicitly knowing all the details of the reflective material.

3.1.2 Detector Modelling

The dimensions and parameters for the simulated PET module were closely matched to the dimensions and properties of the real detector components described in sections 2.2.2 and 2.3. The simulated PET module consisted of three main components: a scintillator, a coupling interface and a SiPM photodetector array.

Scintillator:

LYSO was chosen as scintillator material and the dimensions of the segments and the reflector planes in between were matched to the dimensions of the SiPM array. Two different types of scintillator configurations are investigated:

Matrix: A matrix consisting of 16 independent LYSO crystals arranged in a 4×4 matrix separated by reflective material. The dimensions of each individual crystal in the matrix were set to $3 \times 3 \times 20\,\mathrm{mm}^3$ matching the active area of a single SiPM channel of the photodetector.

DOI: The proposed DOI encoding segmentation described in chapter 2. The crystal array is constructed in such a manner that the full crystal structure behaves as a single block, i.e. no interfaces between the layer implementations. In each layer, reflective material is placed in between the segmentations of that layer.

Both scintillator configurations had $MgSO_4$ powder placed around the crystal arrays and in between the segmented sections to act as a reflective material. A thin layer of Aluminium is wrapped around the entire scintillator block. Only the exit face of the scintillators was not covered with the reflective material and the thin Aluminium layer.

Coupling Interface:

A coupling grease with a thickness of 0.2 mm was placed in between the exit face of the scintillator and the SiPM array. It is needed to prevent a thin layer of air being trapped in between the scintillator and the photodetector. Such a thin layer of air would greatly reduce the light collection efficiency caused by total internal reflection.

Photodetector:

The implemented photodetector was modelled after the SiPM array

Element	K shell [keV]	Fraction Mass %
Lu	63.314	70.7
Ce	40.443	1.0
Y	17.038	4.0
Si	1.839	6.3
O	0.533	18.0

Table 3.1: LYSO elemental composition with their fractional mass used in the simulations and their K shell binding energies.

described in section 2.2.2. Each individual SiPM was enabled to act as an active detector with photon detection being limited to counting the photons hitting the SiPM.

3.1.3 Material Properties

To ensure realistic simulations, material properties need to be provided to the simulation toolkit for each detector component. Defining the material density and chemical composition of each material allows Geant4 to derive the relevant material properties based on the external data packages specified above. However, the user needs to define the optical properties of the materials and define the properties of the optical boundaries between the components.

LYSO Scintillator

The LYSO chemical composition was based on data provided by Saint-Gobain Ceramics & Plastics, Inc. for their PreLude™ 420 LYSO scintillating crystal [22]. According to their data sheet it has the following composition $Lu_{2(1-x)}Y_{2*x}SiO_5 : Ce$ with a 10 % Yttrium content ($Lu_{1.8}Y_{0.2}SiO_5 : Ce$). Due to a lack of reliable data regarding the Ce doping concentration it was set to 1 % based on the value reported in [23]. Mass density of the material was set to 7.1 g/cm^3. In table 3.1 a full list of elements with their fractional mass and K shell binding energies [24, 25] is provided.

LYSO being a Lutetium-based scintillator means that it contains the naturally occurring radioactive isotope ^{176}Lu with a natural abundance of 2.59 %. It is a β-emitter with a half-life $t_{1/2}$ =3.56 $\times$ 10^{10} y and 99.66 % of the time it decays to the 597 keV excited state of ^{176}Hf, [26]. From this state it decays through a cascade of three prompt gamma rays with the following energies (in order of the cascade): 307 keV, 202 keV and 88 keV. Total count

rates for the self radioactivity was measured by Saint-Gobain Ceramics & Plastics, Inc. to be rather low ($R_{self} = 39\,\mathrm{cps/g}$). For the volume of the simulated array type LYSO crystal this would lead to an effective count rate R_{eff}:

$$\begin{aligned} R_{eff} &= V_{scint} \cdot \rho_{\text{LYSO}} \cdot R_{self} \quad \& \quad V_{scint} = N_{ch} \cdot V_{ch} \\ &= 16 \cdot 3 \cdot 3 \cdot 20\,\mathrm{mm}^3 \cdot 7.1\,\frac{\mathrm{g}}{\mathrm{cm}^3} \cdot 39\,\frac{\mathrm{cps}}{\mathrm{g}} \\ &= 797\,472 \cdot 10^{-3}\ \mathrm{cps} \\ R_{eff} &\approx 800\ \mathrm{cps}. \end{aligned} \tag{3.1}$$

A detector placed at a distance d from a point source will only receive a fraction of the emitted annihilation gammas related to the solid angle subtended by the detector at the source position. The fraction of the solid angle for the detector can be approximated with

$$\begin{aligned} \frac{\Omega}{4\pi} &\approx \frac{A_{det}}{4\pi d^2} = \frac{(12.6\,\mathrm{mm})^2}{4\pi(400\,\mathrm{mm})^2} \\ &\approx 10^{-4}. \end{aligned} \tag{3.2}$$

Typical radiation dosages administered to a patient is on the order of several hundreds of MBq to 1 GBq, [27, 28], resulting in an approximate count rate at a single module of 10–100 kcps. Thus the effective count rate of ≈800 cps for self radioactivity of the scintillator, compared to the flux of annihilation gamma passing through the module is negligible. The maximum deposited energy of any of the decays is well below the photopeak (PPK) of the 511 keV annihilation gammas. In addition, according to Goertzen [29], the intrinsic count rates from LYSO can be drastically reduced by a factor of 100 by limiting the energy window for event acceptance to the PPK. Thus the self radioactivity of LYSO was left out of the simulations.

Scintillation processes in Geant4 [30] require to set the absolute light yield Y, the intrinsic energy resolution at full width at half maximum (FWHM), the time constant, the emission spectrum, the optical absorption length and the refractive index for the material. LYSO has a light yield of $Y = 32\,\mathrm{photons/keV}$ leading to a mean number of photons, $n_{phn} = E_\gamma \cdot Y = 16\,352$, for an energy deposit of 511 keV.

In Geant4 the actual number of photons emitted in an event fluctuates around the mean number of photons n_{phn} with a variance given by $R_{\text{E}}^2 \cdot n_{phn}$, [30, p. 167]. The resolution scale parameter R_{E} allows the user to either make the fluctuations narrower or broader. By default, Geant4 sets the resolution scale parameter $R_{\text{E}} = 1$. The resolution scale parameter R_{E} is closely related to the more generally known Fano factor [31] given by $F = \sigma_{\text{W}}^2/\mu_{\text{W}}$ with σ_{W}^2 the

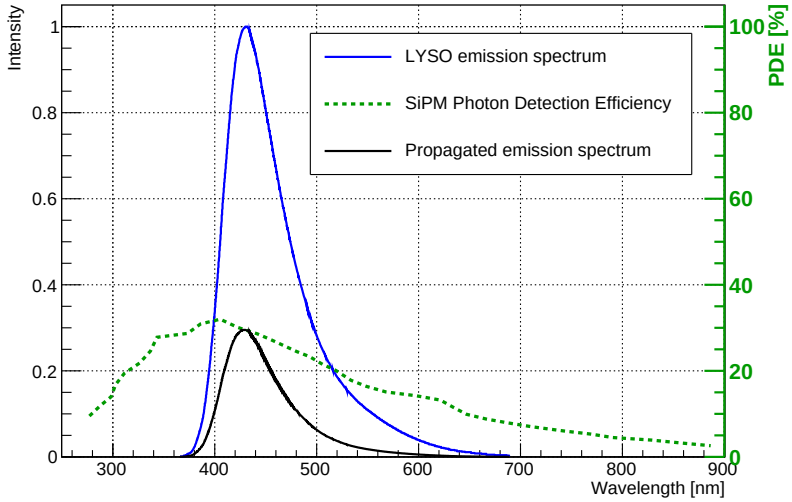

Figure 3.3: Emission spectrum of LYSO [34] provided as input to the simulation. For comparison, the PDE of the SiPM as a function of wavelength was added [35].

variance and μ_{W} the mean of a random process in a given time window W. For a Poisson process the Fano factor would be equal to one. However, realistic doped scintillation crystals like LYSO generally suffer from an inhomogeneous response [32] which causes the distribution of emitted photons to broaden, resulting in a minor degradation of the energy resolution as opposed to an ideal scintillator. As a consequence, doped scintillation crystals like LYSO generally have a Fano factor significantly larger than one, [33].

To set the resolution scale parameter R_{E}, we used data from Saint-Gobain Ceramics & Plastics, Inc. [22]. Thus an intrinsic energy resolution of $\Delta E/E = 8\,\%$ FWHM was used for the LYSO crystal. It was assumed that the measured energy resolution by Saint-Gobain has negligible contributions from the photodetector and crystal geometry they used. As it turned out later, the LYSO crystal produced by Sinoceramics (USA), LLC. has a worse intrinsic energy resolution compared to the crystals from Saint-Gobain.

LYSO has a single and rather short time constant of 41 ns, a refractive index of 1.81 and an attenuation length of 1.2 cm for 511 keV gamma rays. Figure 3.3 shows the emission spectrum for LYSO [34] (peak emission at 420 nm) and compares it to the SiPM PDE [35] as a function of wavelength.

For future comparison an additional photon spectrum was added to fig. 3.3. To drastically cut down on the simulation time the PDE is applied in the simulation at the photon generation step. Using the data for the PDE in function of photon wavelength (see fig. 3.3), a randomly selected fraction of the generated photons are propagated through the scintillation

crystal. The remainder of the generated photons are discarded.

$MgSO_4$ Reflector

The entire scintillator structure was surrounded by a 0.2 mm thick layer of $MgSO_4$ wrapped with an aluminum layer. Only the exit surface was kept free of reflective material as it was coupled to the photodetector. Reflector thickness in between the segments of the structure was set to 0.2 mm matching the spacing between the channels of the SiPM array.

The optical interface between the LYSO crystal and the $MgSO_4$ powder was simulated by setting the properties of the interface to the *polishedtioair* LUT from the Real Surface data software package. The *polishedtioair* simulates a layer of TiO_2 on a polished surface, the LYSO crystal in this case.

The TiO_2 paint is a diffuse reflector which has reflective properties that closely match the properties of a $MgSO_4$ reflector [21]. The difference being the sharp cut-off at wavelengths below 400 nm for the TiO_2 paint. However, because LYSO only emits a small fraction of photons with a wavelength below 400 nm (see fig. 3.3), this was considered to be a negligible difference.

Optical Coupling grease

A layer of 0.2 mm of optical coupling grease was placed in between the exit surface of the scintillator and the photodetector. Its properties were matched to those of the REXON RX-688 optical coupling grease [36] while the boundaries between the optical grease, the scintillator exit surface and photodetector entry surface were always taken to be polished.

Based on the data for REXON RX-688, the refractive index of the coupling gel was set to $n = 1.461$ (mean of 1.457–1.466). The transmission probability of the optical coupling gel was set to 1 (optical transmission of 79 % for 1 cm $\rightarrow >$ 99.9 % for 0.2 mm). In the simulations both values were set to be constant over the entire range of wavelengths.

Photodetector

The epoxy layer is the entry surface of the photodetector and its surface finish was set to polished. The exit surface of the epoxy layer was set to polished as it leads to the active area of the SiPM array and thus acts as an additional optical boundary. Neither the value of the refractive index nor the transmission data for the epoxy in the wavelength spectrum of interest was available, but Hamamatsu Photonics K.K. (HPK) claims (through private communication) that it has a refractive index of 1.55 at a wavelength of 589 nm. Transmission was set to 100 % considering that the PDE for the SiPM already includes the transmission losses through the epoxy layer. Pho-

tons arriving at the active area of the photodetector were counted into their respective channel.

3.2 Basic Performance

This section discusses the performance of the basic physics of the processes involved in the simulation to ensure that realistic results are obtained. For these simulations a DOI encoding type crystal coupled to a SiPM array was used. The module was exposed to 511 keV gamma rays with their impact positions uniformly distributed over the scintillator entry surface and with their momentum perpendicular to the entry surface.

In sections 3.2.1 to 3.2.3 the results for the basic physics are verified to ensure that the input parameters are correctly handled by the simulations. Section 3.2.4 then studies the effects of light sharing in the DOI encoded crystal on the energy resolution $\Delta E/E$.

3.2.1 Gamma Interaction

To obtain scintillation photons, first the 511 keV gamma ray needs to interact with the LYSO crystal. In this case, for a 511 keV gamma ray only the photoelectric effect and Compton scattering are of importance. To study the DOI reconstruction through simulations, it is imperative that the distribution for the interaction depth returns an attenuation length of 12 mm. In fig. 3.4, DOI distributions for the first gamma interaction of all events are presented. In addition, separate DOI distributions for the photoelectric effect and Compton scattering are shown as a cross-check for both processes, i.e. Compton scattering and the photoelectric effect.

The attenuation length for 511 keV gammas of the LYSO crystal in the simulations are extracted from fig. 3.4 by fitting the distributions with the following formula:

$$P(x) = A \cdot \exp\left(-\frac{x}{\lambda}\right), \tag{3.3}$$

where the constant A was introduced to compensate for the non-normalised distributions. The result for the attenuation length (λ) is in reasonable agreement with the attenuation length (λ) of 12 mm provided by Saint-Gobain Ceramics & Plastics, Inc. [22]. It is not expected that this minor difference of 0.47 mm has any noticeable influence on the performance of the DOI reconstruction.

3.2.2 Electron Production

Whenever a gamma ray interacts with the LYSO crystal, it transfers part or all of its energy to an electron. For each event, the initial kinetic and

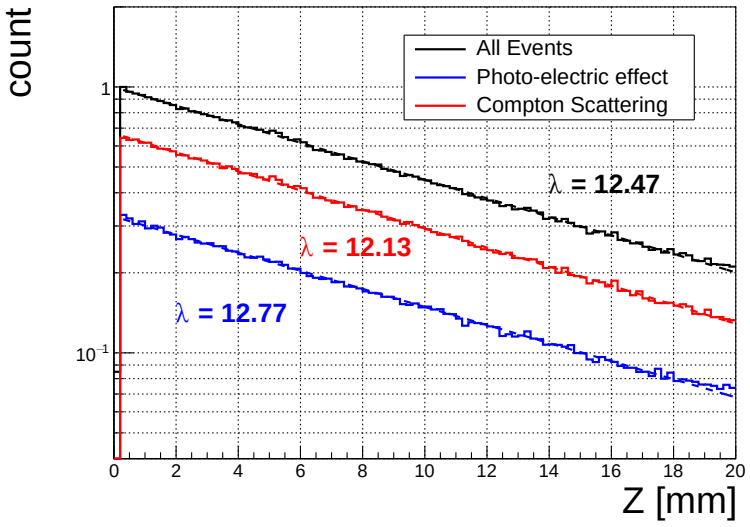

Figure 3.4: Depth of interaction distributions for 511 keV gamma rays in a 20 mm long LYSO crystal of the DOI encoding type. Also shown are the separate contribution for the photoelectric effect and Compton scattering.

deposited energy of all gamma rays and electrons that were produced during the simulation, e.g. mother and daughter particles, was recorded. Energy distributions are constructed for the initial kinetic energy of each electron produced by the first interaction of the primary generated gamma ray. The resulting distributions are presented in fig. 3.5. In addition a separation was made between electrons produced by the photoelectric effect or Compton scattering.

The spectrum for the photoelectric effect shows several clearly separated peaks near the rightmost end of the spectrum. These correspond to the maximum energy transfer of a 511 keV gamma ray to an electron, resulting in an electron kinetic energy of 511 keV minus the binding energy of a K shell electron. Binding energies for the K shell electrons for the various LYSO components can be found in table 3.1. The most prominent peak corresponds to an electron originating from Lu with a K shell binding energy of 63.314 keV.

A clear distinctive Compton edge can be observed around 340 keV which corresponds to a 511 keV gamma ray that has backscattered in the LYSO crystal. The lack of a sharp Compton edge is the result of doppler broadening of the electron momentum due to the inclusion of atomic shell effects in the simulations [37, 38].

In fig. 3.6, distributions for the energy losses and depositions of the initial 511 keV gamma rays are presented. The black histogram presents the total energy loss of the initial 511 keV gamma.

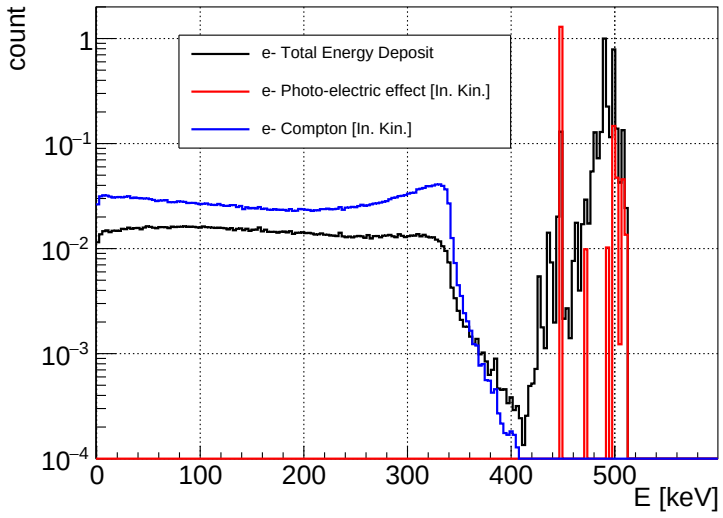

Figure 3.5: Initial kinetic energy distributions of electrons produced by the interaction of a 511 keV gamma ray in a 20 mm LYSO crystal. The separate contributions for the photoelectric effect versus Compton scattering are also shown.

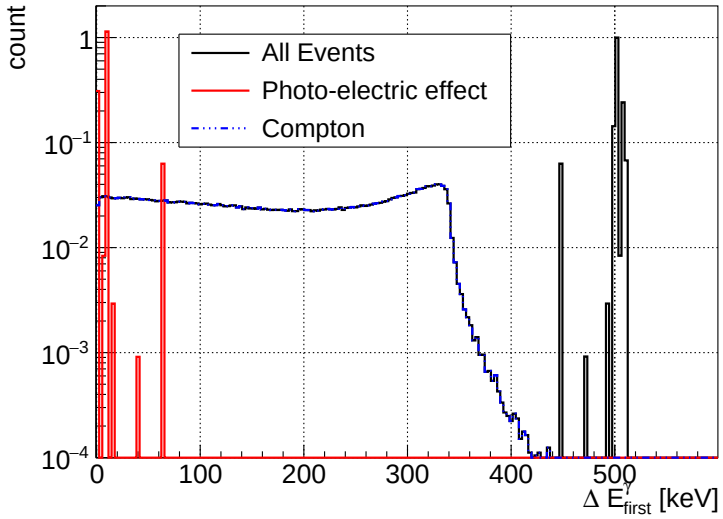

Figure 3.6: Energy losses and depositions in the LYSO crystals by gammas and electrons.

The blue histogram contains the energy loss of the initial gammas which had a Compton scattering interaction as the first interaction. The Compton continuum here overlaps with the Compton continuum of the black histogram.

The red histogram shows the deposited energy of the initial gamma for the photoelectric effect. The reason for the low values of the deposited energy of the gamma rays is a technical one. In Geant4, a gamma ray which undergoes an interaction through the photoelectric effect will only have an energy deposition which equals to the binding energy of the electron. The remainder of the gamma energy is simply transferred to the electron in the form of kinetic energy.

3.2.3 Photon Production

In section 3.1.3 the LYSO emission spectrum and SiPM PDE spectrum were shown in fig. 3.3. Two types of simulations are performed:

- Direct optical photon generation inside the scintillation crystal.
- Generation of a uniform flux of gammas towards the scintillation crystal.

The direct optical photon generation allows to study light sharing effects without interference of the gamma interaction effects. Optical photons were generated inside the scintillation crystal by first generating a random emission point inside the scintillation crystal volume. From each emission point a set number of photons were generated, each having a randomized direction and a wavelength of 420 nm. The number of generated photons was set to the expected number of photons which had the potential to be detected by the SiPM array. In other words, the number of photons with a wavelength of 420 nm emitted by LYSO for an energy deposit of 511 keV, was corrected with the PDE at 420 nm.

Properties for each generated photon were produced according to the procedure employed by Geant4 for generation of scintillation photons. This procedure creates a 4π isotropic distribution with linear polarization by generating two random parameters $\cos\theta$ and ϕ as follows

$$\cos\theta = 1 - 2 \cdot r_1, \tag{3.4}$$

$$\phi = 2 \cdot \pi \cdot r_2, \tag{3.5}$$

with r_1 and r_2 randomly generated numbers in the range $]0, 1[$. The photon momentum $\vec{p}_{phot}$ is then given by

$$\vec{p}_{phot} = (\sin\theta \cdot \cos\phi; \sin\theta \cdot \sin\phi; \cos\theta) \ . \tag{3.6}$$

Polarization of the photon is given by the vector lying in the plane perpendicular to $\vec{p}_{phot}$. The polarization vector $\vec{v}_{pol}$ is constructed by making a

linear combination of the vector $\vec{p}^{\perp}_{phot}$ and $\vec{p}_{cross}$. Both vectors $\vec{p}^{\perp}_{phot}$ and $\vec{p}_{cross}$ are given by

$$\vec{p}^{\perp}_{phot} = (\cos\theta \cdot \cos\phi; \cos\theta \cdot \sin\phi; -\sin\theta) \ , \tag{3.7}$$

$$\vec{p}_{cross} = \vec{p}_{phot} \times \vec{p}^{\perp}_{phot} \ . \tag{3.8}$$

A new random number is generated in the range $[0, 1]$ which provides a random generated ϕ similarly as for eq. (3.5). This new ϕ then allows to create a vector with a randomized direction lying in the plane perpendicular to $\vec{p}_{phot}$. The polarization of the generated photon is then given by

$$\vec{v}_{pol} = \cos\phi \cdot \vec{p}^{\perp}_{phot} + \sin\phi \cdot \vec{p}_{cross} \ . \tag{3.9}$$

The generation of a uniform flux of gamma rays in the second type of simulation differs from the first simulation type in that gamma rays are generated outside the scintillation crystal. These gamma rays are given a momentum directed towards the scintillation crystal. At each step along the gamma track, Geant4 randomly determines if the gamma interacts with the surrounding material. When the gamma interacts, the type of interaction is randomly determined based on the material composition, defined in section 3.1.3, and the provided EPDL97 cross sections [37, 39].

Gamma rays interacting inside the LYSO scintillation crystal will transfer part or all of its energy to an electron. These electrons undergo interactions with the surrounding material through which they lose energy. Energy losses of the electrons can result in the production of:

- scintillation photons,
- secondary electrons,
- bremsstrahlung.

The number of scintillation photons produced is determined by the electron energy loss during that interaction. Secondary electrons will undergo the same types of interactions up to the point that all the initial energy has been converted to scintillation photons or bremsstrahlung. Bremsstrahlung itself will either be reabsorbed by the crystal or escape it.

In addition to the processes described above, the initial gamma interaction will leave one or more of the atoms of the scintillator material in an excited state. De-excitation of these atoms will produce secondary gammas which have the potential to escape the scintillator crystal. The maximum energy of these secondary gammas is 63.314 keV. As a result, the majority of these secondary gammas are reabsorbed in the crystal and produce scintillation photons.

3.2.4 Energy Resolution

One of the crucial properties of a PET module is the energy resolution. The energy resolution of the module is a combination of the intrinsic scintillator resolution, the effects of photon collection efficiency, the detection efficiency of the photo detector, and the excess noise factor (ENF) of the SiPM devices in the SiPM array.

Regardless of the energy resolution of a PET module, a portion of in-tissue Compton scattered gamma rays will still produce signals that are large enough to fall within the photopeak. These scattered gamma rays cause the detected LOR of the PET event to diverge from the true LOR with the obvious consequence of a degraded reconstruction resolution. However, a better energy resolution will reduce the error between the detected LOR and true LOR by reducing the energy window of acceptance of in-tissue Compton scattered events.

To ensure that the simulation is producing realistic energy resolutions $\Delta E_{\text{FWHM}}/E$ the following histograms are created:

- Generated photons from a gamma interaction, fig. 3.7
- Propagated photons detected by the SiPM array, fig. 3.8

From these histograms, the energy resolution of the scintillator crystal at photon generation, i.e. before application of the SiPM PDE and effects of light collection, and the final energy resolution of the full module were obtained. For this purpose the following equations were used to fit the photopeak eq. (3.10) and the Compton edge eq. (3.11).

$$F_{ppk}(x) = A_{ppk} \cdot \exp\left(-\frac{(x-\mu_{ppk})^2}{2\cdot\sigma_{ppk}^2}\right) \tag{3.10}$$

$$F_{\text{CE}}(x) = A_{\text{CE}} \cdot \left\{\int_x^{+\infty} \frac{1}{\sqrt{2\pi\sigma_{\text{CE}}^2}} \cdot \exp\left(-\frac{(x'-\mu_{\text{CE}})^2}{2\cdot\sigma_{\text{CE}}^2}\right)\cdot \mathrm{d}x'\right\} + B_{\text{CE}} \tag{3.11}$$

where $F_{ppk}(x)$ is a Gaussian distribution and $F_{\text{CE}}(x)$ represents the complementary cumulative Gaussian distribution `gaussian_cdf_c` from the `Math` library of the ROOT analysis framework.

The energy resolution (FWHM), is calculated from the results of the fit, $\Delta E/E = 2.355 \cdot \sigma/\mu$, and amounts to 8.30 % for generated photons and 11.14 % for photons detected by the SiPM array.

In fig. 3.7 the energy spectrum of gamma interactions in terms of the total number of produced photons is shown. The mean of the photopeak is situated around 16 345 photons, being quite well in agreement with the provided scintillation yield of 32 photons/keV (16 352 photons @ 511 keV)

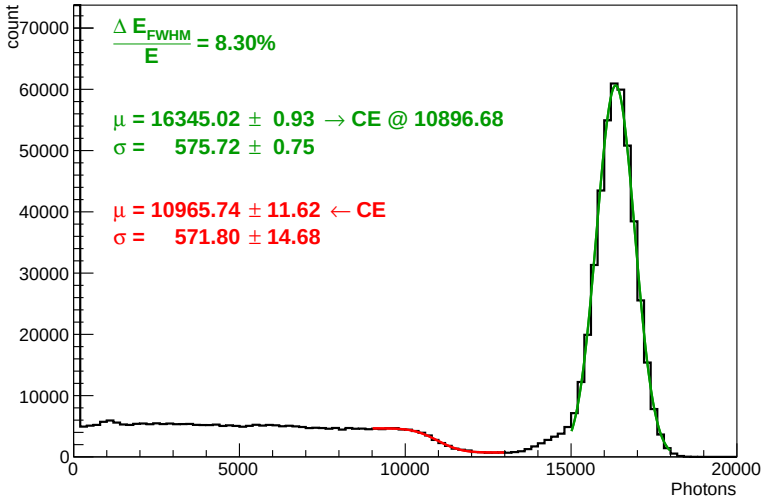

Figure 3.7: Energy spectrum of the produced scintillation photons obtained by binning the total number of photons that were produced after a gamma interacted with the crystal. Green: fit result for the photopeak, red: fit result for the Compton edge.

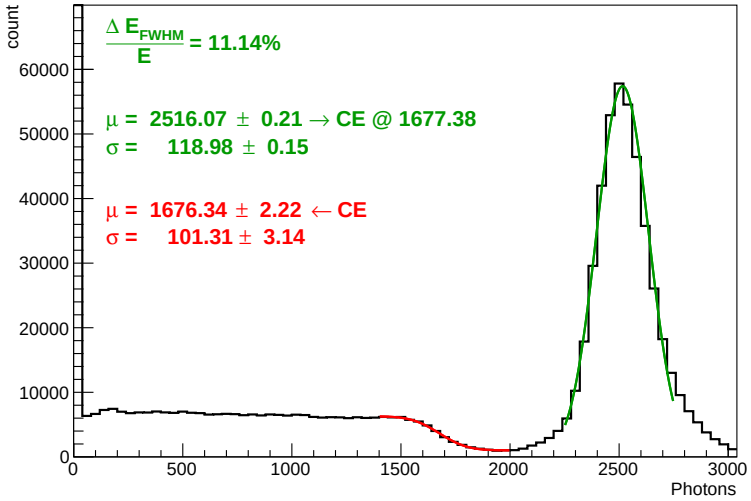

Figure 3.8: Energy spectrum obtained by binning the total number of photons being detected by the SiPM array for each event. Green: fit result for the photopeak, red: fit result for the Compton edge.

mentioned in section 3.1.3. The Compton edge (CE in fig. 3.7) only provides a cross-check to ensure that the system behaves linearly. The location of the Compton edge E_{CE} can be calculated based on the equation for the energy

E_{T} transferred during the scattering, given by

$$E_{\mathrm{T}} = \frac{E_\gamma^2 \cdot (1 - \cos(\theta))}{m_e c^2 + E_\gamma \cdot (1 - \cos(\theta))} \ , \tag{3.12}$$

and thus becomes maximal when θ =180°, i.e. for a back scattered gamma, resulting in

$$E_{\mathrm{CE}} = \frac{2 \cdot E_\gamma^2}{m_e c^2 + 2 \cdot E_\gamma} \ . \tag{3.13}$$

For a 511 keV gamma ray, $E_\gamma = m_e c^2$ such that the location of the Compton edge should be situated at $\mu_{\mathrm{CE}} = 2/3 \cdot \mu_{ppk}$. With a mean number of 16 345 photons (2516 detected photons) in the photopeak, the Compton edge should be situated around 10 896 photons (1677 photons resp.). From both fig. 3.7 and fig. 3.8 it is clear that the Compton edges are situated approximately at $\mu_{\mathrm{CE}} = 2/3 \cdot \mu_{ppk}$.

From the results discussed above, we can estimate the light collection efficiency of the scintillator. The collection equals to the ratio of detected photons and the PDE corrected number of generated photons (4465), 2516/4465≈56 %, which is in good agreement with results found in the literature [40].

Chapter 4

Reconstruction Methods

A 3D-reconstruction of the gamma interaction point requires a method to extract three coordinates from a limited set of parameters, i.e. detected number of photons per photodetector. Regardless of the method, it is necessary to understand the light sharing effects, in function of the gamma interaction point, on the set of parameters from which the interaction point will be extracted.

In this chapter, several methods for the reconstruction of the gamma interaction point are introduced and their baseline performances are studied on simulated events with single point photon emission. Two of the most commonly applied standard reconstruction methods are compared to newly proposed reconstruction methods developed to take advantage of the DOI encoded crystal structure.

This chapter handles the ideal case for a gamma interaction point. It represents a single gamma interaction from which all the scintillation photons are emitted. The location of photon emission in this case is limited to a single point inside the crystal volume. The results of these simulations then provide a baseline performance of the various reconstruction methods studied.

4.1 Photon Emission for the Ideal Case

Essential for PET is the ability to reconstruct the position of the gamma interaction in the plane of the detector. Simulations allow to carefully investigate the effects of light sharing over the SiPM channels and its influence on the determination of the position. Optical photons were generated at positions uniformly distributed inside the volume of the segmented crystal structure. The initial momentum directions of the scintillation photons were randomized as described in section 3.2.3. Based on their initial momentum directions they could be subdivided in the following two subgroups.

downwards: Towards the SiPM array

upwards: Away from the SiPM array

4.2 Standard Reconstruction

The two standard reconstruction methods which are studied represent the most commonly applied methods for the reconstruction of the gamma interaction point in PET cameras. The choice of the method mostly relies on the segmentation structure of the scintillator crystal combined with the layout of the photodetectors.

PET cameras which have a one-to-one mapping between the segments of the crystal and the photodetectors, generally rely on a maximum channel method. On the other hand, PET cameras which do not have a perfect one-to-one mapping, can rely on a center of gravity method due to light sharing effects between segments.

4.2.1 Maximum Channel Position

The most straightforward method to determine the emission point of the optical photons, is to assign it to the SiPM channel that detected the majority of the photons. In this method, the position in the plane of the SiPM array will be set to the center of the SiPM channel with the maximum number of detected photons. For the case of a one-to-one mapping between scintillation crystal and photodetector and no Compton scattering, this provides a discrete two dimensional position with a sigma of $3.2/\sqrt{12}$ =0.92 mm [41] (inter-channel distance 3.2 mm) per direction. For the PET module with the DOI encoded crystal structure, there will be an additional component to the resolution due to light sharing effects.

To determine the accuracy of the maximum channel position method, the area in the plane of the detector was divided into a tightly spaced grid. For each pixel of this grid the number of randomly generated positions in the pixel were counted. At each event the generated position was compared to the location of the maximum channel. If the location of the generated position was situated within the boundaries of the maximum channel, as determined by the SiPM array channel mapping, then the maximum channel position was considered a correctly identified event. In case the location of the generated position did not fall within the boundaries of the maximum channel, the event was considered to be wrongly identified. For these results all the generated photons (both downwards and upwards) were taken into account. In addition no separation between layers was made.

Eventually the numbers of correctly and incorrectly identified events were placed into a two-dimensional histogram where each pixel was normalised by dividing it by the total number of generated positions corresponding to that

Channel Number	All		Down		Up	
	μ	σ	μ	σ	μ	σ
10	90.62	3.02	87.00	5.69	76.08	7.76
11	79.39	8.04	81.64	7.68	46.40	4.48
14	77.04	8.37	84.48	5.52	41.24	6.53
15	73.37	9.02	82.61	6.79	35.59	6.05

Table 4.1: Efficiencies for correct reconstruction of the emission point for the maximum channel method according to the channel above which the generated position was situated.

pixel. The results are presented in fig. 4.1.

It is clear that for the central SiPM channels, the maximum channel method yields good results. However, near the boundaries of the channels there is a significant drop in efficiency for this method. For the outer channels the efficiency does not reach the same level as in the central channels. This can be attributed to the fact that part of the photons will always be reflected inwards and thus incorrectly give a higher weight to the central channels.

Generally an efficiency over 73 % can be achieved for the maximum channel positioning method. In table 4.1 the efficiencies are listed for each channel, in a single quadrant, above which the interaction occurs for different original directions of the photon momenta. The table also indicates that the upwards directed photons are the major contributor to misidentified events where especially the outer channels suffer from rather poor efficiencies.

In figs. 4.2a and 4.2b the wrongly identified events are shown for separating the photons based on their initial momenta. It shows that the downwards photons have a low probability to lead to a wrongly identified event except at the boundaries. The upward photons, on the other hand, have a very high probability to lead to a wrongly identified event, except in the innermost channels.

Ultimately, it is the accuracy in reconstructing the location of photon emission which is of importance. These results for the reconstruction efficiencies merely provide an insight into the regions were the maximum channel method encounters issues.

4.2.2 Center of Gravity

Due to the increasing segmentation along the depth of the scintillator crystal it is expected that the center of gravity would be distorted due to complex reflections on the reflector structure. For each event the mean position (center of gravity) was calculated according to the following formulas

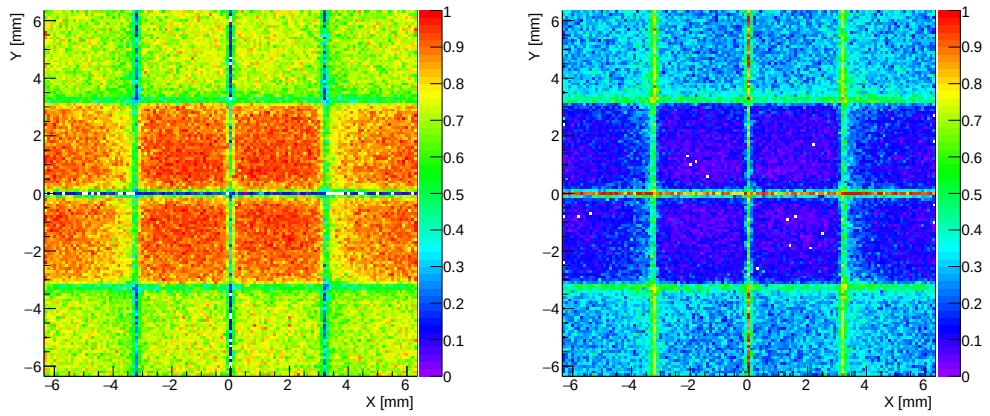

(a) **(b)**

Figure 4.1: Efficiency distributions as a function of the emission point for the maximum channel reconstruction for all photons. (a) Maximum channel corresponds to the emission point while in (b) the maximum channel does not correspond to the emission point.

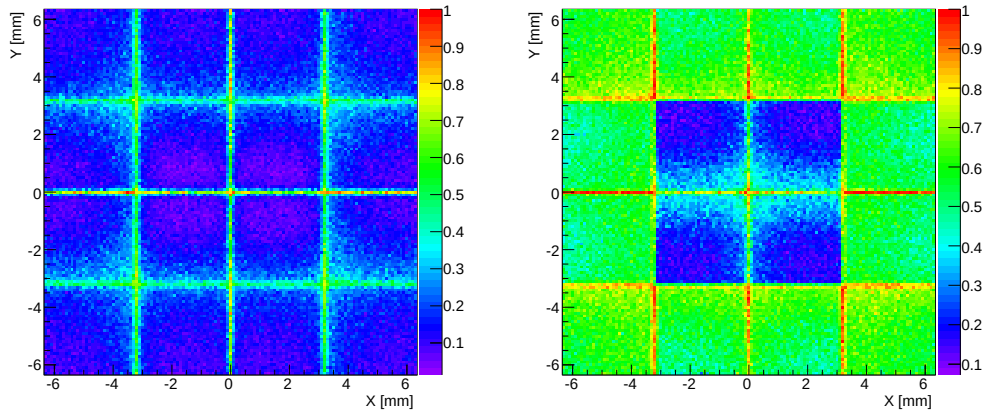

(a) **(b)**

Figure 4.2: Comparison of the wrong reconstruction probability for the maximum channel method as a function of the emission point between (a) the downwards and (b) upwards emitted photons.

$$X_\gamma = \frac{\sum_{i=0}^{15} N_i \cdot X_i}{\sum_{i=0}^{15} N_i} \quad \text{and} \quad Y_\gamma = \frac{\sum_{i=0}^{15} N_i \cdot Y_i}{\sum_{i=0}^{15} N_i} \ , \tag{4.1}$$

with the mean position (X_γ, Y_γ) given in function of the number of photons per channel N_i and the location of the center for each channel (X_i, Y_i).

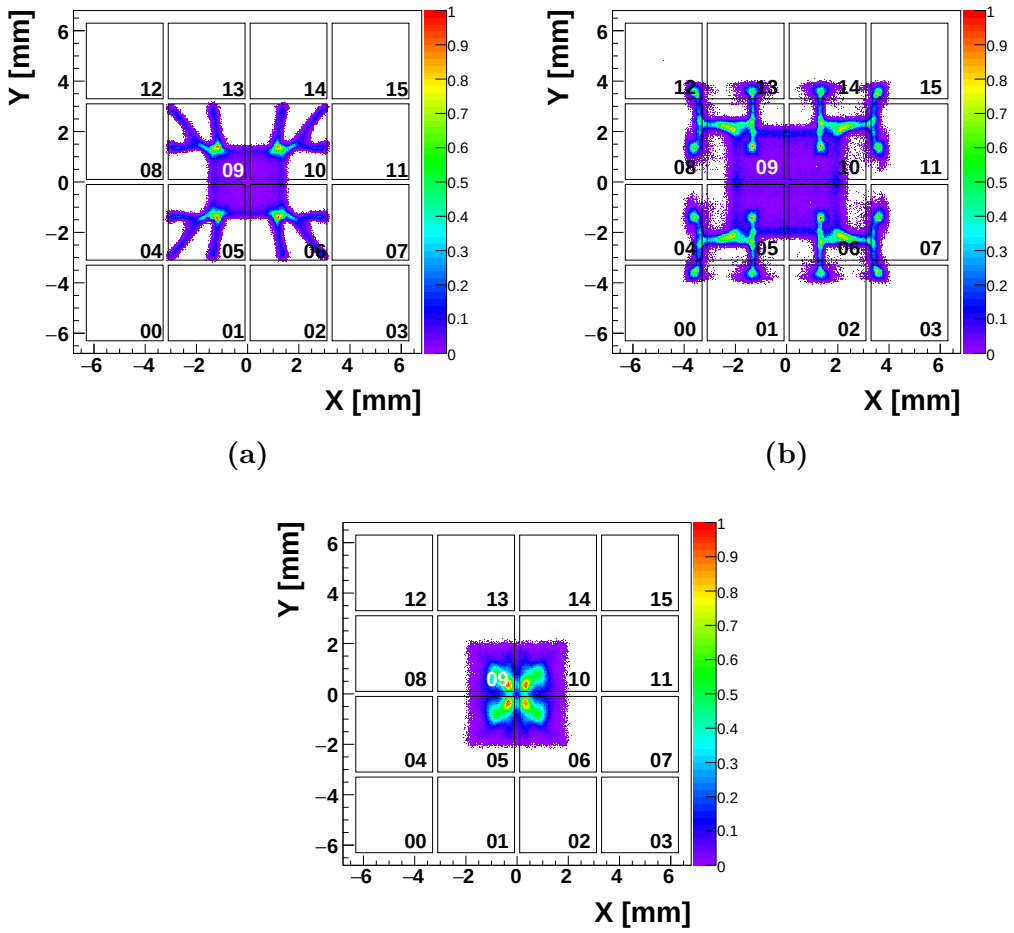

Figure 4.3: Mean positions per event for the cases: (a) all the emitted photons, (b) only downwards emitted photons taken into account, (c) only upwards emitted photons considered. The black squares represent the locations of the SiPM channels below the segmented crystal.

Results for the mean position are presented in fig. 4.3. The mean positions obtained for all the generated photons, i.e. both downwards and upwards, are shown in fig. 4.3a. It is clear that calculating the mean position using eq. (4.1) leads to severely distorted results. Overall the mean positions tend to cluster towards the center of the module, again indicating that reflections cause the inner channel to obtain a larger weight.

When only the downwards emitted photons are taken into account it still causes the mean position for an event to be shifted towards the center as can be seen in fig. 4.3b. This can be understood by the fact that for emission points occurring in the outer region of the segmented crystal, part of the

emitted photons will be detected by the central channels, but there are no SiPM channels beyond the outer region that can counterbalance the central channels. In addition, in the upper layers a part of the emitted photons will reflect off the sides of the segmented crystal back towards the central channels as discussed in appendix A.

For the case of the upwards emitted photons (fig. 4.3c) there is an even more apparent shift of the mean position towards the center. This can mostly be attributed to the upwards photons obtaining a more uniform spread over the SiPM channels due to the various possible reflections from the top and side crystal surfaces (see appendix A).

In appendix B, more details are provided for the correlation between the generated and calculated mean positions X and Y. From the results presented in the appendix, it is clear that the relation between the generated and calculated position is a multivalued function which makes it impossible to unambiguously correct the mean calculated positions. As a result, the center of gravity calculation can not be used in a reliable manner and thus an alternative method of position reconstruction is needed.

4.3 DOI Reconstruction

Aside the reconstruction methods described in sections 4.2.1 to 4.2.2 an additional method is required to reconstruct the depth of the interaction. The DOI encoding utilises a series of ratios of the SiPM channel signals. First the sum of channel signals for each quadrant (Q_q) and subquadrant (SQ_s) are calculated. Then the maximum channel (CH_{max}), quadrant (Q_{max}), and subquadrant (SQ_{max}) are determined to eventually calculate the previously defined set of ratios (see chapter 2),

$$R_1 = \frac{Q_{max}}{\sum_{q \neq max} Q_q} \ , \tag{4.2}$$

$$R_2 = \frac{Q_{max}}{CH_{max}} \ , \tag{4.3}$$

$$R_3 = \frac{SQ_{max}}{SQ_{neighbour}} \ . \tag{4.4}$$

The dependence of each one of the ratios R_r ($r = 1, 2, 3$) on the depth of interaction needs to be determined through simulations and experimental data. However, to use the ratios in further analysis the following 2 methods are used: ratio χ^2 and weighted ratio average.

Both methods require the extraction of a set of parameters from the data. In fig. 4.4, simulated data for the ratios R_r are presented. From these data the required set of parameters is extracted according to the following procedures.

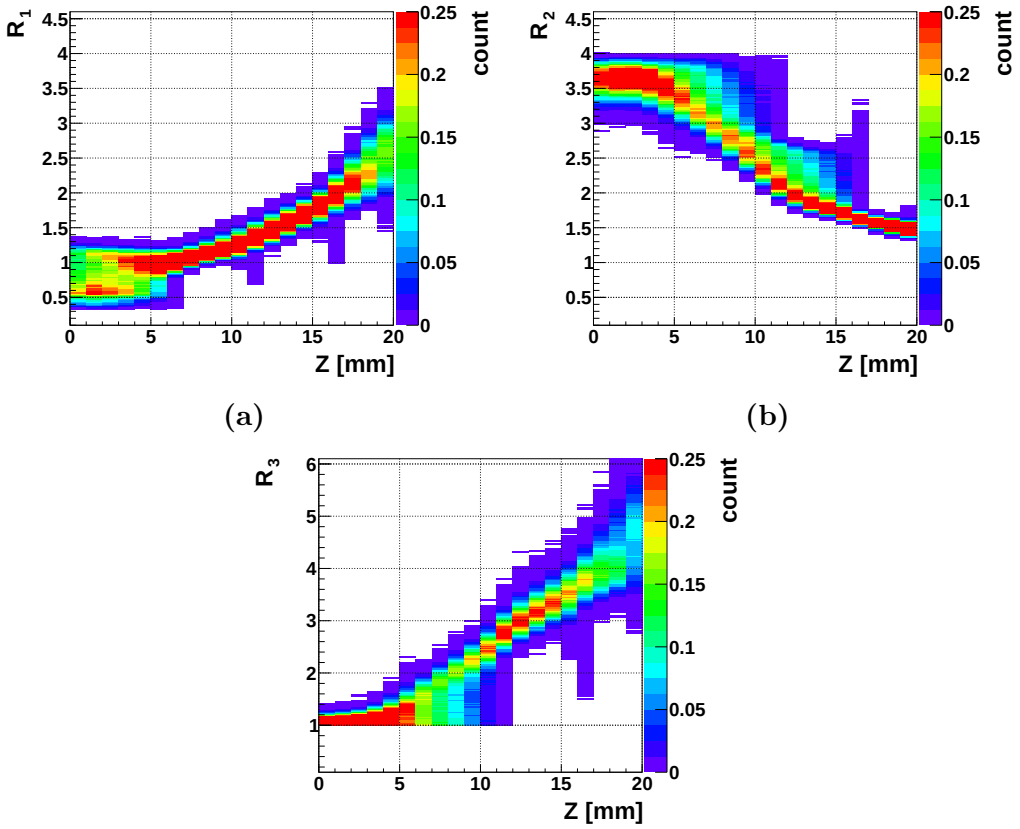

Figure 4.4: 2D histograms of the used ratios as a function of DOI for generated photons: (a) $R_1 = Q_{max}/\sum_{q \neq max}$, (b) $R_2 = Q_{max}/CH_{max}$, (c) $R_3 = SQ_{max}/SQ_{neighbour}$. The data presented in these figures where scaled to the entry with the maximum count and the color scale is limited to 0.25 to more clearly illustrate the features of the DOI ratios.

4.3.1 Ratio χ^2

This method divides the depth along the crystal into equally sized slices. Each slice has a position index p along the depth and a mean ($\overline{R_r^p}$) and RMS (σ_r^p) value for the ratio is appointed to the slice. The mean and RMS values are extracted from the data presented in fig. 4.4. This is done for each ratio R_r and at each position index p. Figure 4.5a show the results for the extracted mean and RMS values for each slice p where each slice has a thickness of 1 mm along the depth.

Once the mean $\overline{R_r^p}$ and RMS σ_r^p values for each slice p have been extracted, then during reconstruction of an event, for each slice p the following χ_p^2 value is calculated according to,

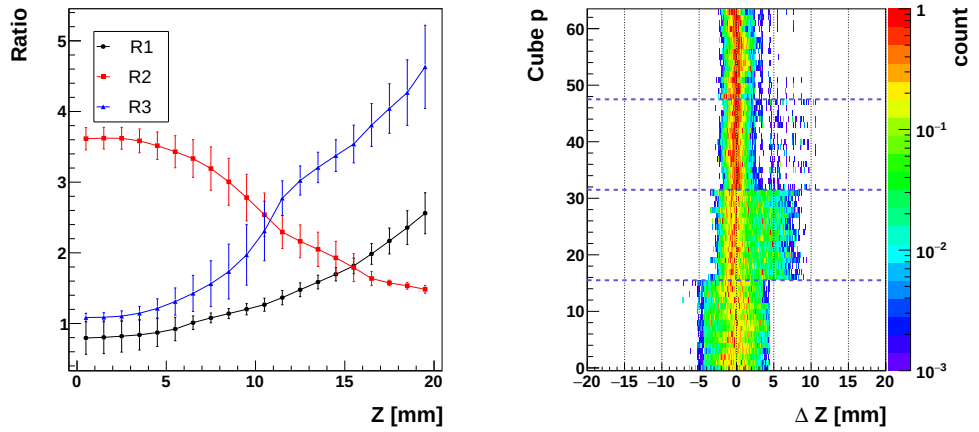

(a) **(b)**

Figure 4.5: Ratio χ^2 method results: (a) extracted values for mean ratio $\overline{R_r^p}$ with RMS σ_r^p (error bars). (b) distance between the generated and reconstructed DOI (Z) as a function of the generated cube index p.

$$\chi_p^2 = \sum_{r=1}^{3} \left(\frac{R_r - \overline{R_r^p}}{\sigma_r^p} \right)^2 , \tag{4.5}$$

where R_r represents the value of ratio $r = 1 \ldots 3$, while $\overline{R_r^p}$ and σ_r^p are the parameters previously extracted from the data.

Eventually the minimal χ_p^2 is then selected as the reconstructed position index along the depth where the gamma interaction occurred with the reconstructed Z_{reco} set to the center of the slice. In fig. 4.5b the distance in DOI between the generated position and the center of the reconstructed slice is shown, where ΔZ is defined as

$$\Delta Z = Z_{gen} - Z_{reco} , \tag{4.6}$$

with Z_{gen} the generated point of emission and Z_{reco} the reconstructed DOI. The distance histogram was normalised to the total number of generated events. From fig. 4.5b it follows that with the χ^2 method a high probability to correctly reconstruct the layer in which the interaction occurred can be obtained.

4.3.2 DOI Weighted Average

The DOI weighted average method for reconstructing the DOI works on a similar principle as the χ^2 method. As with the χ^2 method, the data

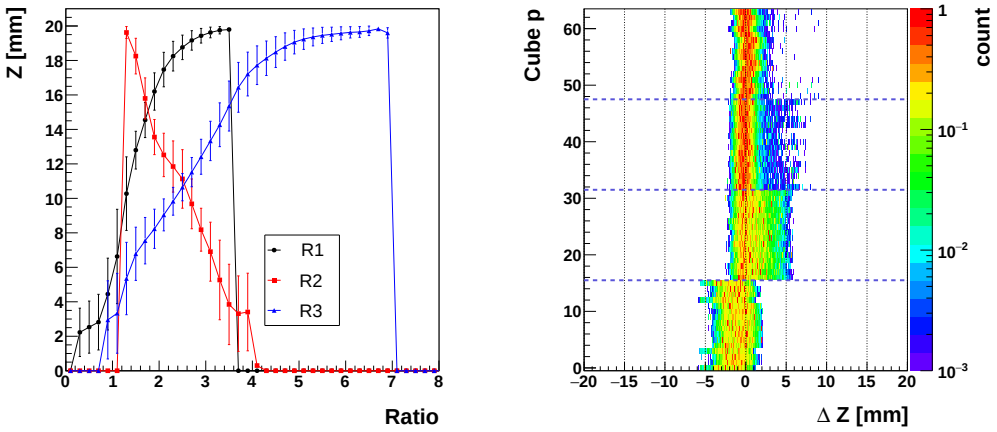

(a) (b)

Figure 4.6: Weighted average results: (a) extracted mean $\overline{Z_r^p}$ and RMS σ_r^p (error bars) value to be used to calculate the weighted average. (b) distance between the generated DOI (Z) location and weighted average (Z_γ) separated according to the cube of generation.

presented in fig. 4.4 is once again divided into equally sized slices. However, now the slices are made for the values of the ratios along the Y axis.

Once again, to each slice a mean ($\overline{Z_r^p}$) and RMS (σ_r^p) value is appointed. These values are extracted from the data shown in fig. 4.4. The results for this procedure are presented in fig. 4.6a.

In further analysis, during the reconstruction of an event, for each ratio R_r the slice p is determined to which the ratio R_r belongs. The previously determined mean ($\overline{Z_r^p}$) and RMS (σ_r^p) values for each ratio, associated to slice p, are then used to calculate a weighted average according to

$$Z_\gamma = \frac{\sum_{r=1}^{3} \frac{\overline{Z_r^p}}{(\sigma_r^p)^2}}{\sum_{r=1}^{3} \left(\frac{1}{\sigma_r^p}\right)^2} \tag{4.7}$$

Similarly as before, fig. 4.6b displays the results for the DOI distance between the generated and reconstructed DOI with ΔZ defined as

$$\Delta Z = Z_{gen} - Z_\gamma \ , \tag{4.8}$$

where Z_{gen} the generated point of emission and Z_{reco} the reconstructed DOI. The histogram was normalised to the total number of generated events.

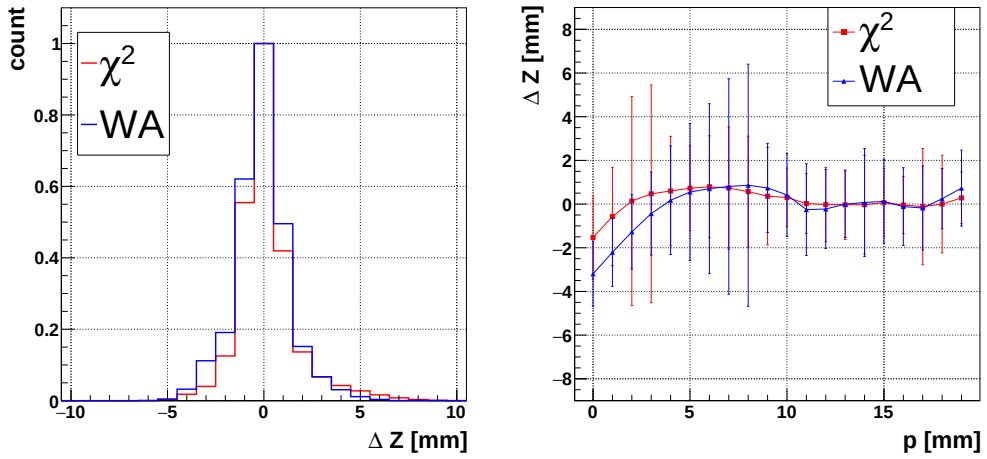

(a) (b)

Figure 4.7: Reconstruction resolution ΔZ for the ratio based methods: (a) combined result for all slices, and (b) mean and FWHM values for ΔZ as a function of the slice index p in which the emission point was situated.

These results indicate that for the top layer (L1), the weighted average method causes a general shift (≈2 mm–3 mm) of the reconstructed location towards a deeper DOI.

4.3.3 DOI Slice Reconstruction

The χ^2 method divides the crystal into equally sized slices along the length of the crystal. During reconstruction, the slice with the smallest χ^2 values is then taken as the reconstructed slice p_{reco}. Even though the weighted average method does not rely on these slice divisions, it is possible to identify the slice p_{reco} in which the reconstructed Z_γ is situated.

During reconstruction, the difference in slice index ΔZ between the slice of emission and the reconstructed slice is calculated, with ΔZ defined as:

$$\Delta Z = p_{em} - p_{reco} \ , \tag{4.9}$$

with p_{em} the slice of emission and p_{reco} the reconstructed slice. This difference in slice index ΔZ is calculated for both DOI reconstruction methods.

The results in fig. 4.7a indicate that both methods obtain similar slice reconstruction resolutions. Values for the FWHM and the full width at tenth maximum (FWTM) were extracted from these results through linear fits between the bins before and after the half maximum (10 % for FWTM) of the histogram. Such linear fits are performed both on the leading and trailing edges of the histograms. From these fits, the distance between the

points on the fit results which are at the exact half maximum (10 % resp.) are then taken as the FWHM (FWTM resp.).

With this method, the FWHM for the χ^2 method becomes 2.0 mm, while the weighted average has a FWHM of 2.3 mm. This minor difference is mostly related to the difference in the tails of both histograms, where the weighted average resolution has a higher weight in the tail towards the forward direction, i.e. left side. The FWTM values are 4.8 mm for the χ^2 and 5.8 mm for the weighted average which confirms the worse condition in the tails of the weighted average slice resolution.

A more detailed study of the difference in slice index is performed by producing ΔZ histograms for each slice. The values of ΔZ are filled into the histogram corresponding to the slice of emission. Afterwards, mean and FWHM values were extracted from each histogram. The results of this procedure are presented in fig. 4.7a with the FWHM added as errors to the mean values.

From these results, one can see that the left tail of the resolution in fig. 4.7a for the weighted average can mostly be attributed to the first layer (L1). The shift of the mean values for the weighted average method in the top layer clearly indicates a forward bias in this layer. Such forward bias is also present for the χ^2 method. However, there is nearly a factor 2 difference in resolution for nearly all slices in the first layer (L1). In the second layer (L2), both reconstruction methods tend to suffer from a backward bias, i.e. towards the entry face of the crystal. When the interaction point occurs close to the third layer (L3) or deeper, the slice reconstruction tends to correctly reconstruct the slice.

Values for the FWHM become quite large ($\approx$5 mm) for several slices in the first layer for the χ^2 method, but recover to reasonable values ($<$2 mm) around slice 4 (just in front of L2). The FWHM values for the weighted average are quite reasonable for the slices in the first layer ($<$2 mm) but drastically increase ($>$5 mm) in the second layer before dropping down to reasonable levels in the third layer.

4.4 Cube Reconstruction

In section 4.1 the DOI location is determined by separately reconstructing the position in the plane of the photodetectors (X_γ, Y_γ) and along the depth (Z_γ). This section describes a method where the DOI position is determined by dividing the scintillator crystal into equally sized volume elements and then estimating in which volume element the γ interaction occurred. In this entire section, box and layer will refer to the cube box and layer terms introduced in section 2.4.1.

4.4.1 Method

The crystal volume is divided into 64 equally sized cubes. The plane of the photodetector is divided into 16 equally sized boxes. Along the depth, the volume is divided into 4 equally sized layers. This provides a 3D grid with a pitch of 3.2 mm in the plane of the detector (X, Y) and 5 mm along the depth direction (Z).

To each cube j $(j = 0 \dots 63)$ we assigned two sets of 16 parameters, with each parameter being associated to a particular SiPM channel k $(k = 0 \dots 15)$. The k channel fraction f_k forms the basis for these sets of parameters, which is defined as

$$f_k = \frac{h_k}{\sum_{c=0}^{15} h_c} \ , \tag{4.10}$$

where h_k and h_c represent pedestal corrected SiPM channel signals. These channel fractions f_k depend on the effects of light sharing between the channels of the PET module.

For the first set of parameters, the mean of the k channel fraction $(\overline{f_k^j})$ is selected. The RMS (σ_k^j) of the k channel fraction is taken for the second set of parameters. These parameters are to be extracted from the simulation data prior to the reconstruction. Extraction of these parameters relies on the locations of the gamma interactions. The first phase for the cube reconstruction extracts the set of parameters for each cube. At this stage, a 2D histogram is produced for each cube j, where each histogram contains the channel fractions f_k $(k = 0 \dots 15)$ for the events with the gamma interaction occurring in cube j.

In fig. 4.8 an example for the channel fraction histograms are presented. They represent the histograms for the 16 cubes in the third layer (L3). The value of the channel fraction is marked on the X-axis, while SiPM channel index k is marked on the Y-axis. Finally, for each cube j, the mean $(\overline{f_k^j})$ and RMS (σ_k^j) values for each channel are extracted. In this manner, each cube obtains two sets of 16 parameters.

During the reconstruction phase, these sets of parameters are used to calculate the following χ^2 values,

$$\chi_j^2 = \sum_{k=0}^{15} \left(\frac{f_k - \overline{f_k^j}}{\sigma_k^j} \right)^2 \ , \tag{4.11}$$

which is calculated for each cube j and each event. Thus for each event 64 χ^2 values are obtained. Eventually, the cube with the minimal χ^2 value is selected as the reconstructed cube.

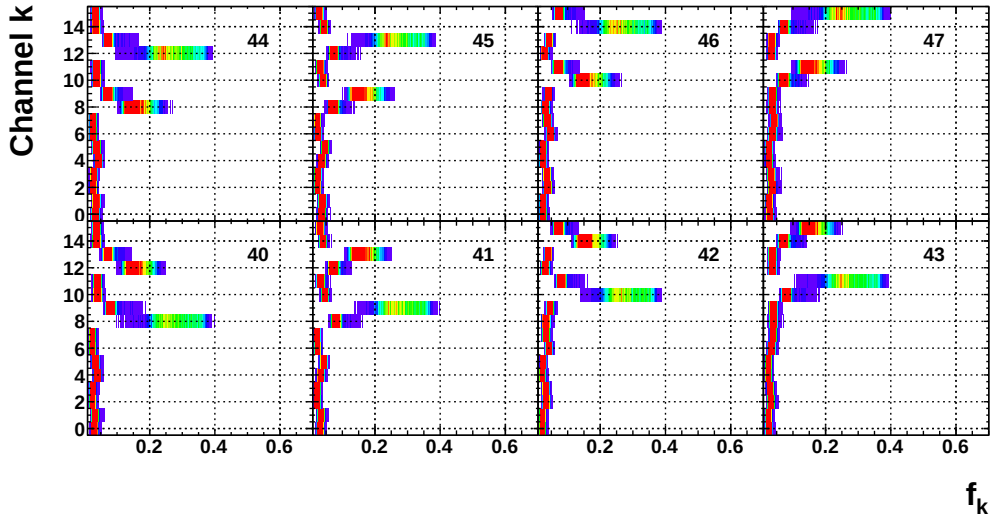

Figure 4.8: Examples of the Channel fractions f_k distributions for the boxes of the top two rows of cubes in the third layer with indices 40–47 as indicated in the figures.

Lets us illustrate this with a particular example: for each event which had the emission point generated in cube 41 (box 9 in L3), the difference between the χ^2 of cube 41 and all the other cubes was taken, with $\Delta\chi^2_p$ defined as

$$\Delta\chi^2_p = \chi^2_p - \chi^2_{41} \ . \tag{4.12}$$

The meaning of this parameter $\Delta\chi^2_p$ is that, if for a particular event, all values for $\Delta\chi^2_p$ are positive for all cubes p, then the cube reconstruction will have correctly reconstructed the cube for that event. On the other hand, a negative value of $\Delta\chi^2_p$ for a single cube p means that the cube reconstruction has incorrectly identified the cube for that particular event.

In fig. 4.9a those differences $\Delta\chi^2_p$ between all the cubes and cube 41 are shown. From this figure, we can see that there are some events where the cube is misidentified, i.e. negative $\Delta\chi^2$ values for the other cubes. While, for events generated in cube 41, some events are reconstructed towards upper layers $p < 41$ (away from the SiPM array), the majority of the misidentified events are reconstructed in a neighbouring cube $p = 45$ or in the lower layer $p > 47$.

Finally, projections from the data in fig. 4.9a are made of the neighbouring cubes of cube 41 and are shown in fig. 4.9b. These histograms are scaled to the total number of generated events in cube 41. The shown histograms correspond to the cubes 40–47 and follow the mapping as shown in fig. 2.6. These distributions show that mostly the cubes in the same SQ (top row

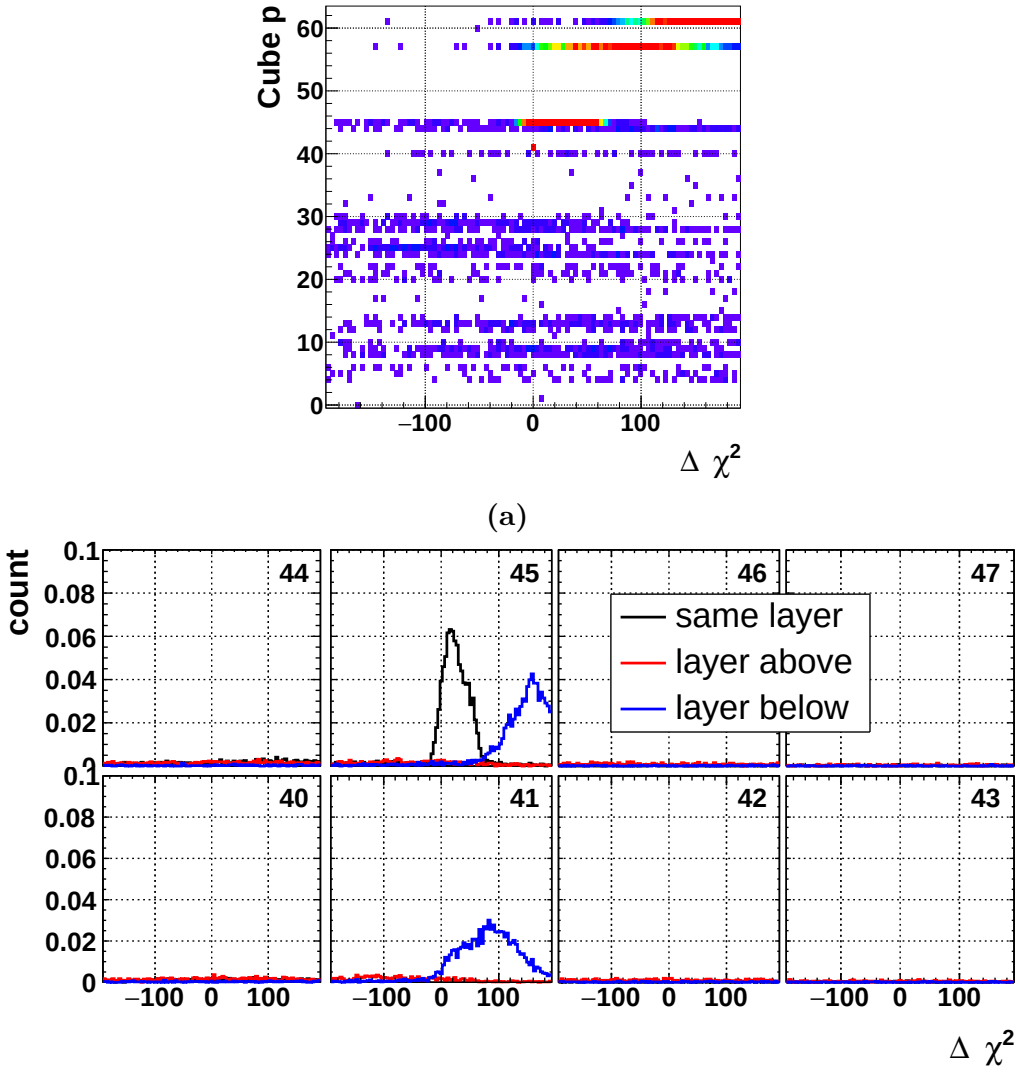

(a)

(b)

Figure 4.9: Examples of the $\Delta\chi^2$ distributions for the boxes of the top two rows of cubes (indexes 40–47) in the third layer: (a) $\Delta\chi^2$ distributions between the cube with index 41 (box 9 in L3) and all other cubes, (b) projections of the $\Delta\chi^2$ distributions of the neighbouring cubes of cube 41. The numbers inside the figures indicate the cube index p for which $\Delta\chi^2_p$ as defined in eq. (4.12) is shown.

second column) have χ^2 values which are close to the χ^2 of cube 41. The cubes situated in the layer above (red) and below (blue) have χ^2 which are not much larger than the values for cube 41. However, they rarely are smaller as indicated by the positive offset of those $\Delta\chi^2_p$ distributions.

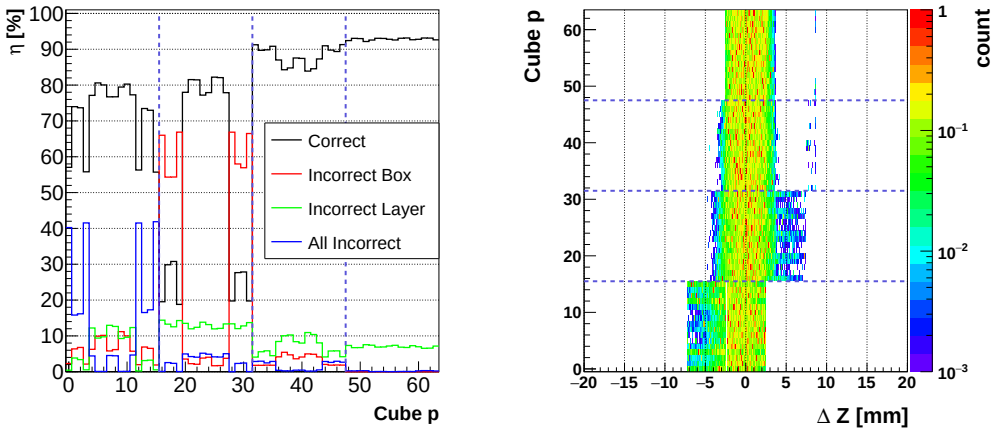

(a) (b)

Figure 4.10: General results for the cube reconstruction: (a) (in)efficiencies η for the reconstruction, (b) distances between the generated position and the center of the reconstructed cube for the 3 directions.

4.4.2 Reconstruction Efficiency

Efficiencies for the cube reconstruction are calculated by counting the number of times that the cube was correctly identified. The results are normalised to the number of generated events in the respective cube. Results of the efficiency versus the cube in which the event was generated are presented in fig. 4.10a. We subdivide the events into the following categories:

- Correct: correct layer, and correct box reconstruction
- Incorrect box: correct layer, but incorrect box reconstruction
- Incorrect layer: correct box, but incorrect layer reconstruction
- Incorrect layer and box: both box and layer were incorrectly reconstructed

In fig. 4.10a the X-axis shows the cube indices; aid lines (light blue) are provided to indicate which cubes belong together in a particular layer. From fig. 4.10a it is clear that the efficiency for correct box reconstruction suffers at the edges of the second layer.

Additionally, the distance ΔZ between the center of the reconstructed cube and the generated DOI position is presented in fig. 4.10b, with ΔZ given by

$$\Delta Z = Z_{gen} - Z_{reco} \ , \tag{4.13}$$

with Z_{gen} the generated point of emission and Z_{reco} the center of the reconstructed cube. It suggests that in the case of an erroneous cube reconstruction the reconstructed cube is prominently one of the neighbouring cubes.

4.4.3 Efficiency and Position

Simulations allow to study in detail how reconstruction efficiencies depend on the DOI location. The different (in)efficiencies as described in section 4.4.2 have been filled into 2D histograms separated for the four layers. Normalisation was performed by keeping track of the number of times an event was generated at particular generated (X, Y) positions. All figures are set to show the identical range for the efficiency going from 0 to 1.

The layer separation was made to obtain an insight to where the cube reconstruction performs well and where if fails to adequately reconstruct the cube. It is important to note that these histograms do not give any indication about the location of a wrongly reconstructed cube with respect to the generated cube.

Correct Reconstruction

In the case of a correct cube reconstruction the reconstructed cube matches with the cube in which the emission point was generated. From fig. 4.11 it is clear that primarily cubes situated at the outer corners or in the upper and lower row of cubes in the second layer show a reduced performance for the cube reconstruction.

Especially fig. 4.11b shows that the cubes in the top and bottom rows in layer 2 suffer from seriously reduced reconstruction efficiencies. This can also be seen in fig. 4.10a where the efficiency drops at the start and end of layer 2.

Incorrect Box

The incorrect box reconstructions displayed in fig. 4.12, present results for the reconstructions where the box was wrongly identified. In this case the reconstruction did identify the layer correctly.

From these results it is clear that the reconstruction efficiency for the box mostly suffers at box boundaries. In addition, layer 2 shows a high probability for incorrectly reconstructing the box for the top and bottom rows of boxes, see fig. 4.12b. This can be understood as scintillation photons having a greater probability to be reflected from the side reflectors towards the central row of boxes. Layer 2 namely consists of quadrants which are located just above the subquadrants in layer 3. The subquadrants allow light sharing to occur between the rows, while strongly reducing the light sharing between columns.

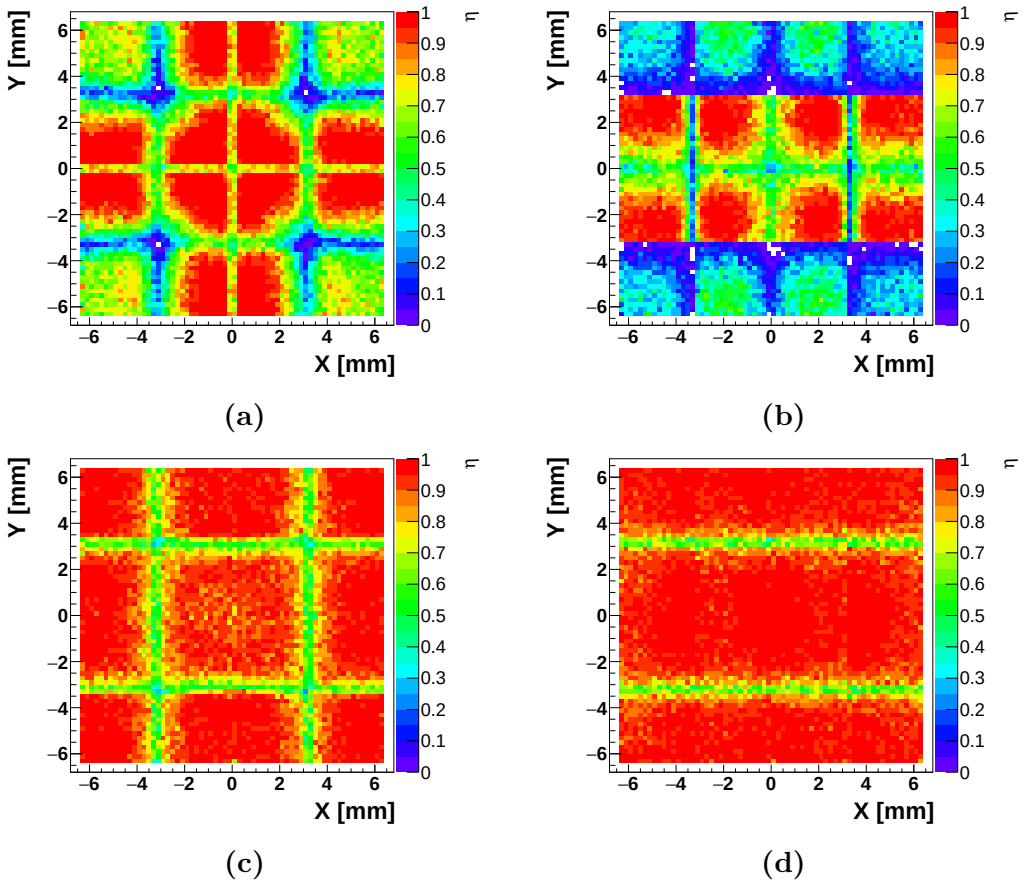

Figure 4.11: Reconstruction efficiencies as a function of the generated (X, Y) position for the correctly reconstructed events: (a) Layer 1, (b) Layer 2, (c) Layer 3, (d) Layer 4.

Finally, the bottom layer (4) has a very low probability to wrongly identify the box resulting in no misidentified events for the current data sets. This is due to the emission point being very close to a SiPM channel situated just below that particular box. The result is a large photon fraction f_k being measured by that particular SiPM. A large fraction f_k at one SiPM simultaneously means small fractions at the other SiPMs. Hence, the cubes in the lower layers have large values for the mean $\overline{f_k^j}$ and RMS σ_k^j which in turn leads to a minimal χ^2 for the cube in which the emission point is situated.

Incorrect Layer

Incorrect identification of the layer while correctly identifying the box primarily fails in the central region for top two layers, i.e. layer 1 and 2, see fig. 4.13a and fig. 4.13b. Both layers suffer mostly at the inner reflector boundaries. Layer 1 suffers the most at the crossing of the two reflector boundaries at

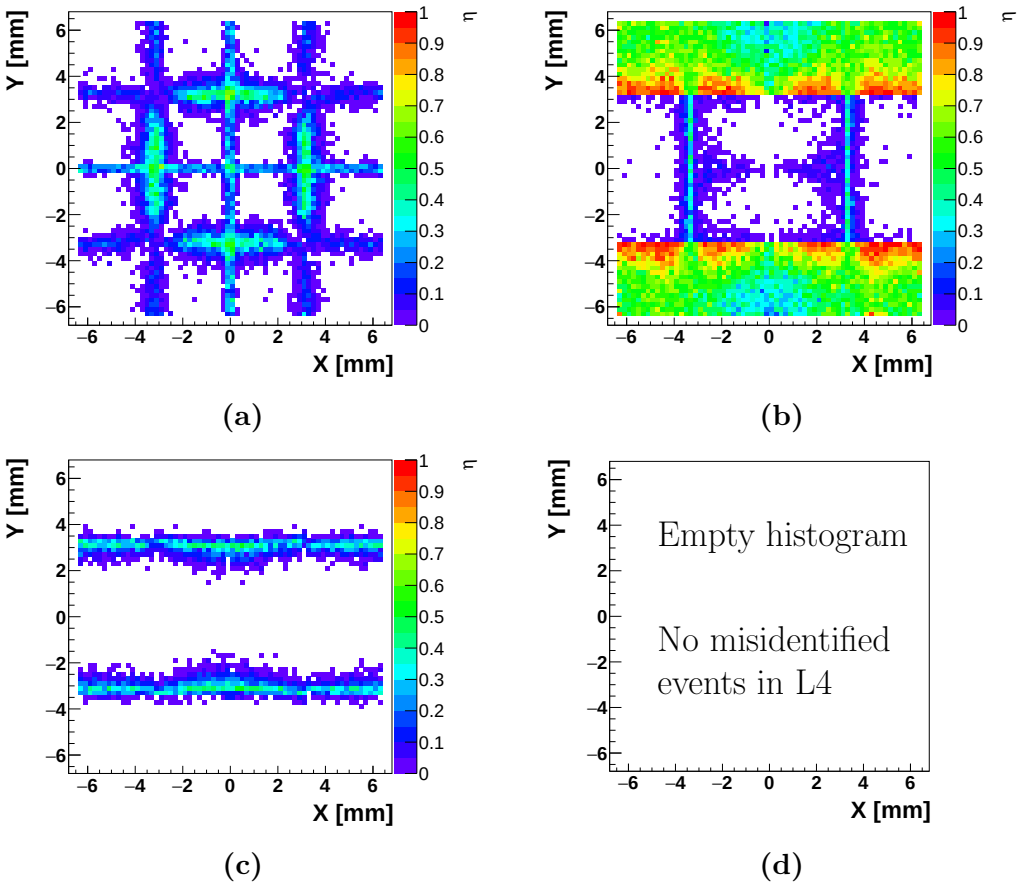

Figure 4.12: Misidentification probabilities as a function of the generated (X, Y) position for events with an incorrectly identified box and correctly identified layer: (a) Layer 1, (b) Layer 2, (c) Layer 3, (d) Layer 4.

the center of each quadrant. Layer 2 on the other hand, suffers at all the reflector boundaries, except the outer reflective wall. From fig. 4.10b we can deduce that for incorrectly identified layers, the reconstruction leads to either a higher or lower layer.

Incorrect Box and Layer

Figure 4.14 holds the reconstruction inefficiencies for the case that both the box and layer were incorrectly identified. Similarly for the other misidentification situations, i.e. wrong box or layer, the cube reconstruction fails to identify the correct cube mostly at reflector boundaries. Especially the top layer (L1) suffers the most from an incorrectly identified box and layer simultaneously.

Most of the misidentification can be attributed to the mismatch between the cube geometry and the scintillator crystal structure. This mismatch in

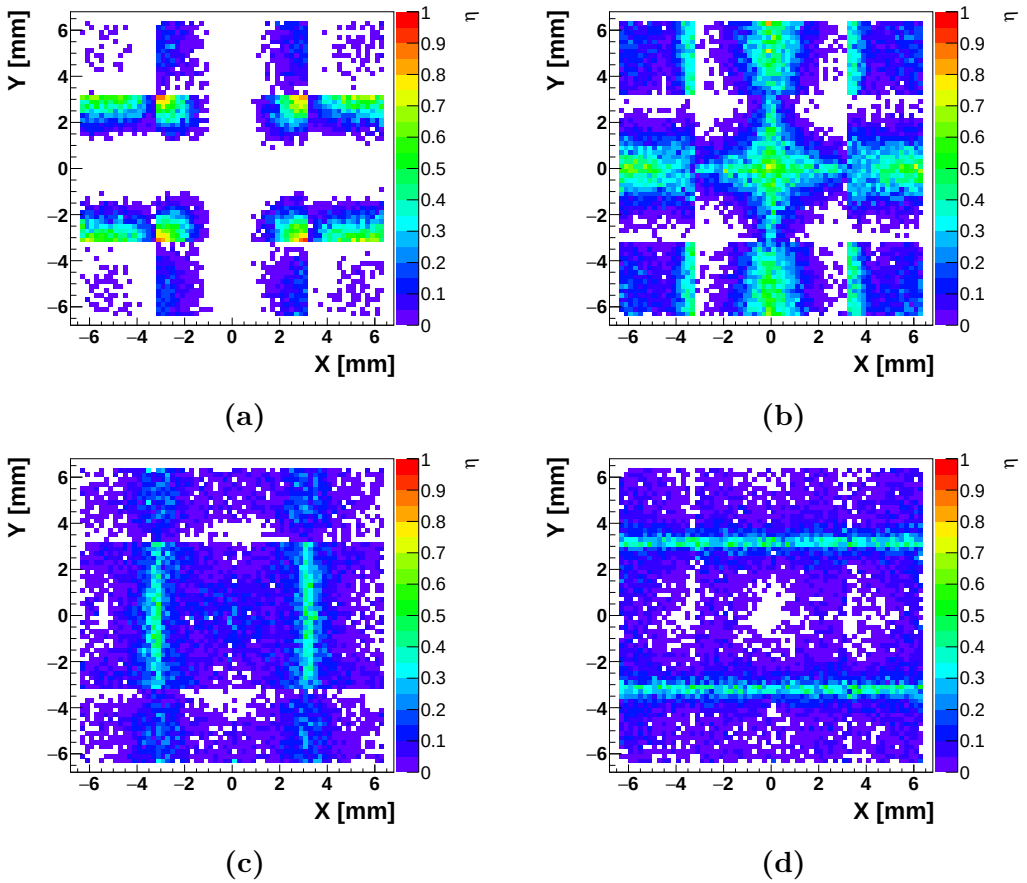

Figure 4.13: Misidentification probabilities as a function of the generated (X, Y) position for events with an incorrectly identified layer and correctly identified box: (a) Layer 1, (b) Layer 2, (c) Layer 3, (d) Layer 4.

geometry results in small expansion volumes being present at the crossing between the layers. These expansion volumes allows the scintillation light to spread out more over the underlying segments causing the differences in χ^2 values for the cubes near the interaction point to be small. These small differences in χ^2 values ultimately lead to the occasional misidentification of the cube.

4.5 Comparison of Reconstruction Methods

The least suited reconstruction method is the center of gravity method. As illustrated in fig. 4.3a it suffers from a strong compression towards the center of the module. Introduction of a scaling factor to compensate for the compression is a non-trivial task. From figs. B.2 and B.3 it is clear that the inward compression of the center of gravity is strongly correlated with the

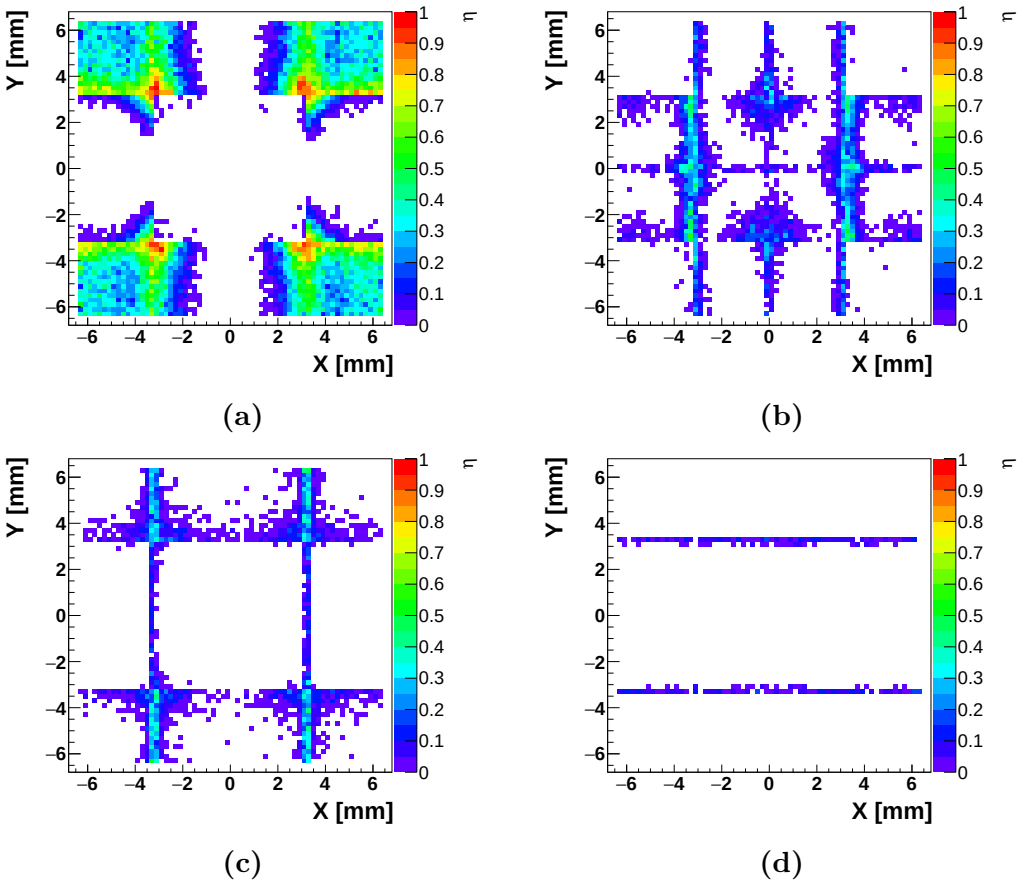

Figure 4.14: Misidentification probabilities as a function of the generated (X, Y) position for events with incorrectly identified box and layer: (a) Layer 1, (b) Layer 2, (c) Layer 3, (d) Layer 4.

DOI. In particular layer 2, as well as layer 3 for the Y direction, exhibit a nearly flat correlation between the true and calculated mean positions. As a result it is not possible to introduce a compensation method for those layers.

The DOI reconstruction methods described in sections 4.3.1 and 4.3.2, i.e. the χ^2 and weighted average methods, by themselves only provide a reconstruction of the emission point along the depth of the scintillation crystal. Therefore both methods rely on another method to reconstruct the location of emission in the plane of the detector. Two options exist: determine the (X_γ, Y_γ) through the maximum channel method or the cube reconstruction method.

A comparison of the resolution in the (X, Y) plane is made between the maximum channel and the cube reconstruction methods. The differences ΔX and ΔY are defined as

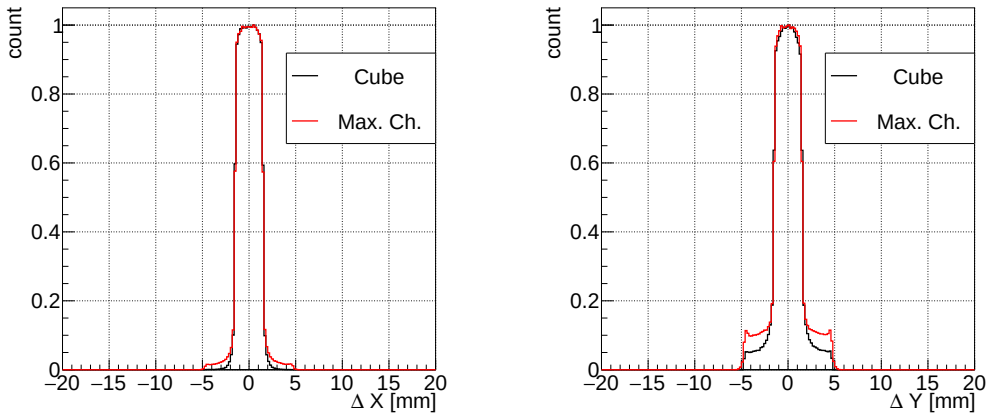

(a) **(b)**

Figure 4.15: Comparison of the (X, Y) resolution between the maximum channel and cube reconstruction methods: (a) ΔX, and (b) ΔY.

$$\Delta X = X_{gen} - X_{reco} \ , \tag{4.14}$$
$$\Delta Y = Y_{gen} - Y_{reco} \ , \tag{4.15}$$

with X_{gen} and Y_{gen} (X_{reco} and Y_{reco}) the (X, Y) coordinates of the generated (reconstructed resp.) emission point.

From fig. 4.15 it is clear that both methods achieve roughly the same resolution of 3.1 mm at FWHM. The main difference between both methods is the minor reduction of the tails for the cube reconstruction.

Finally a comparison is made between the three reconstruction methods for the DOI, i.e. the χ^2, the weighted average, and the cube reconstruction methods. Figure 4.16a presents the mean values of ΔZ as a function of cube index, where the index corresponds to the cube in which the emission point was generated. These mean values for ΔZ, and their RMS, are extracted from the data presented in figs. 4.5b, 4.6b and 4.10b. It indicates that for interactions occurring in the top layer, the weighted average and cube reconstruction methods cause a minor shift of the reconstructed DOI, ≈1 mm to 2 mm, towards deeper values. Interactions in the second layer on the other hand will be shifted towards the entry face of the scintillation crystal. Reconstruction of interactions in the bottom two layers, layer 3 and 4, does not exhibit any offset. However, the cube reconstruction does show a considerably larger error compared to the other two reconstruction methods. The χ^2 method has a relatively small offset, <1 mm, for all layers.

Figure 4.16b provides the results for the DOI reconstruction resolution regardless of the location of interaction. Similarly as in fig. 4.16a the cube

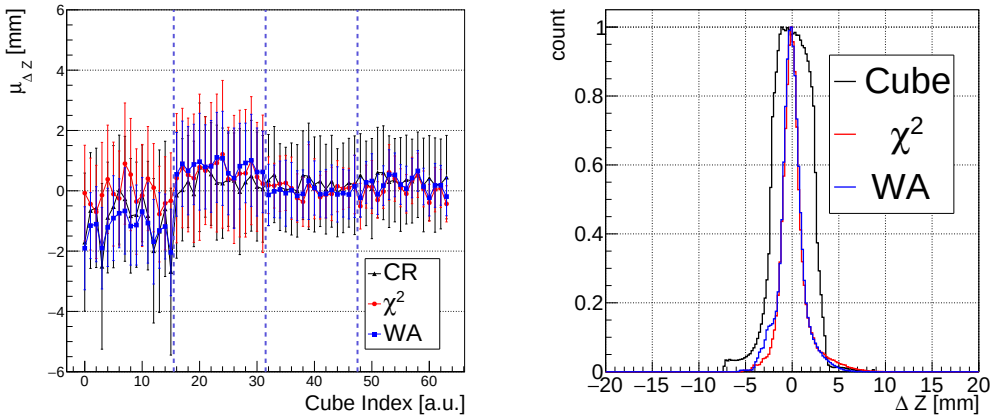

(a) **(b)**

Figure 4.16: Comparison of the DOI reconstruction between the three methods for uniformly distributed generation of optical photons. (a) Mean with RMS for the three methods as a function of cube index. (b) ΔZ for all reconstructed events.

reconstruction has the worst resolution, 4.9 mm FWHM, which is understandable considering that it is a discrete reconstruction method where the cubes have a width of 5 mm. Both the χ^2 and the weighted average reconstruction methods have similar results for the reconstruction resolution, 1.8 mm and 1.9 mm.

Chapter 5

Reconstruction with Simulated Gammas

In chapter 4, all the scintillation photons were generated from a single emission point in the scintillator crystal. This provides a baseline performance for the reconstruction methods discussed in chapter 4.

In reality however, gamma rays can undergo a series of Compton scatterings, potentially followed with the absorption of the remaining gamma through the photo-electric effect. Multiple gamma interactions cause scintillation photons to be created at several locations inside the scintillation crystal. This in turn results in the center of gravity of the measured light distribution to shift away from the location of the first gamma interaction.

For PET it would be best that the LOR for each PET event were constructed from the locations of the first gamma interactions in both PET modules. Unfortunately, due to the nature of gamma interactions in matter there will always be an error present in the LOR reconstruction.

This chapter focusses on the error introduced to the DOI reconstruction methods due to multiple gamma interactions. Several variations of simulations with gamma rays were performed, where for each simulation the analysis was done according to the methods discussed in chapter 4.

During analysis of the simulation data, the first step was to determine the parameters of the photopeak (PPK), i.e. μ_{ppk} and σ_{ppk}. Further analysis only takes into account those events with a measured number of photons which falls in the range $\mu_{ppk} \pm 2.355 \cdot \sigma_{ppk}$.

5.1 Gamma Ray Generation

For every simulation type, positions for the gamma rays are uniformly generated in a plane parallel to the front faces of the scintillator crystal. The plane from which primary gamma rays were generated was set at a distance

of 5 mm from the edge of the scintillator crystal. This limits the probability for Compton scattering before entering the PET module as it only goes through a very thin layer of air. A 5 mm distance between the starting position and the front face of the crystal leads to an air layer thickness of 4.8 mm (0.2 mm thick reflector).

In addition, simulations were done with gamma rays entering the scintillation crystal at an angle in the YZ plane, with respect to the normal of the front face of the crystal. These angles between the normal and the gamma ray momentum direction were varied in the range 0° to 30° with a step size of 7.5°.

5.2 Energy Weighted Interaction Point

In chapter 4 the baseline performance of the reconstruction methods was discussed through optical photon emission from a single location in the scintillator volume. However, in reality, gamma rays undergo multiple interactions inside the crystal volume. Each gamma ray interaction will cause an emission point for scintillation light to appear. The final measured light distribution is a superposition of the multiple emission points. Evidently, multiple gamma interactions will cause the center of gravity of the light distribution to shift away from the first gamma interaction.

To study the magnitude of the shift, it is important to keep in mind that each gamma interaction produces an electron. This electron in turn will deposit energy that eventually produces scintillation photons. In essence at each gamma interaction point there can be multiple points of photon emission. The number of scintillation photons emitted for each electron interaction directly depends on the energy deposited by the electron during the interaction.

For each event during the simulation, the number of gamma and electron interactions were recorded along with the energy deposited during the interaction. The center of gravity of the light distribution, further referred to as the energy weighted position $(X_{\text{EWP}}, Y_{\text{EWP}}, Z_{\text{EWP}})$, is defined as

$$(X_{\text{EWP}}, Y_{\text{EWP}}, Z_{\text{EWP}}) = \frac{\sum_i E^i_{e-dep} \cdot (X_i, Y_i, Z_i)}{\sum_i E^i_{e-dep}} \ , \tag{5.1}$$

where E^i_{e-dep} is the energy deposited by the electron at position (X_i, Y_i, Z_i) for the i-th electron interaction.

The difference $(\Delta X, \Delta Y, \Delta Z)$ between the first gamma interaction point $(X^{1^{st}}_\gamma, Y^{1^{st}}_\gamma, Z^{1^{st}}_\gamma)$ and the energy weighted position $(X_{\text{EWP}}, Y_{\text{EWP}}, Z_{\text{EWP}})$ is defined as

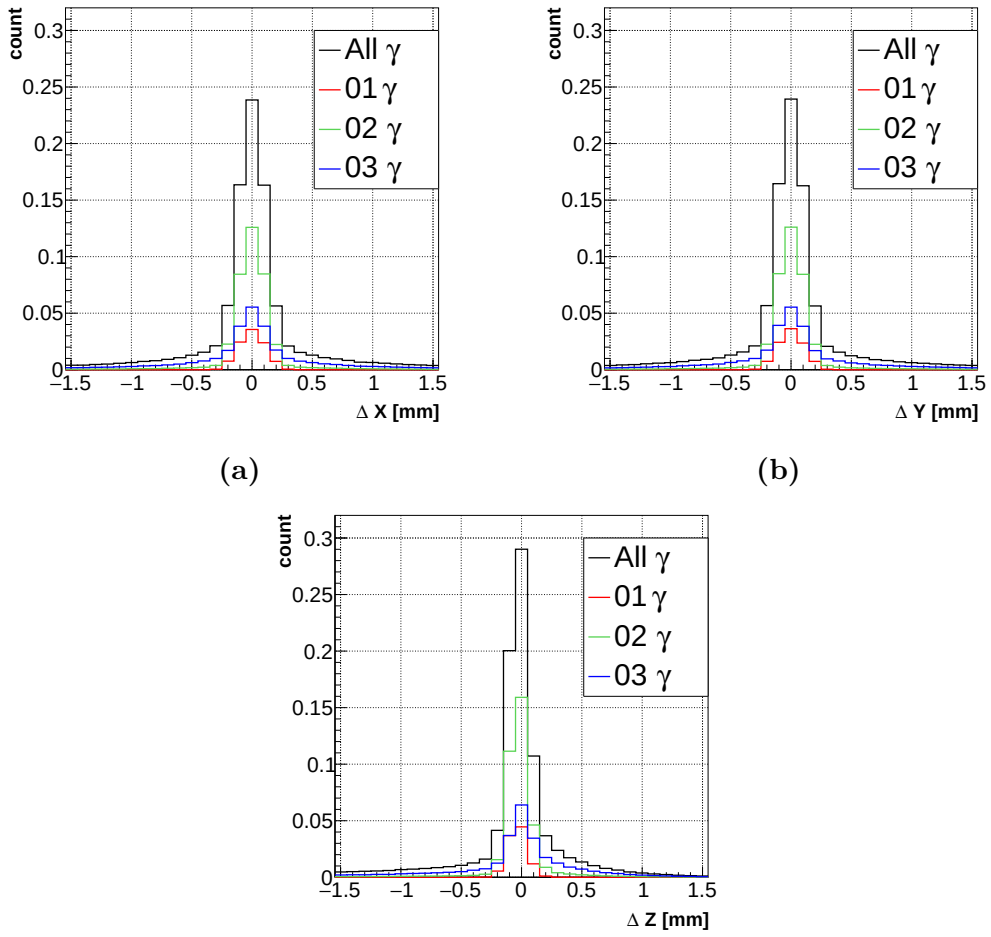

(a) **(b)**

(c)

Figure 5.1: Range between the first gamma interaction point and the energy weighted position: (a) direction along X, (b) direction along Y, and (c) direction along the depth, Z.

$$\Delta X = X_{\gamma}^{1^{st}} - X_{\text{EWP}} \ , \tag{5.2}$$

$$\Delta Y = Y_{\gamma}^{1^{st}} - Y_{\text{EWP}} \ , \tag{5.3}$$

$$\Delta Z = Z_{\gamma}^{1^{st}} - Z_{\text{EWP}} \ . \tag{5.4}$$

Results for the distance between the position of the first gamma interaction and the energy weighted position are presented in fig. 5.1. In addition, a separation was made between the events based on the number of gamma interactions that occurred during the event.

From fig. 5.1a and fig. 5.1b it is clear that the difference in segmentation between the X and Y directions does not lead to a difference in the range.

Number of γ interactions	X [mm]	Y [mm]	Z [mm]	fraction [%]
1	0.28	0.27	0.21	10
2	0.27	0.27	0.20	38
3	0.30	0.30	0.24	31
All	0.28	0.27	0.21	100

Table 5.1: Results for the range between the first gamma interaction point and the energy weighted position as a function of the number of gamma interactions.These results represent the fundamental limit that can be achieved for the position resolution.

This is to be expected considering that there is only a small difference in reflector volume between the two different segmentations.

As expected, the range between the first gamma interaction and the energy weighted positions is mostly limited to the electron range when there is only a single gamma interaction. When multiple gamma interactions are involved, the range increases due to the gamma ray being scattered in a random direction. In table 5.1, FWHM extracted values for these ranges are presented as a function of the number of gamma interactions which occurred during the event. From this table, we can see that this range is well below the dimensions of the elements of the PET module (i.e. Q, SQ, CH). The fractions indicated in the table are the number of events, in the PPK, with a certain number of gamma interactions which was then normalized to the total number of events in the PPK.

There is only a minor difference in the range between two gamma interactions and more than two interactions. While each gamma interaction, in an event, causes the energy weighted position to shift away from the first gamma interaction, the shift is limited by the dimensions of the crystal. Therefore, the gamma interactions after the first two interactions can only increase the tails, but not extend them.

Comparing the fraction of energy, f_{E}, deposited at the first gamma interaction point to the range $(\Delta X, \Delta Y, \Delta Z)$ provides the results presented in fig. 5.2. With f_{E} defined as

$$f_{\text{E}} = \frac{E_{\gamma-dep}^{1^{st}}}{511\,\text{keV}} \ . \tag{5.5}$$

From the results shown in fig. 5.2, it follows that the tails for the range can mostly be attributed to events where only a small fraction of the energy is deposited in the first gamma interaction. This is consistent with a shallow

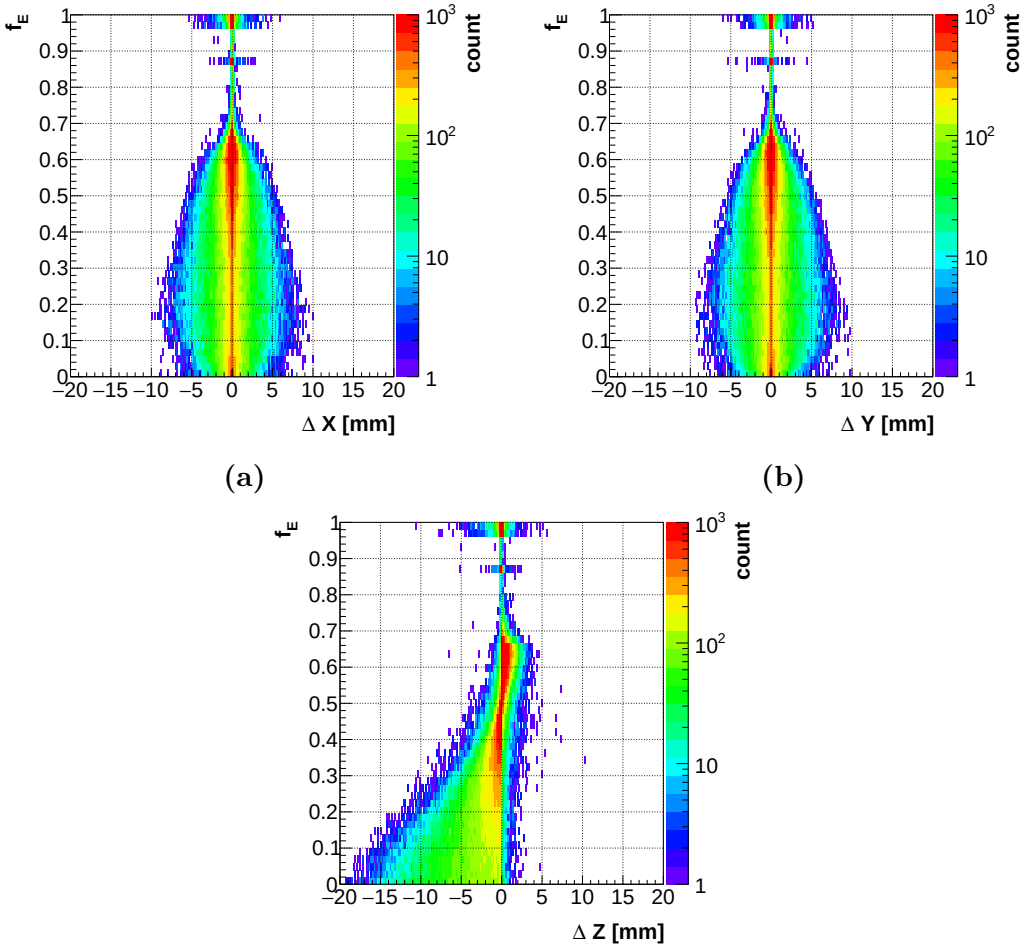

Figure 5.2: Range between the first gamma interaction point and the energy weighted position as a function of the fraction of energy deposited at the first gamma interaction point: (a) direction along X, (b) direction along Y, and (c) direction along the depth, Z.

angle Compton scattering. Shallow angle Compton scattered gamma rays have a larger remaining energy and thus have a larger attenuation length. Larger attenuation lengths in turn translate to a larger range between the first gamma interaction point and energy weighted position.

A small energy deposition at the first gamma interaction results in a considerable tail for the range along the Z direction, see fig. 5.2c. As expected, those first interactions with a low f_{E} correspond with forward scattered gamma rays, i.e. $Z_{\text{EWP}} > Z_{\gamma}^{1^{st}}$, and thus they have a greater probability to deposited more energy deeper inside the scintillation crystal.

Based on eq. (3.12), the energy fraction f_{E} at which the Compton scattered gamma is neither forward nor backward scattered can be calculated by

setting $\theta = 90°$, giving

$$E_{\mathrm{T}} = \frac{E_\gamma^2}{2 \cdot E_\gamma} \ , \tag{5.6}$$

keeping in mind that $E_\gamma = m_e c^2$. Thus at an energy fraction $f_{\mathrm{E}} = 0.5$ there should be a turn point at which the gamma will go from forward scattering to backscattering. In fig. 5.2c there is indeed a turn point present at $f_{\mathrm{E}} = 0.5$ where the tail for the range switches from predominantly negative values for ΔZ to positive values, i.e. from forward to backscattered gamma rays.

5.3 Reconstruction

The methods explained in chapter 4 are now applied to the events with the more realistic gamma interaction as opposed to a single emission point per event as was the case in chapter 4. Each of the methods described in section 4.3 and section 4.4, relies on a set of parameters specific to the method to be able to perform the reconstruction.

In chapter 4 those parameters were extracted from the data itself by relying on the presence of the emission point location. Now a choice for the sets of parameters can be made. It is possible to reuse the sets of parameters form chapter 4 or new sets can be extracted from the data. Extracting new sets of parameters from the simulation data with a gamma source, once again presents two possibilities in terms of the point of reference to which the sets are produced. Ideally the sets of parameters would be produced with the first gamma interaction location as reference. However, the energy weighted position should be more closely correlated to the center of gravity of the light distribution. During reconstruction, the aim is to reconstruct the first gamma interaction point and thus the results for efficiency and resolution of the reconstruction are taken to be relative to the first gamma interaction point. Here, a comparison is made for the all reconstruction methods with the different sets of reconstruction parameters.

5.3.1 Ratios Based Reconstruction

Reconstruction resolutions were determined for the ratio based DOI reconstruction in a similar fashion as described in section 4.3.3. These resolutions are in terms of the slices as they are defined for the χ^2 method, see section 4.3.1. In an identical manner, the difference in slice index ΔZ between true and reconstructed indices were calculated. The definition of ΔZ is similar as eq. (4.9), however, the slice of emission p_{em} is replaced by the slice $p_\gamma^{1^{st}}$ where the first interaction occurred, i.e.

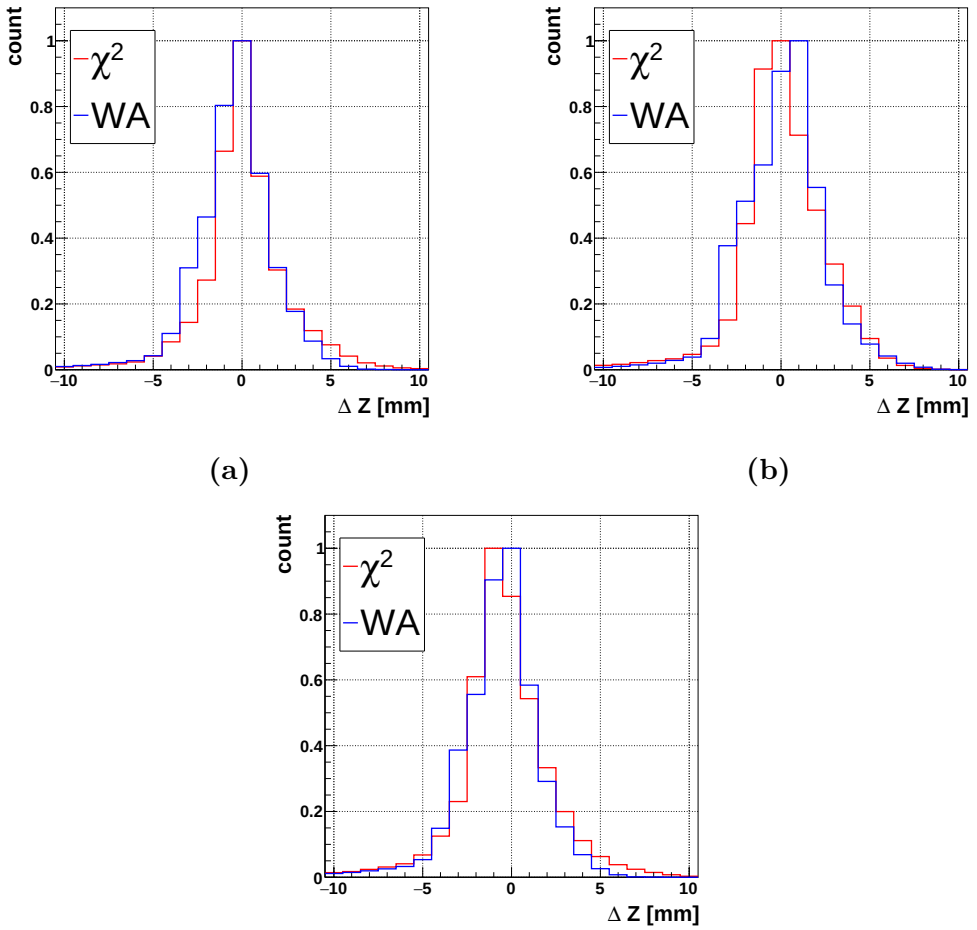

Figure 5.3: Differences in slice index ΔZ for the ratio based reconstruction methods performed with three variations of parameter sets which were extracted from: (a) simulation data with a photon source, (b) gamma ray simulation data with the first gamma interaction point as reference, and (c) the energy weighted point as reference.

$$\Delta Z = p_{\gamma}^{1^{st}} - p_{reco} \ . \tag{5.7}$$

For both methods, the results for ΔZ, are compared to each other in fig. 5.3 for the three previously described parameter sets. From these results, the FWHM and FWTM values were extracted from the results in an identical manner as described in section 4.3.3. Table 5.2 provides a list of the extracted FWHM and FWTM values.

The parameter set based on the photon source simulation data, results in degraded resolutions, shown in fig. 5.4a, compared to the results presented in

Parameter set from	χ^2 meth.		WA meth.	
	FWHM	FWTM	FWHM	FWTM
Photon Source	2.7	8.2	3.2	8.0
First Gamma	3.8	8.6	4.3	8.6
Energy Weighted	3.5	8.7	3.6	8.1

Table 5.2: FWHM and FWTM values for difference in slice index ΔZ of the ratio based DOI reconstruction for the χ^2 and weighted average methods. Results were obtained for three different parameter sets used during reconstruction.

section 4.3.3. These differences in the results are expected and are attributed to Compton scattering of the gammas inside the scintillator crystal. Namely, the light distribution of Compton scattered gamma rays have multiple photon emission centers. The result is a light distribution, in relation to the first gamma interaction location, which differs from a light distribution caused by a single emission point, i.e. a photon source.

Performing the DOI reconstruction with the parameter sets obtained from the simulations with gamma rays, figs. 5.4b and 5.4c, results in a worse reconstruction resolution compared to the photon source parameter set. In particular, the parameter set obtained relative to the first gamma interaction points, results in the worst resolution of all the parameter sets.

In section 4.3.3, the difference in slice index ΔZ was studied in function of the slice p_{em} from which the scintillation photons were emitted. Here, the same procedure is performed were p_{em} is now replaced with the slice $p^{1^{st}}$ in which the first gamma interaction occurred. The results for the mean and FWHM values of ΔZ for each slice are shown in fig. 5.4.

Regardless of the method and parameter sets used during reconstruction, the first layer (L1) has a similar forward bias (deeper into the crystal) for DOI reconstructing. Also in the second layer (L2), the same backward bias (towards front) for DOI reconstruction is present. Gamma interactions in the crystal occuring beyond the middle of layer 2 (L2) lead to an adequate reconstruction of the slice. This is supported by low absolute values for ΔZ for $p > 9$. In addition for these slices, the FWHM has stabilized in the range 2 mm–3 mm.

Although, from fig. 5.4b, it is clear that when using the first gamma parameter set, the weighted average method has issues. It suffers from a strong backward bias of the DOI reconstruction once the annihilation gammas go beyond the top layer (L1). This can be seen from the nearly linear increase of the mean values of ΔZ for $p > 5$.

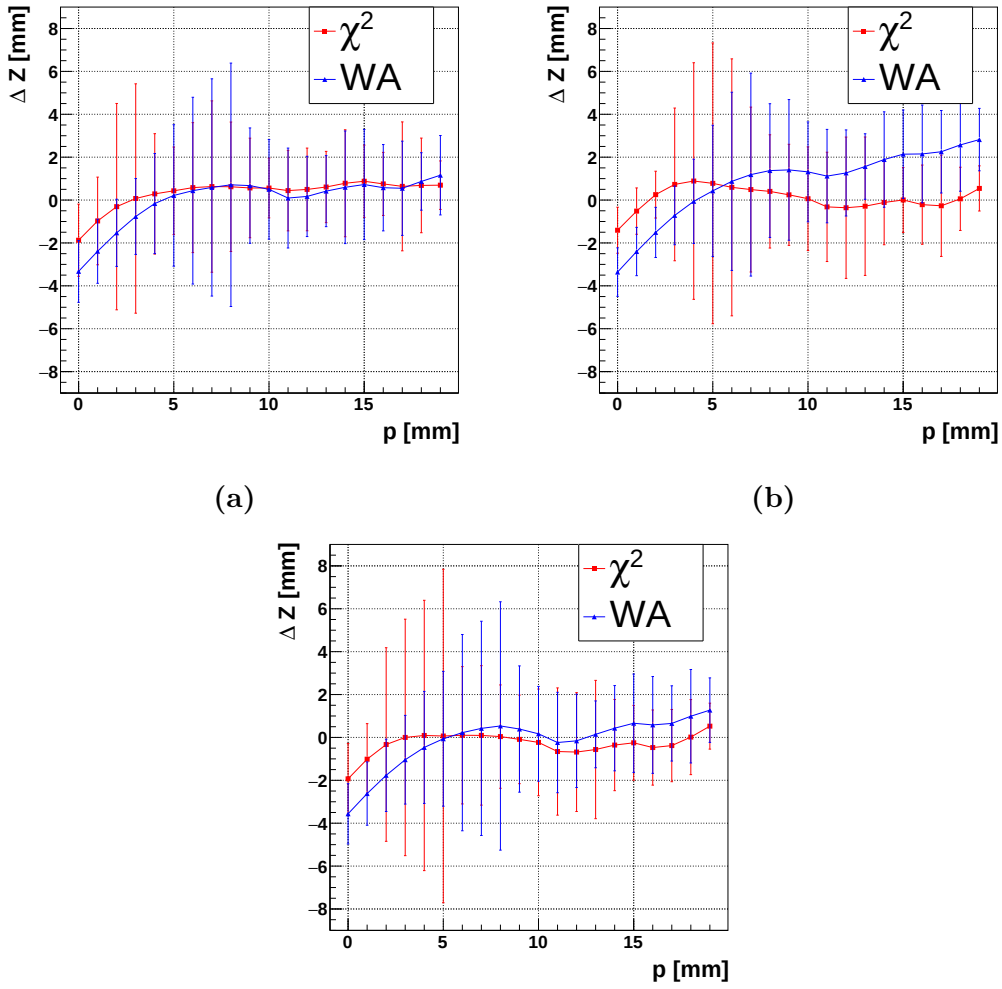

Figure 5.4: Mean and FWHM values for ΔZ as a function of slice p^{1st} for the ratio based reconstruction methods. Results are obtained with three variations in parameter sets which were extracted from: (a) simulation data with a photon source, (b) gamma ray simulation data with the first gamma interaction point as reference, and (c) the energy weighted point as reference.

5.3.2 Cube Reconstruction Efficiency

The extraction of the efficiency for the cube reconstruction is performed identically as described in section 4.4.2 with the emission point, as in section 4.4.2, substituted for the first gamma interaction point. Results for the three possible parameter sets are presented in fig. 5.5.

Comparing the efficiencies between the three parameter sets indicates that the parameter set obtained with the first gamma interaction point, fig. 5.5b,

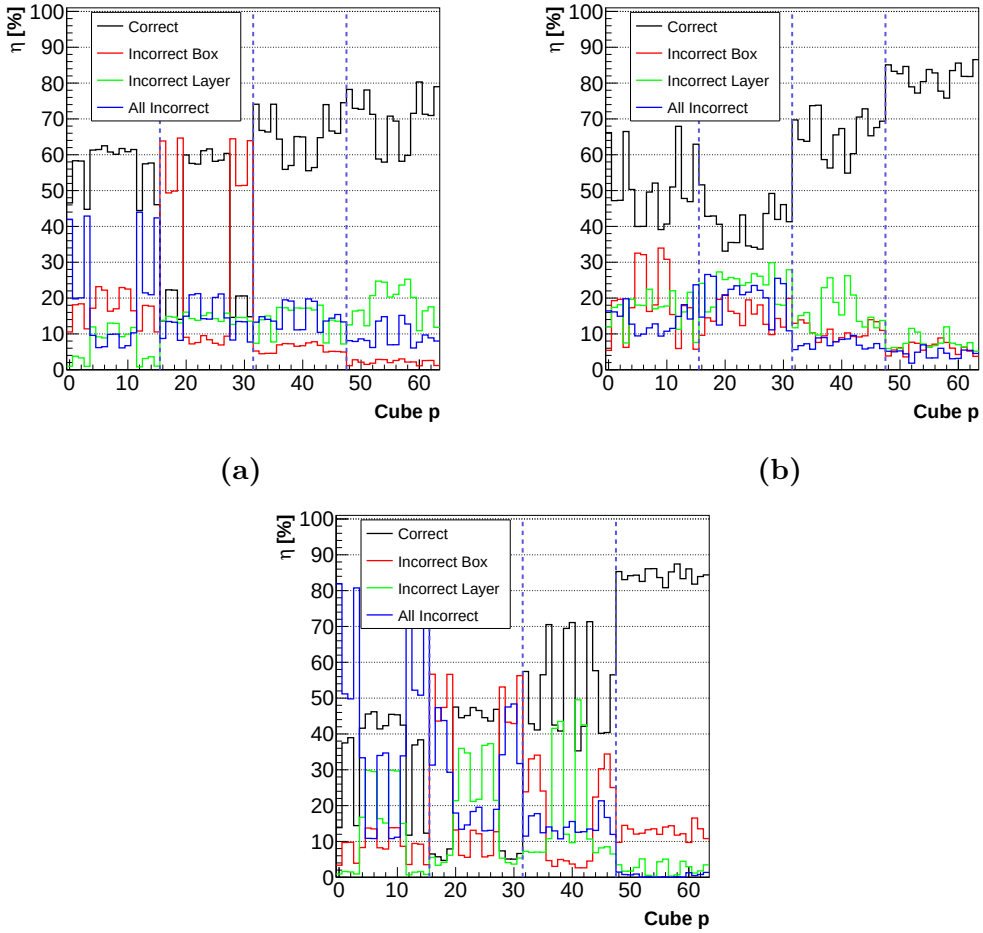

Figure 5.5: Reconstruction efficiencies of the cube reconstruction for parameter sets extracted from: (a) simulation data with a photon source, (b) gamma ray simulation data with the first gamma interaction point as reference, and (c) the energy weighted point as reference.

provides the best overall cube reconstruction efficiency.

The difference between the parameter sets of the photon source and gamma ray simulation data can be understood by comparing the distributions for the channel fractions f_k, defined in eq. (4.10). Figure 5.6 presents the distributions for the channel fractions f_k for a corner cube in layer 2, i.e. the photon source, first gamma interaction or the energy weighted position originated in this cube. This cube was chosen as its reconstruction efficiency suffers greatly for the parameter sets not referenced to the first gamma interaction point, see first cube index in the second layer which has a low reconstruction efficiency in fig. 5.5.

A comparison of the distributions for the channel fractions f_k presented

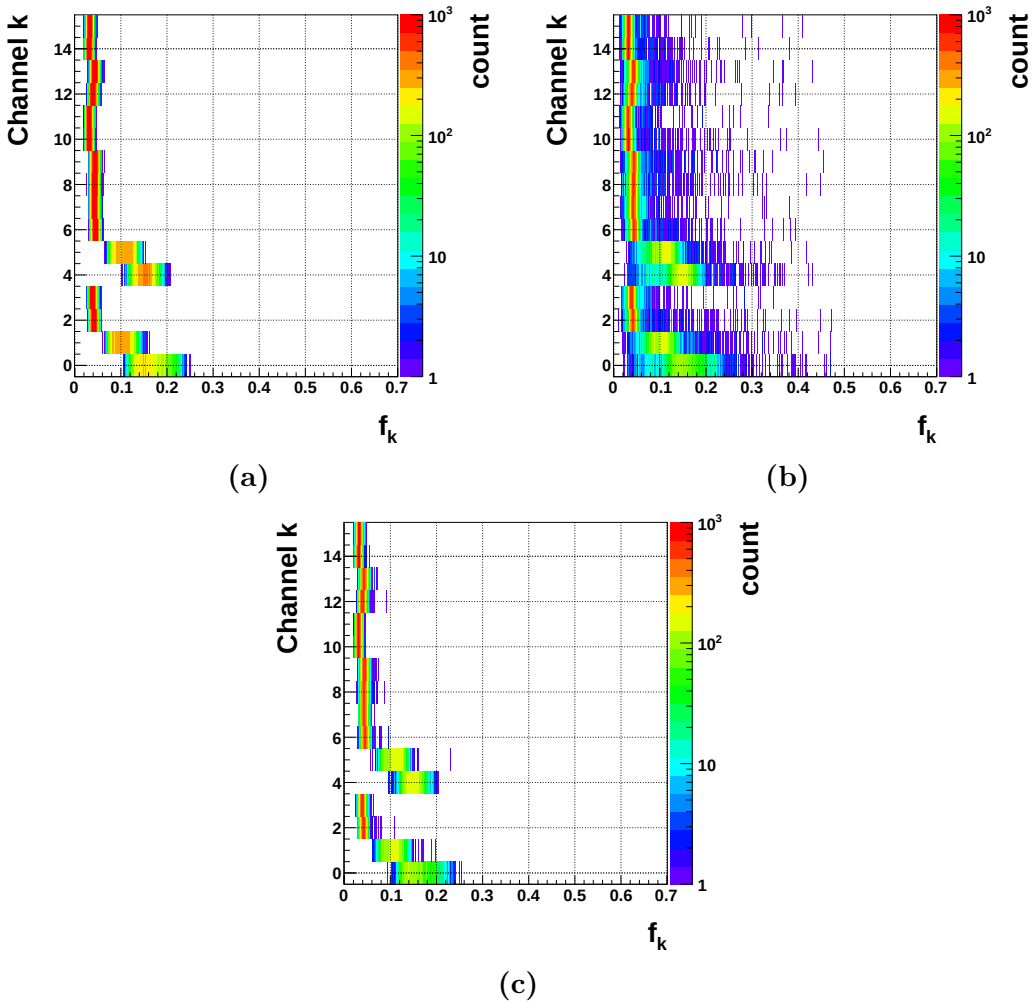

Figure 5.6: Channel fraction distributions f_k for a corner cube in the second layer extracted from: (a) simulation data with a photon source, (b) gamma ray simulation data with the first gamma interaction point as reference, and (c) the energy weighted point as reference.

in fig. 5.6 indicates narrower distributions for the simulation data with the photon source and when the energy weighted position is taken as reference point. The result of these more narrow distributions are smaller values for the RMS (σ_k^j) compared to the distributions with the first gamma interaction as the reference point. In turn this leads to a higher probability that the parameter set for the first gamma interaction has a smaller χ^2, eq. (4.11).

In fig. 5.7 the resulting χ^2 distributions for the different parameter sets are presented. These figures are limited to the χ^2 distributions to the second layer, cube indices 16 to 31.

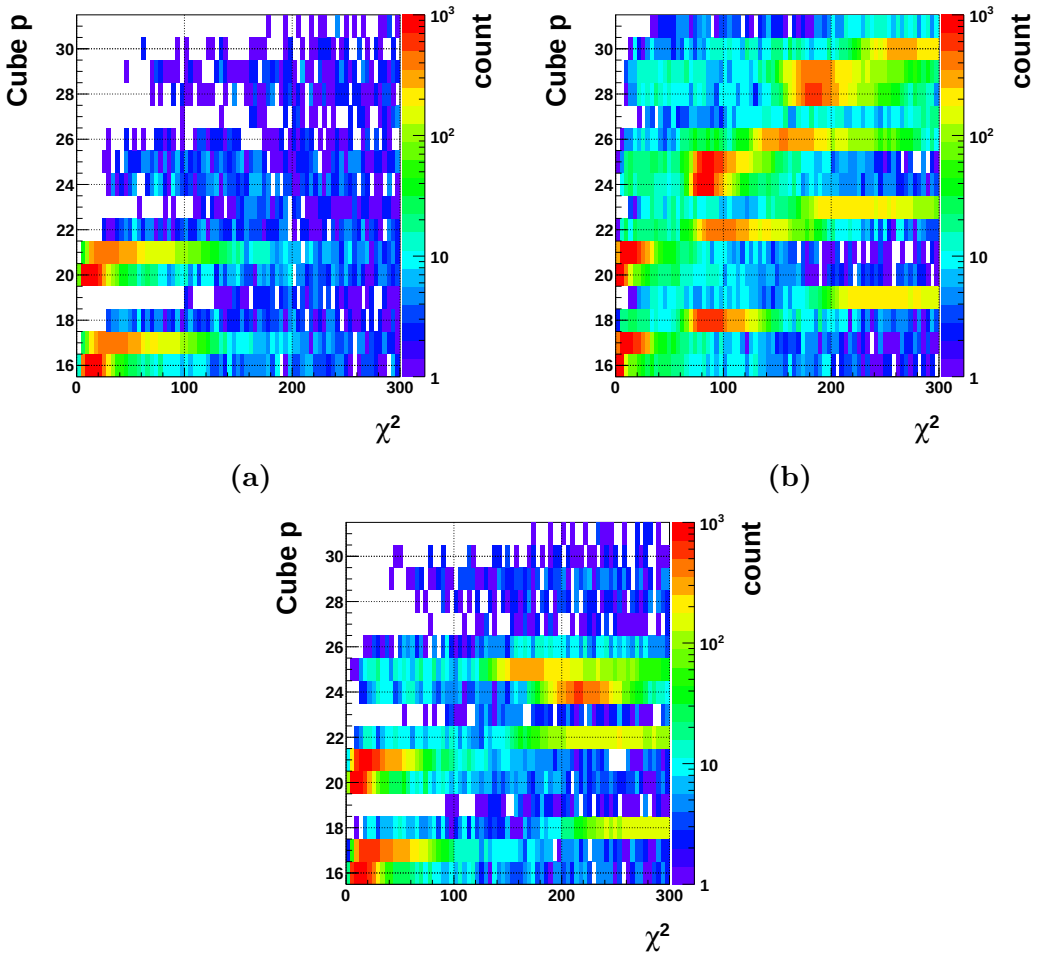

Figure 5.7: Results for the χ^2 distributions of the second layer when the first gamma interaction occurred in the corner cube with cube index 16 for the parameter sets obtained: (a) from the photon source simulation data, (b) with the first gamma interaction point as reference, and (c) the energy weighted point as reference.

5.4 Comparison of Reconstruction Methods

For both ratio based reconstruction methods the (X, Y) position is determined through either the maximum channel or the cube reconstruction methods. The maximum channel method does not rely on a set of parameters for reconstruction like the cube reconstruction method. As such the comparison is mostly limited to a comparison between the various reconstruction parameter sets for the cube reconstruction. However, the results for the maximum channel method are compared to the results presented in fig. 4.15. For both reconstruction methods, the distances ΔX and ΔY are defined similarly as

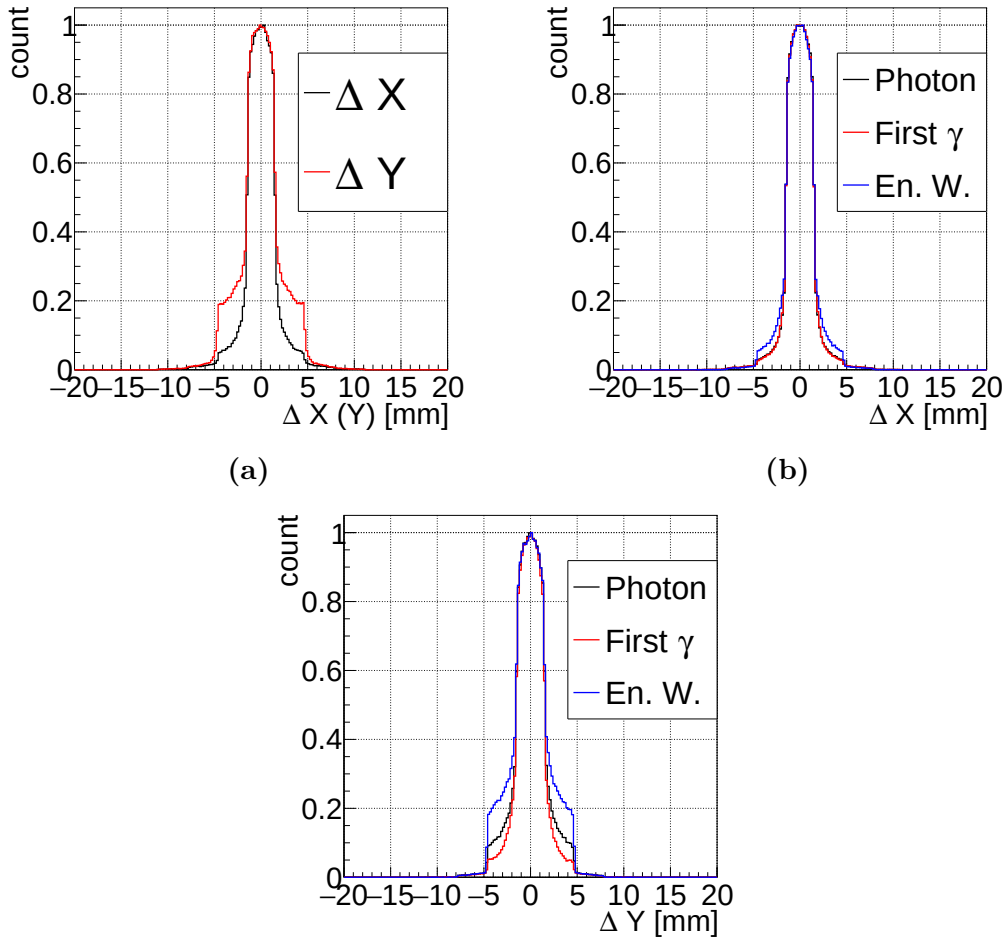

Figure 5.8: Reconstruction resolutions ΔX and ΔY. (a) Maximum channel method. Comparison of the various parameter sets for the cube reconstruction: (b) ΔX, and (c) ΔY.

eq. (4.14) and eq. (4.15) where the coordinates of the emission point are replaced with the coordinates of the first gamma interaction point.

With the simulation of gammas, multiple interactions will be present in a considerable number of events. These multiple interactions have the potential to cause significant changes to the light distribution when compared to a single point of emission. As such the (X, Y) resolutions for the maximum channel method are presented in fig. 5.8a. Comparison with the results for the maximum channel method in fig. 4.15 indicates that multiple gamma interactions have a minimal influence on the performance of the maximum channel method.

The comparison for the cube reconstruction is made for the three different parameters sets for reconstruction as described before, see section 5.3. From

the results presented in fig. 5.8b it is clear that the reconstruction of the X position has a minimal sensitivity to the chosen reconstruction parameter set. While the reconstruction of the Y position has the same FWHM, it does show a dependence on the chosen set of reconstruction parameters for the tails. Comparing the parameter set from the energy weighted position with the parameter set from the first gamma interaction yields nearly a factor of 2 difference at the FWTM.

A comparison of the DOI reconstruction is made for the cube, and the ratio based reconstruction methods. Simultaneously, the comparison is also made for the various reconstruction parameter sets. The distance ΔZ between the first gamma interaction point $Z_\gamma^{1^{st}}$ and the reconstructed DOI position Z_{reco} is defined identically as in eq. (4.13) with Z_{gen} replaced by $Z_\gamma^{1^{st}}$.

From the results in fig. 5.9 it is clear that the ratio based methods have a better resolution compared to the cube reconstruction. This result is similar as for the simulation with a single photon source, see section 4.5. More interesting is the influence of the parameter sets applied to perform the reconstruction. The photon source parameter sets lead to better resolutions for the ratio based reconstructions, 2.3 mm (2.5 mm) for χ^2 (WA resp.), fig. 5.9a, while the parameter sets with the first gamma interaction lead to the worst resolution, 3.5 mm (3.1 mm) for χ^2 (WA resp.). On the other hand, the cube reconstruction obtains the best resolution with the first gamma parameter sets, while the energy weighted parameter sets lead to the worst resolution.

Another feature present in the results for the reconstruction resolutions are the offsets of the peaks in figs. 5.9a to 5.9c. With the photon source parameter sets, there is practically no peak offset present for the ratio based methods, while for the other two parameter sets there is a noticeable offset present for at least one of the two methods. Regardless of the parameter set applied to the reconstruction, the cube reconstruction method always suffers from an offset.

Similarly as in fig. 4.16a, figures with the mean ΔZ as a function of the cube index in which the first gamma interaction occurred are presented in fig. 5.10. It provides details regarding the dependency of the DOI reconstruction offsets on the first gamma interaction location.

The offset towards deeper DOI of the χ^2 method for the energy weighted parameter sets seems to mostly originate from reconstruction of events with their first interaction in the top layer (L1), fig. 5.10c. For the other parameters sets there is no preferred direction of the offset for the χ^2 method.

Regardless of the type of parameters sets used during reconstruction, the weighted average (WA) DOI reconstruction method suffers from a consistent offset of $\approx$2 mm in the top layer (L1) towards deeper DOI values. While the offset for WA reconstruction is minimal for layers 2, 3, and 4 when the photon source and energy weighted position parameter sets are applied, the first gamma parameter sets cause considerable offsets regardless of the location of

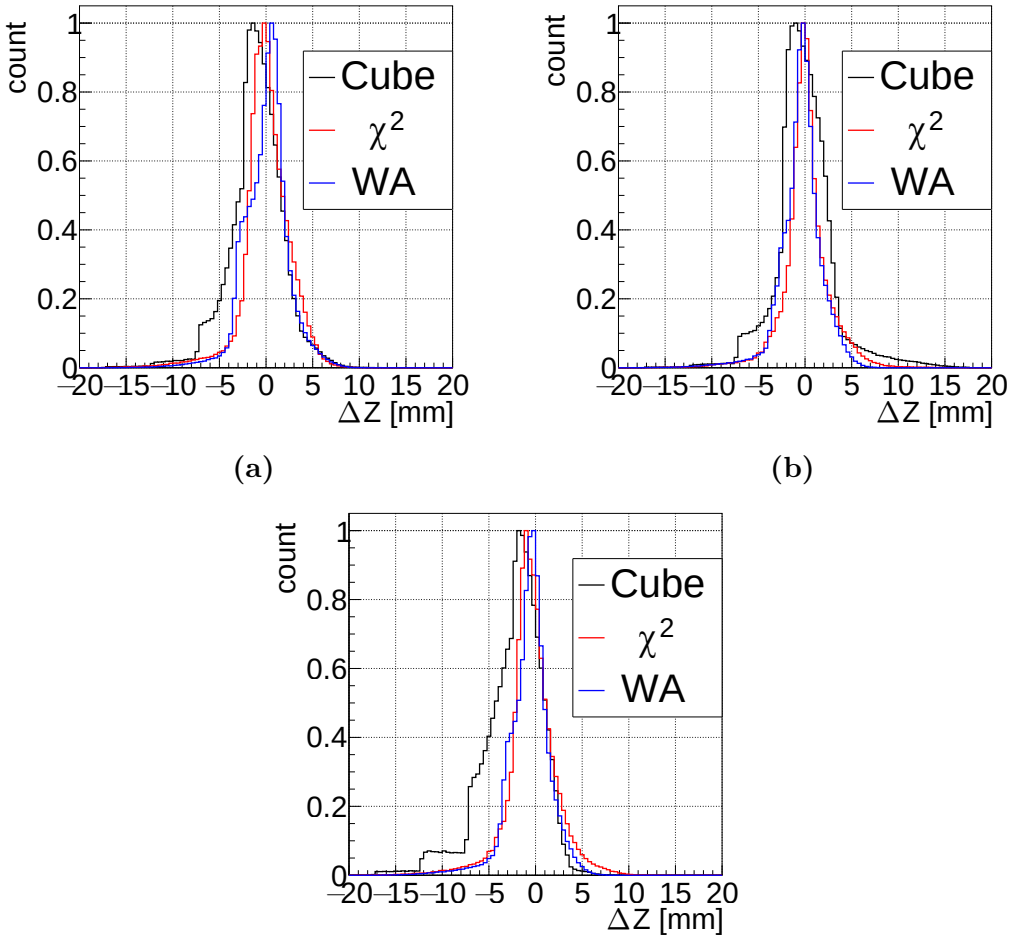

Figure 5.9: Comparison of the DOI reconstruction resolutions for the different parameter sets: (a) photon source, (b) the first gamma interaction point as reference, and (c) the energy weighted point as reference.

the first gamma interaction. In addition, there is also a change in direction of the offset at the interface of layer 1 and 2, where the offset changes from deeper to more shallow reconstructions, relative to the true DOI.

The cube reconstruction method benefits the most from the first gamma parameter sets with a DOI reconstruction resolution of 4.3 mm, see fig. 5.9b. With the energy weigthed parameter sets, the shoulder at the leading edge in fig. 5.9c has grown considerably. This means that a considerable amount of events are reconstructed at a deeper DOI compared to the DOI of the first gamma interaction point.

From the Klein-Nishina formula [42] for the differential cross-section of Compton scattered gammas, it follows that 511 keV gamma rays have a higher probability to scatter under a low angle. Combined with the higher

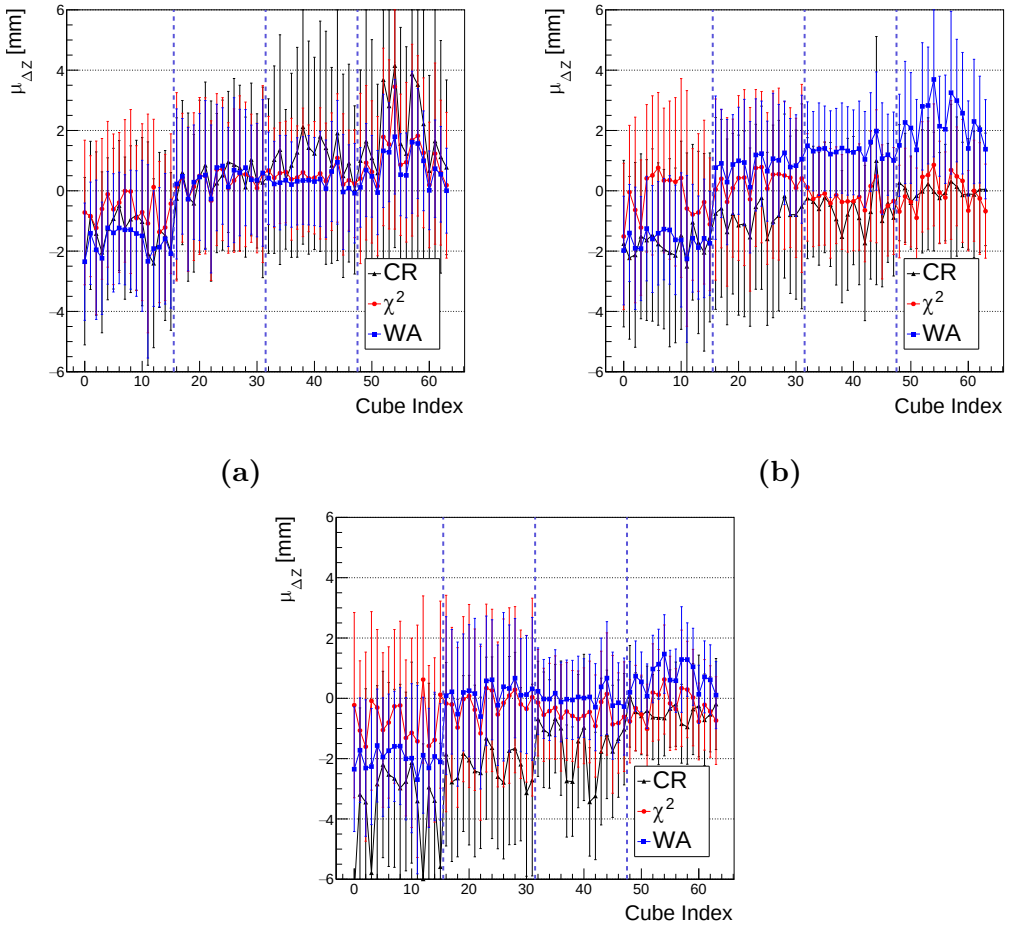

Figure 5.10: Comparison of the DOI reconstruction resolutions for the different parameter sets: (a) photon source, (b) the first gamma interaction point as reference, and (c) the energy weighted point as reference.

probability for Compton scattering v.s. photoelectric effect, it explains why the energy weighted interaction point is more often located at a deeper DOI.

5.5 Tube of Response

The aim of the proposed PET module is to improve the resolution of the LOR reconstruction. The reconstruction resolution of the gamma interaction point leads to an imperfect reconstruction of the LOR. Overall this results in a tube of response (TOR) encasing the LOR which in turn leads to a degradation of the image quality of a PET scan.

In fig. 5.11 a model of a PET scanner is presented to illustrate the TOR.

In addition it illustrates the effects of the location of the annihilation event with respect to the central region of the ring and how it gives rise to the so called parallax error.

This parallax error is the result of the gamma ray passing through scintillator crystals before it interacts. When a gamma ray passes through a crystal (or a segment), it shifts one of the end points of the LOR away from the true LOR. Figure 5.11 only illustrate the parallax error in two dimensions. In reality, PET scanners utilize multiple rings in parallel along the Z axis. Aside the degradation of image quality in the plane of each ring, the parallax error also limits three dimensional reconstruction techniques.

The blue dots in the figure represent annihilation events while the blue (white dashed for the central LOR) lines represent the true LOR. Reconstructed LORs are shown in red and the TOR is indicated with a light gray area. Both the left and right side of the figure are symmetrical in terms of the locations of e^-e^+ annihilation and the interaction points in the scintillation crystals.

From the figure, one can see that annihilation events occurring in the central region of a PET scanner will have their gamma rays enter the scintillation crystal with a momentum direction perpendicular to the entry face. For these types of annihilation events, only the (X, Y) coordinates and their resolutions $(\Delta X, \Delta Y)$ are of importance during LOR reconstruction. In this case the TOR becomes a rectangular volume surrounding the true LOR with dimensions $(\Delta X, \Delta Y, D)$, D being the diameter of the ring.

The left side of the figure, illustrates the increase in size of the TOR for an array type crystal. On the right side a TOR is presented for the segmented crystal type utilizing the cube reconstruction. The light green areas indicate the array element or the cube in which gamma interacted.

As can be seen in the figure, when the array element or the cube was reconstructed correctly, the TOR will be substantially smaller for the cube reconstruction compared to the array type crystal. Simultaneously the reconstructed LOR (red) is relatively close to the true LOR (blue) in the case of the cube reconstruction. The array type crystal, on the other hand, suffers from a clear divergence between the reconstructed (red) and the true (blue) LOR.

The central part of the figure illustrates the TOR which both types of crystal would obtain for an annihilation event occurring at the central axis of the PET ring. Considering that both types of crystals have similar resolutions $(\Delta X, \Delta Y)$ in the plane of the detector, both their TOR would be similar as well. The TOR is narrower than for the off-axis annihilation events due to their resolutions in the plane of the detector being smaller compared to their resolution along the crystal (DOI).

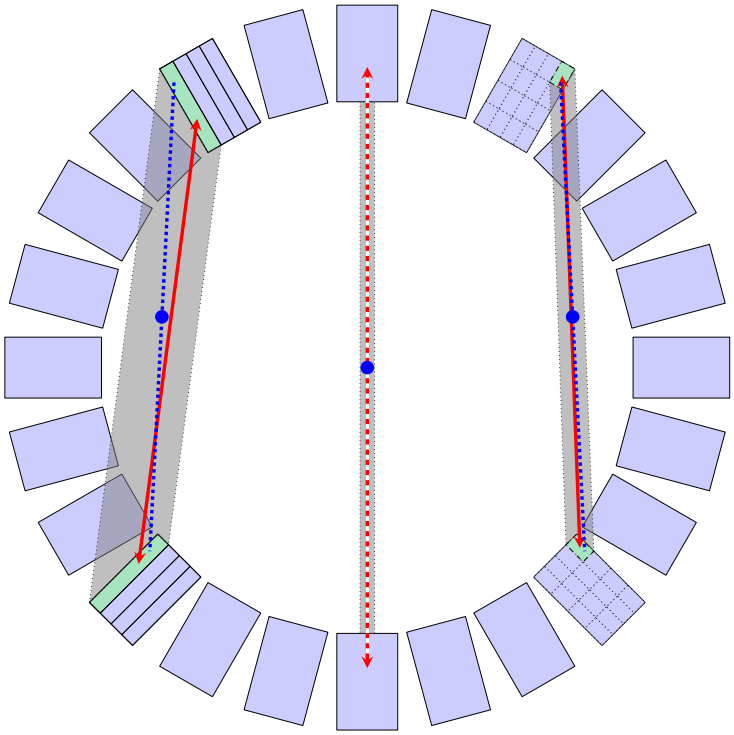

Figure 5.11: A 2D sketch of a pet geometry illustrating the difference in TOR for two different types of segmentations of the scintillator crystal for annihilation events at various locations in a model of a PET scanner.

5.5.1 Extraction of TOR Resolution

To extract the resolution for the TOR it is necessary to obtain the distance between the true LOR and the reconstructed point. As an aid for the method of extraction, a sketch is presented in fig. 5.12. In this figure $\vec{s}$ represents the momentum direction of the primary gamma ray and $\vec{x}_1$ the point of origin of the primary gamma ray. The first gamma interaction point is represented by $\vec{x}_2$ and the reconstructed point by $\vec{x}_0$. The green box represents the volume created by the resolutions $(\Delta X, \Delta Y, \Delta Z)$ of the reconstruction.

From the vectors $\vec{x}_0$, $\vec{x}_1$, and $\vec{x}_2$ it is possible to calculate the vector $\vec{d}$ which is the vector perpendicular to the LOR and going through the reconstructed point. The vectors $\vec{s}$ and $\vec{v}$ are defined as follows

$$\vec{s} = \frac{\vec{x}_2 - \vec{x}_1}{\|\vec{x}_2 - \vec{x}_1\|} \ , \tag{5.8}$$

$$\vec{v} = \vec{x}_0 - \vec{x}_1 \ . \tag{5.9}$$

Then the intersection point of $\vec{d}$ with the LOR is given by

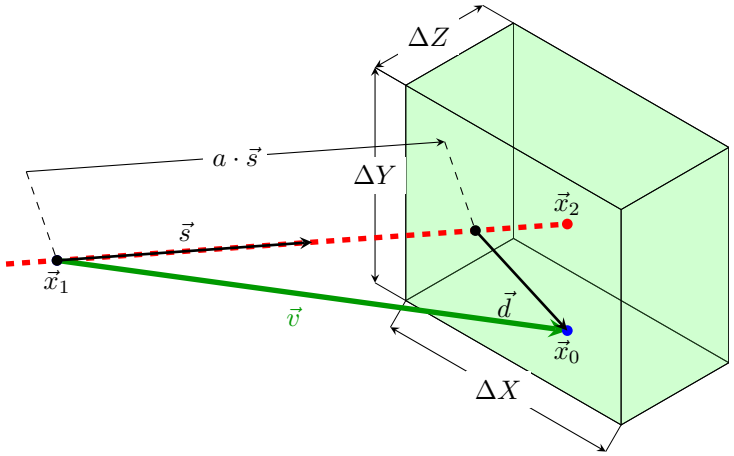

Figure 5.12: Sketch for the calculation of the resolutions $(\Delta X_{\text{TOR}}, \Delta Y_{\text{TOR}})$ for the TOR.

$$a \cdot \vec{s} = (\vec{s} \cdot \vec{v}) \cdot \vec{s} \,, \tag{5.10}$$

with a being a scaling constant. The vector $\vec{d}$ is then obtained with

$$\vec{d} = a \cdot \vec{s} - \vec{v} \,. \tag{5.11}$$

In the simulations with the non-perpendicular gamma rays, their momentum directions were rotated around the X-axis such that their directions only changed along the Y- and Z-axis. This allows us to rotate the vector $\vec{d}$ back over the X-axis to obtain the resolution $(\Delta X_{\text{TOR}}, \Delta Y_{\text{TOR}})$ for the TOR. Considering that for the TOR, the main parameters of interest are the resolutions ΔX_{TOR} and ΔY_{TOR}, thus the resolutions for the TOR are obtained with

$$\Delta X_{\text{TOR}} = d_X \,, \tag{5.12}$$
$$\Delta Y_{\text{TOR}} = d_Y \cdot \cos(\theta) + d_Z \cdot \sin(\theta) \,, \tag{5.13}$$

with d_X (d_Y and d_Z) the X (Y and Z resp.) component of vector $\vec{d}$ and θ being the angle between the Y-axis and the momentum direction of the primary gamma ray.

5.5.2 TOR Resolution

A comparison is made for the TOR resolution between the array and segmented types of crystals. For both types of crystals, simulations were done

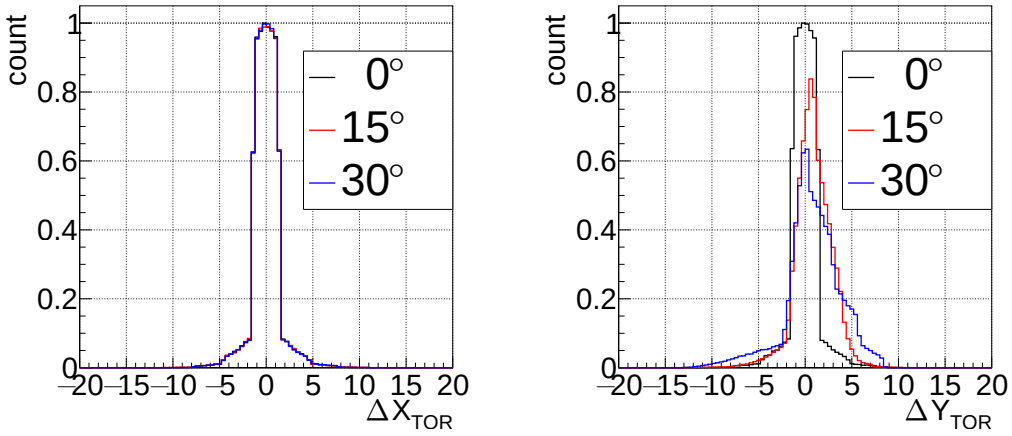

(a) **(b)**

Figure 5.13: Comparison of the TOR reconstruction resolutions for the array type scintillator crystal, i.e. maximum channel reconstruction, for the different angles: (a) ΔX_{TOR}, (b) ΔY_{TOR}.

with gamma rays having an initial momentum direction under an angle with respect to the normal of the crystal entry face. The angle was changed in the YZ plane over the range 0°–30° in steps of 7.5°. Under these conditions, the resolution for the X coordinate remains similar to the case with perpendicular gammas. For the array type crystal, fig. 5.13a shows that indeed there is no change for the resolution of the ΔX_{TOR} coordinate for the gammas with different angles.

The resolution for the ΔY_{TOR} coordinate on the other hand, shows a degradation when the angle between the normal of the entry surface and the gamma momentum directions increases, see fig. 5.13b. Not only does the FWHM increase from 3.0 mm to 4.3 mm, the increase of the FWTM is even more severe, from 3.6 mm to 9.3 mm. The data presented in fig. 5.13b were normalized to their integrals. Afterwards, the data was rescaled to the maximum of the data for the perpendicular gamma rays (0°). It accentuates the increase in the number of reconstructions at further distances from the LOR with the angle.

Results for the FWHM of ΔY_{TOR} of the segmented crystal are presented in fig. 5.15. Overall it is clear that the reconstruction resolution for the segmented crystal has a greater potential to keep its performance over a large range of angles as opposed to the array type crystal.

In addition, a comparison is made between the various parameter sets for the DOI reconstruction. Comparing the results from figs. 5.15a to 5.15c indicates that for the perpendicular angle, that there is a minimal difference in reconstruction resolution between the different parameter sets. However, from fig. 5.15c it follows that the parameter sets for the energy weighted

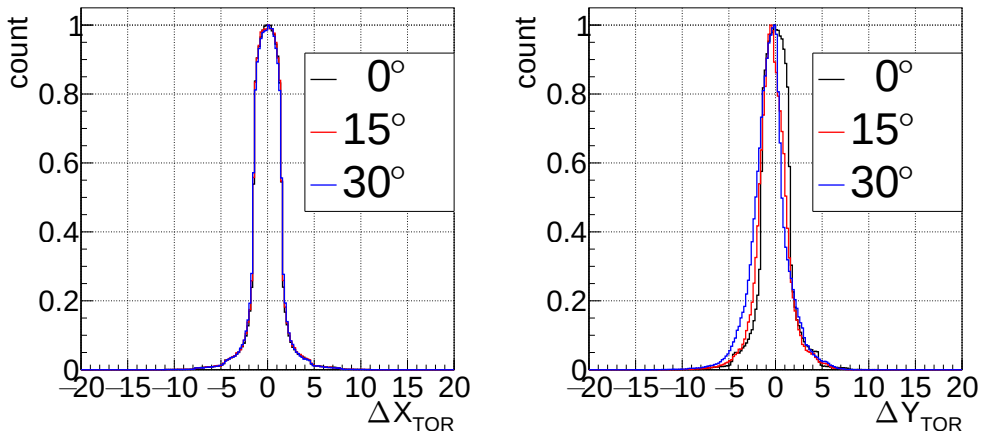

(a) **(b)**

Figure 5.14: Comparison of the TOR reconstruction resolutions utilising the cube method for the segmented type scintillator crystal for the different angles: (a) ΔX_{TOR}, (b) ΔY_{TOR}.

position suffers from a minor degradation towards increasing angle. This degradation is present for all the different DOI reconstruction methods. Thus the energy weighted parameter sets are least suited for reconstruction of the LOR.

Regardless of the parameter sets used, the cube reconstruction achieves the best resolution over the studied range of angles. The resolution for the cube reconstruction becomes better at larger angles. The χ^2 and the weighted average reconstruction methods, on the other hand, suffer from a small degradation in the resolution at the largest angles.

The cube reconstruction achieves the best resolution for both the photon source and first gamma parameter sets. Comparing fig. 5.15a with fig. 5.15b shows that the parameters sets obtained with the photon source have a minor advantage over the first gamma parameter sets. As a consequence it is possible to generate parameter sets with a photon source leading to cleaner channel fraction f_k distributions, see fig. 5.6a.

The fact that the photon source parameter sets provide a better reconstruction resolution compared to the first gamma parameter sets, indicates a possibility to use generated parameter sets for reconstruction of real PET data.

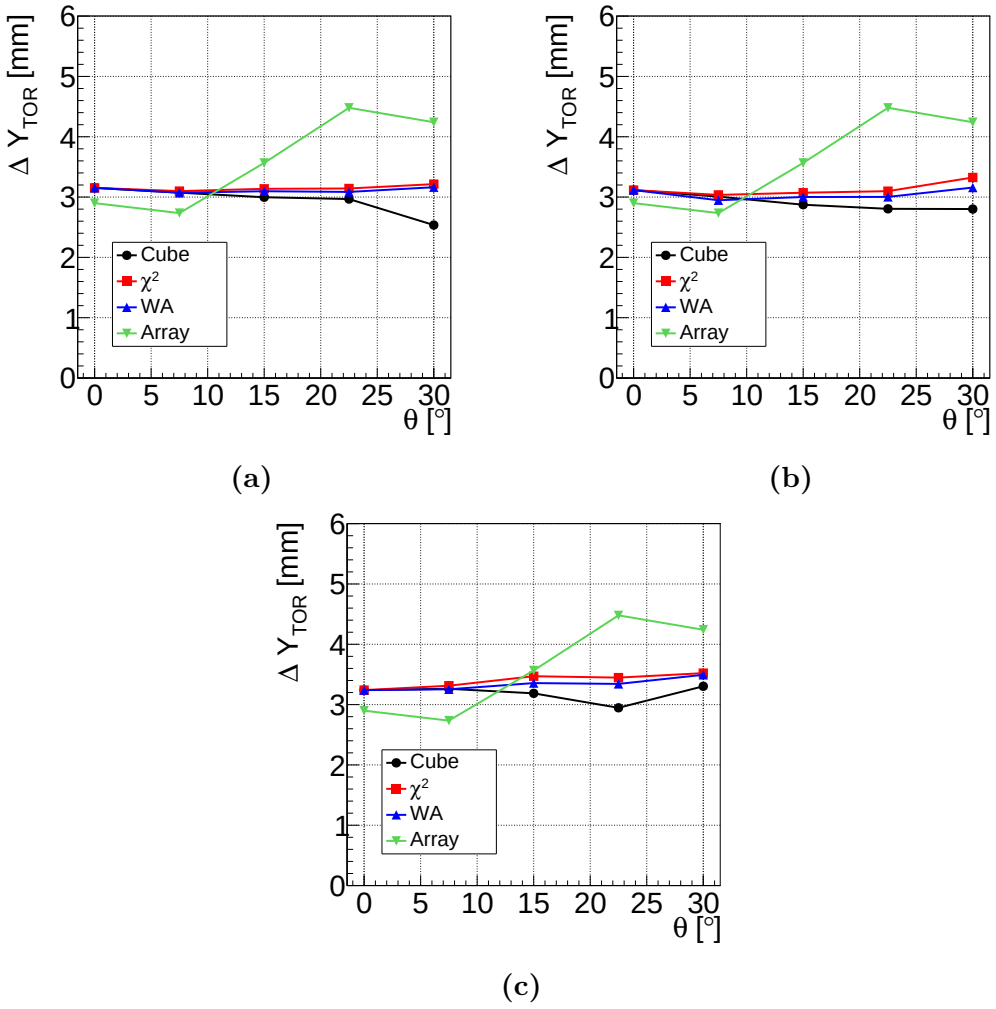

Figure 5.15: FWHM resolutions ΔY_{TOR} as a function of angle between the entry surface normal and the initial gamma momentum direction: (a) photon source parameter sets, (b) the first gamma interaction point as reference, and (c) the energy weighted point as reference.

Chapter 6

Experimental Setup

The setup for verification of the DOI encoding of the segmented crystal array consists of a ^{22}Na β^+ placed in between two gamma detectors, as shown in fig. 6.1. Each gamma detector consists of a LYSO scintillation crystal coupled to a SiPM as photodetector.

One of the gamma detectors consists of a small LYSO scintillator optically coupled to a single SiPM. This gamma detector acted as the trigger for PET events originating from the ^{22}Na β^+ source. Detection of both annihilation gammas on both detectors ensures that mostly events originating from an annihilation are considered. Its small size and longer distance from the source ensured a well collimated beam of gamma rays.

The second gamma detector is a prototype PET module which consists of a segmented crystal array coupled to an array of SiPMs, and is the device under test (DUT). To study the performance of this prototype module, the ^{22}Na β^+ source is placed between the two detectors to provide two back to back 511 keV gamma rays.

The protoype module is mounted onto a 2D translation stage to scan the gamma ray beam over the surface of the module. It is possible to mount the module on the translational stage in two different orientations to enable scans over different surfaces of the module. Both mounting directions are required

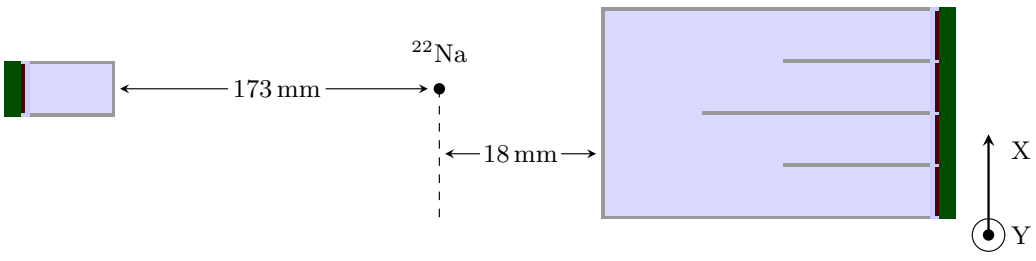

Figure 6.1: Illustration of the setup in the XY scan orientation indicating the distances between the source and the trigger detector. The X and Y directions of the module movement are indicated on the right hand side.

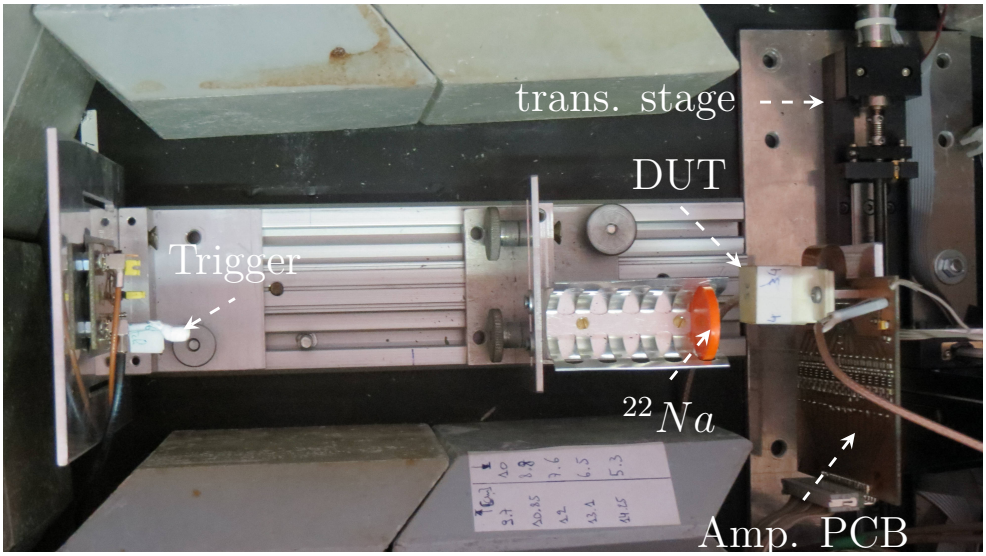

Figure 6.2: Back-to-back gamma setup used for the measurements. The entire setup is surrounded by lead shielding.

to obtain the performance of the prototype module in the XY and the YZ (DOI) planes.

6.1 Gamma Detectors

To prevent ambient light from disturbing the measurements, the entire setup was placed in a light tight box. This box was then covered with an additional layer of black cloth to ensure that no outside light was able to enter the box. The inside of the light tight box containing the entire measurement setup is shown in fig. 6.2.

6.1.1 Trigger Gamma Detector

The function of the trigger gamma detector is to start the digital acquisition when it detects a gamma. The digital acquisition is started when the signal measured on the trigger is sufficiently large. At this point a gate signal is generated to instruct the digital acquisition to record the signals originating from the trigger and all the channels of the prototype PET module. This gate signal is held long enough for the acquisition to measure a full scintillation pulse of the PET module.

The trigger gamma detector consists of a small piece of LYSO crystal produced by Saint-Gobain Ceramics & Plastics, Inc. with dimensions $3 \times 3 \times 5\,\mathrm{mm}^3$ coupled to a SiPM. This scintillator crystal does not have any

segmentations.

The SiPM for the trigger was a $3 \times 3\,\mathrm{mm}^2$ device of the surface mount type with model number S10931-50P. It has a cell pitch of 50 µm providing a total of 3600 cells. With the simulations, it was shown that on average ≈2500 photons were detected for a 511 keV gamma ray. Combined with the non-linearity of a SiPM device, see section 2.2.1, it means that the scintillation pulses fall in the non-linear range of the trigger detector. However, this does not cause issues considering that only events within the photopeak (PPK) are of interest, e.g. gammas with an energy close to 511 keV.

A constant bias of 72 V was applied to the trigger SiPM during all the measurements. This bias was slightly above the bias recommended by the producer, 71.8 V.

The trigger detector was placed in a static position and with its central axis in the horizontal direction and aligned to the ^{22}Na source. The distance between the source and the trigger detector was 173 mm.

6.1.2 Prototype PET Module

The prototype PET module consists of a LYSO scintillator crystal which was coupled to the SiPM array with a Silicon based coupling grease, REXON RX-688. The coupling grease aids in preventing the formation of a thin layer of air between the crystal and the SiPM array. This reduces the amount of total internal reflection of scintillation photons at the coupling interface between the scintillator and the photodetector.

A holder for the entire module was produced out of a white plastic (PA2200) with laser sintering. The function of the holder was to keep sufficient pressure applied to keep an optimal optical coupling between the crystal and the SiPM array. The module was directly mounted to translational stages with the holder.

In fig. 6.3 a picture is shown of the SiPM array and the segmented crystal scintillator. A €0.10 coin is added as a size comparison.

Silicon Photomultiplier

A S11830-3344MT(X), also produced by HPK, was selected for the SiPM array as it provided a 4×4 array of SiPMs in a monolithic package. It was chosen for its good performance in terms of gain and low dark count. In addition, it has the benefit that all SiPMs channels in the array have an operating bias in a narrow range. The mean recommended operating bias of the array is 72.29 V with an RMS spread of 0.05 V, see appendix C. The SiPM array was operated at this mean recommented bias.

A LM73 temperature sensor from Texas Instruments, [43] is directly mounted onto the SiPM array. This temperature sensor and its readout

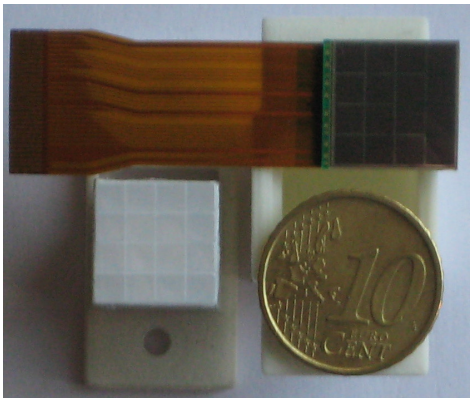

Figure 6.3: Picture of the components which make up the PET module. The SiPM array is pictured on top and the left bottom shows the scintillator crystal array.

LYSO Material Properties	
Density [g/cm^3]	7.2
Radiation Length [cm]	1.1
Decay Constant [ns]	40–44
Light Yield [photons/MeV]	32000
Peak Emission [nm]	428
Refractive Index	1.82

Table 6.1: LYSO scintillator material properties as specified by Sinoceramics (USA), LLC.

circuit are part of the monolithic package as provided by HPK. The temperature sensor was configured to provide a temperature readout with a step of 0.125 °C.

Detailed data for the SiPM array regarding the channel layout, recommended bias for each channel, signal extraction, and communication with the temperature sensor can be found in appendix C.

Each SiPM in the array has a single cell pitch of 50 µm, again providing 3600 cells in a single SiPM. The 16 SiPMs are arranged in a 4×4 matrix with a pitch of 3.2 mm between the SiPMs. Each SiPM has an active area of $3 \times 3\,\text{mm}^2$. The entire SiPM array is combined into a monolithic package with a 0.3 mm layer of protective glass epoxy and mounted onto a PCB with a thickness of 1 mm.

Scintillation Crystal

The specially segmented crystal array was produced by Sinoceramics (USA), LLC. according to the dimensions specified in section 2.3. To obtain the layered structure it was produced from a monolithic block of the LYSO scintillating crystal by making several perpendicular cuts at varying depths. Eventually this resulted in 4 layers with varying degrees of segmentation without the need for optical glue to bond the layers together. LYSO was chosen as scintillating material for its relatively high light yield at 511 keV to ensure a good spatial and energy resolution and its potential for good timing.

Properties of the LYSO scintillator material, as specified by Sinoceramics (USA), LLC., are presented in table 6.1. The cuts in between the segmentations were filled with $MgSO_4$ as a reflective material.

Translational Stages

A pair of translational stages, MM-4M-EX from National Aperture, were mounted to each other in an orthogonal configuration such that scans can be performed in a 2D plane. The stages with the mounted prototype module were placed, with respect to the source and trigger, such that the beam of gamma rays enter the scintillator of the PET module at perpendicular angles.

The stages provide a position resolution of 0.3595 µm with a repeatability of ±0.5 µm. A pair of MVP® 2001 Series controllers from MicroMo Electronics provided the automated steering of the stages during the measurements.

6.2 Source

A ^{22}Na β^+ high resolution marker 55-0-0490NMA, model MMS06-022-25u, was used as a source. The source was produced by Eckert & Ziegler [44]. It is a β^+ emitter, meaning that a positron is ejected out of nucleus. Due to the relatively low kinetic energy of the positron it loses its kinetic energy in a rather short distance. After all of its kinetic energy is lost, it undergoes an annihilation with an electron and two back-to-back gamma rays are emitted with each having an energy of 511 keV. Besides the emission of positrons, the ^{22}Na source also emits gamma rays at an energy of 1275 keV. Two mechanisms exist for the decay of a ^{22}Na isotope, β^+ and electron capture.

The β^+ is the most prominent decay mechanism and it consists of two branches,

$$\begin{aligned} {}^{22}Na &\rightarrow {}^{22}Ne^*_{1275\,\mathrm{keV}} + e^+ + \nu \ (90.3\%) \\ {}^{22}Na &\rightarrow {}^{22}Ne_{ground} + e^+ + \nu \ (0.06\%) \end{aligned}$$

with $^{22}Ne^*_{1275\,\mathrm{keV}}$ ($^{22}Ne_{ground}$) being an excited state (ground state resp.) of the ^{22}Ne isotope.

Electron capture for ^{22}Na consists of a single branch which always ends in the excited state of ^{22}Ne,

$$^{22}Na + e^- \rightarrow {}^{22}Ne^*_{1275\,\mathrm{keV}} + \nu \ (9.64\%)$$

From both decay mechanisms it is clear that nearly all decays, in total 99.94 %, of ^{22}Na is followed by the emission of a single 1275 keV gamma ray. These 1275 keV gamma rays are emitted in random directions. The coincidence mode of the measurements, through the use of a trigger detector, greatly eliminates the contribution of these gamma rays to the background.

The active region of the source has a spherical shape with a diameter of 0.25 ± 0.05 mm that is encased in a clear acrylic disc. The acrylic disc has a thickness of 6.35 mm and a diameter of 25.4 mm. The activity of the source was (925 ± 139) kBq, calibrated at 15/01/2009. The small size of the active

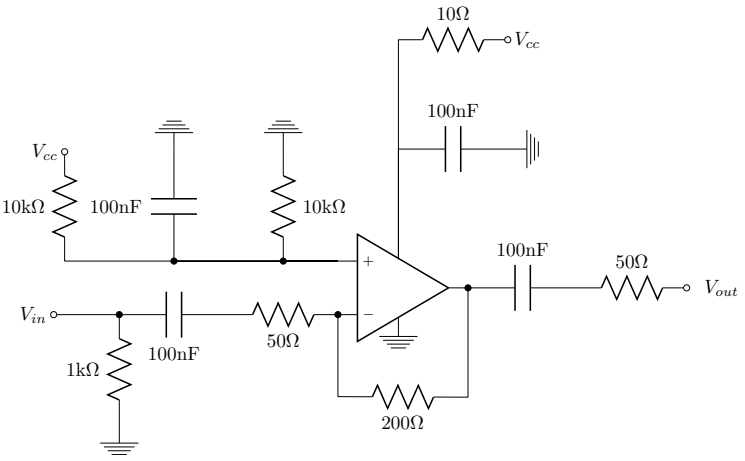

Figure 6.4: Single channel amplifier electronic schematic used to readout the individual SiPM channels.

region of the source provides a well defined point of gamma emission. Due to the activity of the source, a lead shielding was placed surrounding the entire setup.

The trigger was placed at a distance of 173 mm from the source and the prototype PET module at a distance of 18 mm. These distances between source, trigger, and PET module, combined with the dimensions of the trigger scintillation crystal results in a gamma ray beam spot size of ≈0.7 mm on the PET module. This estimate does not take into account shallow angle Compton scattered gamma rays in the acrylic disk or along the path to both detectors.

6.3 Electronic Readout

A printed circuit board (PCB) with amplifiers was designed to connect the 16 channels of the SiPM array to the readout electronics. With this PCB each channel could be read out separately to perform charge measurements for each channel which is necessary for the depth of interaction encoding. The electronic schematic for a single channel amplifier is shown in fig. 6.4.

The amplifier used was an EL8102 [45] which is a single rail-to-rail amplifier with a −3 dB bandwidth of 500 MHz, and a slew rate of 600 V/µs. It requires a very low 5.6 mA supply current.

The amplifier PCB also doubled as the mounting board for the PET module as illustrated on the left hand side in fig. 6.5. This PCB is then mounted onto the mounting point of the translational stages. All 16 channels are connected through a 17 channel flat cable, 16 signals and 1 ground, to a CAEN V792 QDC VME module [46] for data acquisition.

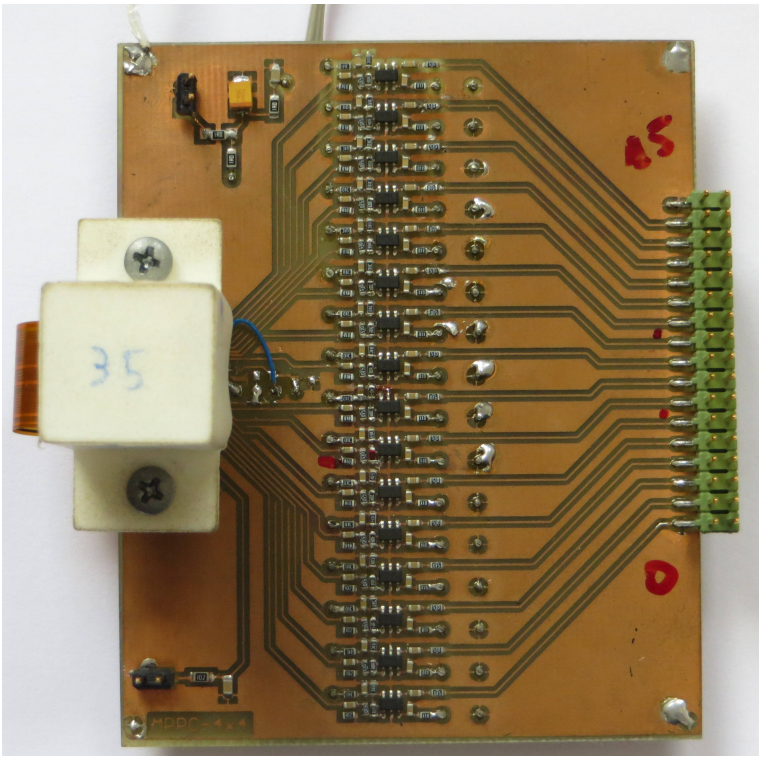

Figure 6.5: Photo of the amplifier PCB for the readout of the PET module signals. The PET module, white block on the left, is mounted in front of the PCB.

The V792 QDC VME module is a 1-unit wide VME 6U module providing 32 Charge-to-Digital Conversion channels with current integrating inputs with a 50 Ω input impedance. Each channel converts the input charge into a voltage level by a QAC (Charge to Amplitude conversion) and provides an input range of 0 pC to 400 pC. The integral non-linearity of the module is ±0.1 % of the full scale range (FSR).

The trigger SiPM was connected to an amplifier before splitting the signal. After splitting, one of the signals was connected to a Phillips Scientific 715 discriminator to generate a gate signal for the ADC modules. This discriminator output was connected to a CAEN N93B timing unit. The gate was set to 400 ns and was sent to both ADC VME modules using a daisy chain. A schematic of the entire chain of electronics is shown in fig. 6.6.

Both the V792 and V965 VME modules require the signals to arrive 15 ns after the gate leading edge. Due to this requirement and the delay of the signals from the prototype PET module, arising from the cable length, the signal of the trigger SiPM was delayed for 64 ns with respect to the leading edge of the gate.

Communication with the LM73 temperature sensor on the back of the

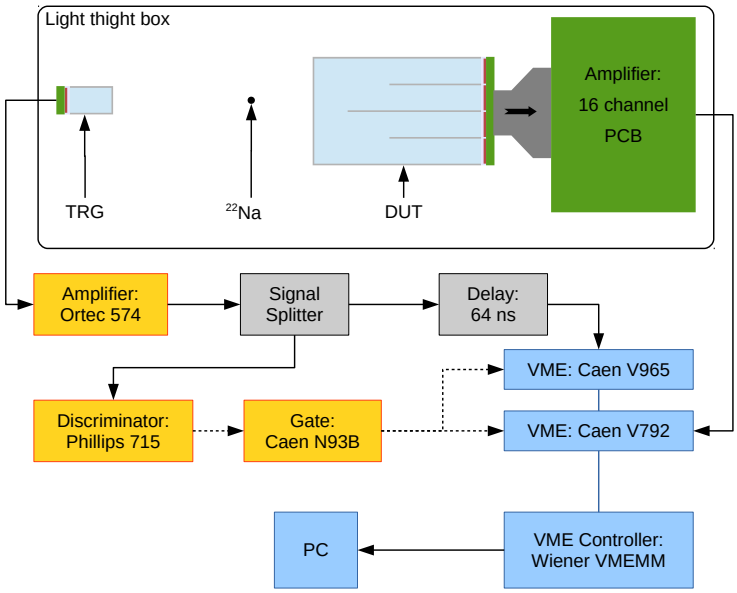

Figure 6.6: Schematic of the readout electronics chain. The cable between the prototype PET module and the readout electronics required an additional delay element for the trigger signal.

PET module was done through the use of a SUB-20 multi interface USB adapter (SUB-20), [47]. The SUB-20 adapter provides an easy programming interface to readout I^2C devices, i.e. LM73, over USB. This provided the temperature readout during the data acquisition.

6.4 Measurements

To study the performance of the DOI segmented crystal array various scans were done. Two different mounting positions were possible for the prototype PET module. The primary mounting position was used to determine the performance of the 2D position reconstruction in the plane of the SiPM array. These scans are referred to as the XY scans. The secondary mounting position was used to study the performance of the DOI encoding and are referred to as the DOI scans. For each of the scan types the scanned area was slightly larger than the area of the module to ensure a complete scan over the module surface.

The bias for the SiPM array was provided with an MPOD high voltage power supply EHS 8005p from W-IE-NE-R and ISEG [48, 49]. Simulation for instability of the power supply was tested by varying the applied bias to the PET module in the range 72.35 V to 72.5 V in steps of 50 mV. These steps are ≈5 times higher than the specified ripple, <10 mV, of the power supply.

From these measurements, discussed at a later stage, it can be concluded that these bias fluctuations do not have an influence to the performance of the module.

6.4.1 XY scans

The XY scan orientation, see fig. 6.1, enables to perform a scan over the entry face of the scintillation crystal and thus in the plane of the SiPM array. The purpose of this scan orientation was to verify the 2D position determination in the plane of the detector.

The module orientation was taken to have the front surface of the PET module perpendicular to the line of response between the trigger, source and module. During the measurement, the module was moved transversely inside the beam of gammas originating from the e^+e^- annihilations inside the ^{22}Na source.

Between two measurement points, the module was moved by 0.6 mm, corresponding to 1669 steps of the translational stage. Every movement was limited to a single axis at a time, where for every step along the X axis, the module was first moved over the full range of the Y axis. This results in line scans along the Y axis for each step along the X axis. At each measurement point, 5000 events were recorded while the temperature was recorded every 15 s.

6.4.2 DOI scans

In the second scan orientation, see fig. 6.7, a scan is performed in the YZ plane where the gamma ray beam was scanned over one of the side surfaces of the segmented scintillation crystal. This YZ scan orientation enables to study the DOI encoding of the segmented crystal array. For these DOI scans, the module orientation was taken such that the gamma beam is perpendicular to one of the sides of the PET module. The side chosen for the DOI measurements corresponds to the direction perpendicular to the layer 3 crystal segmentation, see fig. 2.4c.

The DOI scans were performed in a similar manner as for the XY scans. However, now the X positions correspond to Z positions along the length of the crystal. Effectively the DOI scans are a series of line scans along the Y axis for each Z positions along the crystal. Distance between each measurement point are identical to those used during the XY scans. At each point 10 000 events were recorded. The temperature was again recorded every 15 s.

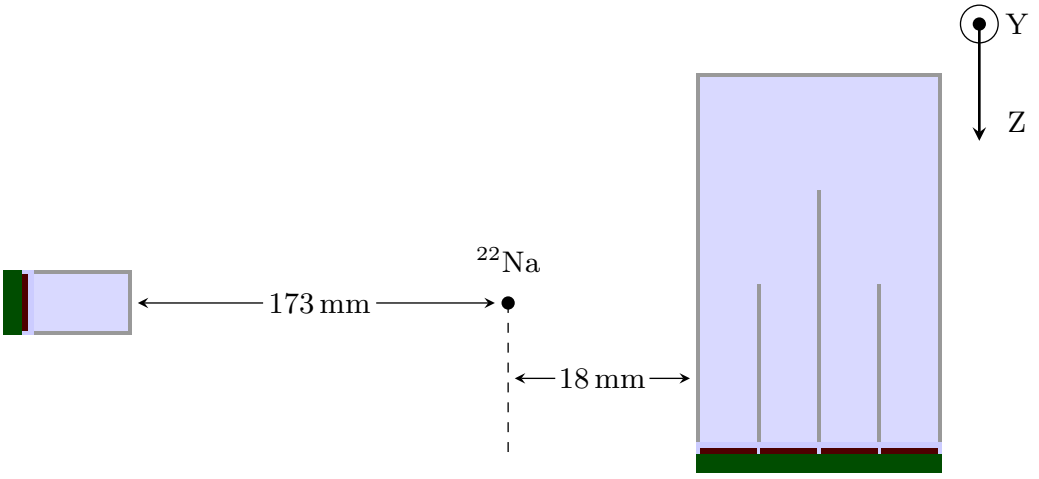

Figure 6.7: Setup in the DOI scan orientation indicating the distances between the source and the trigger. The Y and Z directions of the module movement are indicated on the top right hand side.

6.5 Data

Before processing, experimental data are first converted to ROOT files. During this stage the ADC channels are remapped to obtain an identical channel mapping as is used during the simulations.

6.5.1 Recorded Data

During the measurement, the following data are recorded and saved in a binary format with the following data being recorded:

Time: Unix time was recorded as time stamp for each moment the data was taken.

Temperature: The temperature sensor on the back side of the SiPM array was read every 15 seconds.

Trigger: For each event the ADC of the trigger detector was readout from the CAEN V965 VME module.

SiPM array: ADC for the each of the 16 SiPM channels was readout from the CAEN V792 VME module and stored together with the trigger ADC.

Position: The position of the module was saved as the index of the current step of the translational stage.

6.5.2 Raw Data Conversion

To simplify the further analysis, these binary data files are converted to a ROOT file. The following ROOT trees are saved in the file:

RUN information: The number of positions per direction and number of steps per position.

Temperature data: The Unix time stamp, device ID for the SUB-20 device and temperature sensor, and temperature.

Event data: The Unix time stamp, event number, module position, ADC of the trigger detector, and ADC values for all channels of the SiPM array.

RUN information contains basic information regarding the measurement. For each measurement the number of measurement points, i.e. the number of positions, is stored. In addition, for each direction of the translational stage, the number of steps of the motor per measurement point, i.e. per position index, is saved.

Temperature data was kept separately from the ADC data due to the temperature being recorded every 15 seconds while ADC data was recorded at a much higher rate. During raw data conversion to the ROOT data format no analysis of any data was performed.

6.5.3 Channel Remapping

To ensure consistency on channel mapping compared to the channel map from the simulations a remap of several channels was required. Remapping the channels enabled the use of the same analysis code as for the simulated events. Code reuse ensures that the analysis of both sets of data, experimental and simulated, is performed in an identical manner. Comparison and interpretation of the results can then be done consistently.

The channel remapping is handled during the conversion from raw to ROOT data. In fig. 6.8, the remapping of the original channels to the mapping from the simulations is shown. Due to the way the SiPM channels are internally connected in the array, only the bottom two rows of all the channels required a remapping. The remapped channels are marked in the white rows with their original (new) channel numbers in red (green resp.). More details regarding all the SiPM channels and their remapping can be found in appendix C.

During the DOI scans, the source is located on the left side of the schematic, fig. 6.8. The lack of information regarding the exact point of interaction along the trajectory of the gamma rays requires a grouping together of the data from four SiPM channels. For the chosen orientation of

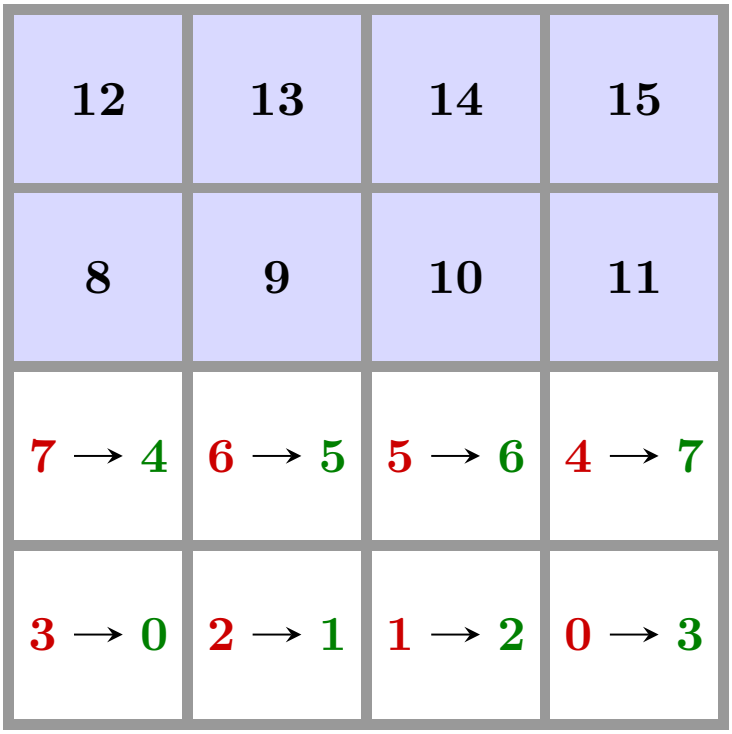

Figure 6.8: Schematic of the channel remapping where the white channels represent the remapped channels. The original channel numbers are indicated in red while the newly obtained channel numbers are indicated in green.

the PET module, section 6.4.2, the following channels are grouped together: 0–3, 4–7, 8–11, and 12–15. As a consequence, the ADC fraction f_k and χ^2 distributions will differ from those presented in chapter 4.

Chapter 7

Measurements of Performance

7.1 Data Preprocessing

The preprocessing stage of the data involves identifying the events that originate from a positron-electron annihilation. In the first stage, ADC histograms are built as a function of time for the trigger and the individual channels from the SiPM module. With these histograms, ADC cutting ranges are determined for the trigger and channels of the SiPM array. Simultaneously, the pedestals for the channels in the SiPM array are extracted from these ADC histograms. The results for these cutting ranges and channel pedestals then allow to build an ADC histogram as a function of time for the ADC spectra of the full module.

The module ADC spectra are then used to determine the photopeak (PPK) location. Together with the temperature data, a scaling factor is then determined to apply temperature corrections to the ADC. After temperature corrections have been applied, scaling factors for the channels of the module are determined to compensate for gain variations between the SiPM channels caused by the variation in channel breakdown voltages.

7.1.1 Trigger Energy Spectra

Energy spectra for the trigger (single SiPM) are constructed by filling a histogram with the raw ADC values of the trigger detector recorded for each event. Such histograms are made for each measurement point (position) to minimize the influence of temperature variations during the measurement. Figure 7.1a holds all trigger ADC spectra for a particular run. There is a clear variation of the trigger PPK location during the measurement.

A Gaussian fit,

$$f(x) = A + B \cdot \exp\left(-\frac{(x-\mu_{\text{TRG}})^2}{2\sigma_{\text{TRG}}^2}\right), \tag{7.1}$$

was applied to determine the mean (μ_{TRG}) and sigma (σ_{TRG}) of the trigger PPK. The fit results are then saved for further analysis of the PET module data.

The Gaussian fitting process was guided by setting the initial value for μ_{TRG} to the position of maximum value within the range near the PPK. Fitting range limits for μ_{TRG} where then set to a limited range ($\pm$100 ADC bins wich corresponds to $\approx 2.8 \cdot \sigma_{\text{TRG}}$) around the maximum bin. Fitting parameters for σ_{TRG} were limited in the range of 50 to 150 ADC bins. In fig. 7.1b, the result of this fitting procedure is shown for a single position of the measurement. The black histogram shows the raw trigger data for the position with index 210, while the blue histogram contains the trigger data after applying a cut on the PPK of the full PET module ADC (explained later). Both histograms were scaled to the maximum of the raw trigger ADC spectrum.

Further analysis applies a cut on the trigger ADC by only taking into account events with a trigger ADC value that fall in between the range of $\mu_{\text{TRG}} \pm 2.35 \cdot \sigma_{\text{TRG}}$.

7.1.2 Channel Pedestals

Pedestals for the 16 SiPM channels in the PET module were determined by filling the recorded ADC values for each channel (a_{ch}) into their respective energy histograms; fig. 7.1c presents an ADC histogram for one of the SiPM channels of the SiPM array. For each measurement point (position), the pedestal peak for all the channel histograms was fitted with a Gaussian function similar as eq. (7.1). This provides channel pedestal values for each position in the measurement, minimizing the impact of potential changes in the signal pedestal.

During further analysis, the pedestal values for each module channel ($ch = 1 \cdots 16$) were set to the μ^{ch}_{PED} from the fit results. For each SiPM channel, those pedestal values μ^{ch}_{PED} are subtracted from the recorded channel ADC values,

$$h_{ch} = a_{ch} - \mu^{ch}_{\text{PED}} \ , \tag{7.2}$$

with a_{ch} representing the raw ADC value of channel ch for a particular event. This pedestal subtraction is performed for each event while ensuring that the pedestal values are updated for each position.

7.1.3 PET Module ADC

Light sharing over the SiPM channels due to the segmented crystal structure requires the summing of all channel signals to obtain the full measured event energy. Before summing the channel signals, the raw channel ADC values need to be corrected for their individual pedestals. Channel ADC pedestals

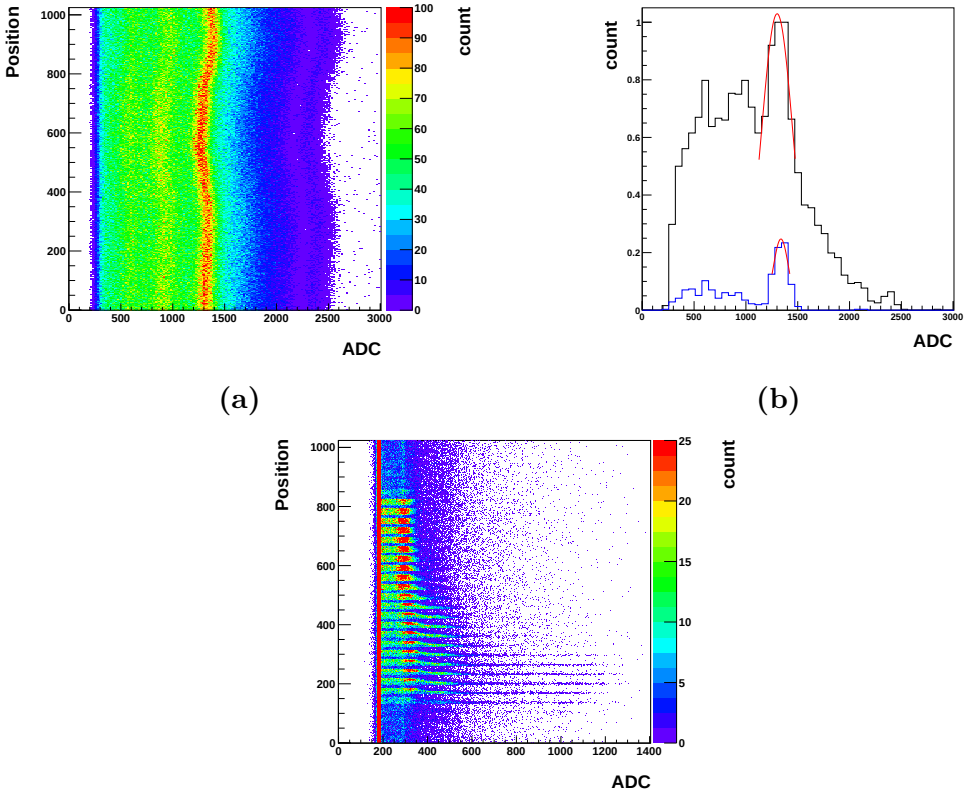

Figure 7.1: Example of ADC histograms used during the preprocessing stage of the analysis of a measurement. The top histograms contain all the data for all positions along the X scan direction while the bottom histogram contains the trigger data for a single position: (a) trigger ADC spectra over time during a measurement, (b) trigger data for the position with index 210. The blue spectrum contains the trigger data for the same position after applying a cut on the PPK of the summed module ADC (explained at a later stage). (c) Raw channel ADC (a_{ch}) for a single channel.

were determined in section 7.1.2 and subtraction of these pedestal values from the raw channel ADC values leads to a pedestal corrected measured energy H as

$$\begin{aligned} H &= \sum_{ch=1}^{16} (a_{ch} - \mu_{\text{PED}}^{ch}) \\ &= \sum_{ch=1}^{16} h_{ch} \ . \end{aligned} \tag{7.3}$$

In the remainder of this work when discussing the measured energy, we will mean H from eq. (7.3).

A new ADC histogram as a function of time (position) is made for the module ADC sum H, where for each event a cut is made on the trigger PPK. Through Gaussian fits, the ADC pedestal location μ_{PED} and PPK location μ_{PPK} with σ_{PPK} are determined for the module ADC sum H. The fitting process was carried out similarly as in section 7.1.1 for the PPK while the pedestal was determined through a fit with a Gaussian function around the ADC value of 0.

7.1.4 Module Location and Orientation

SiPM channel locations are important for reconstruction of the interaction point due to the need for knowledge of the relative source position in relation to the module and the SiPM channels. Additionally, once the module and channel locations are known, all further analysis is limited to a region of interest (ROI) which is limited to the location of the module in the scan data. The ROI has a small margin added to the module location to ensure that all measurement points situated within the boundaries of the module are included in the further analysis.

To determine the location of the module in the scan data, first a 2D histogram is constructed which contains, for each measurement point, the number of events with a measured energy H that falls within the PPK.

The number of events within the PPK for each measurement point are obtained after the PPK fit for the measurement point has been performed according to the fitting procedure described in section 7.1.3. For each measurement point, the previously obtained parameters μ_{PPK} and σ_{PPK} of the PPK are then used to integrate the PPK within the range $\mu_{\text{PPK}} \pm 2.355 \cdot \sigma_{\text{PPK}}$. This results in the number of events with a measured energy H that falls within the PPK. Figure 7.2a presents the resulting histogram holding the number of events within the PPK for each measurement point. It illustrates that the location of the module can clearly be distinguished in the scan data.

The data presented in fig. 7.2a is then projected onto the X and Y axis (Z axis for DOI scans). These projections are made for each bin where each bin along the X axis will be projected onto the Y axis and vice versa. Linear fits are then applied to the leading and trailing edges of these projections. The points on those linear fits which are separated by the width of the module from each other are taken as the edges of the module. For the DOI scans, the distances between the points needs to match the length of the crystal.

Due to the module potentially being rotated in the plane of the detector, an angle of rotation is determined. The found edges are added to graphs, separated by scan direction and lower or upper edge for each direction. These graphs, see fig. 7.2b are then fit with another linear function to find the angle

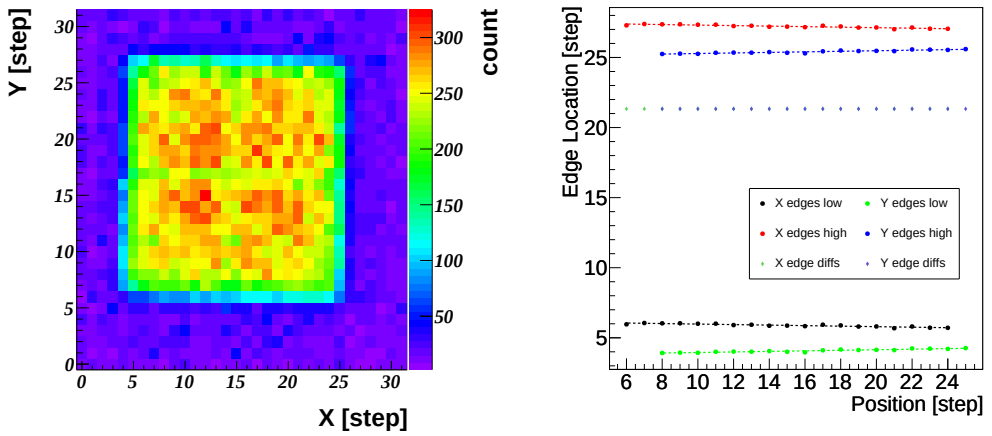

(a) (b)

Figure 7.2: Figures used to find the module location and rotation: (a) 2D histogram holding the number of hits in the PPK, (b) graphs containing the results for the edges for each bin lying in between the general edges.

of rotation.

Finally the ROI is taken to be the outermost edges with an additional bin added as margin. During further analysis, only data within the ROI is taken into account.

7.2 PET Module Calibration

After the preprocessing stage of the data, a calibration procedure is applied to recorded data from the PET module. Due to the temperature dependence of the SiPM gain and the LYSO light yield, a correction for the temperature is required. There is also a difference in optimal operating bias between the individual SiPM channels which needs an additional correction to smoothen out the difference in SiPM gains.

7.2.1 Temperature

Throughout each measurement, the temperature of the module was registered to enable temperature corrections for the channel ADC values. Figure 7.3 presents the average temperature at each position during a measurement where fig. 7.3a shows the average temperatures as a function of overal position index, i.e. it illustrates the temperature variations as a function of measurement progress. Figure 7.3b compares the average temperature with the module PPK obtained in section 7.1.3. It clearly illustrates the dependence of the SiPM gain versus temperature.

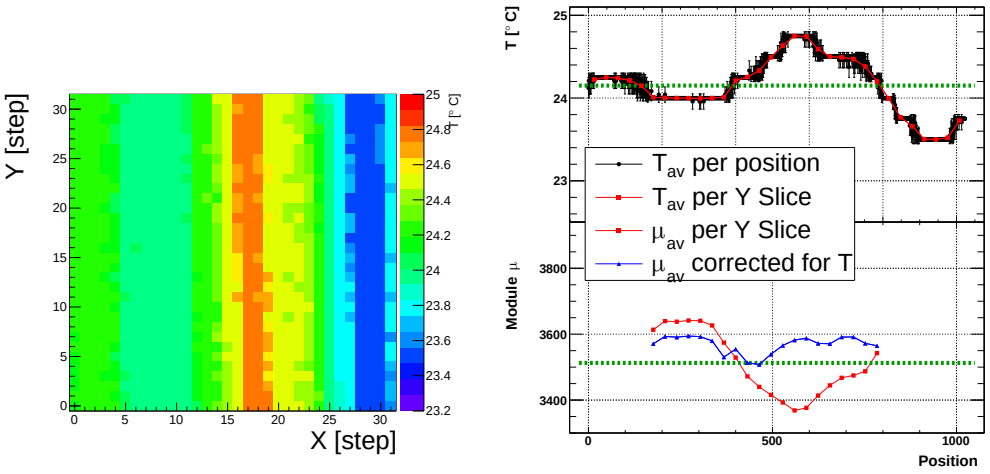

(a) **(b)**

Figure 7.3: Average temperature during a measurement (XY scan at 72.35V): (a) Average temperature per measurement point, (b) Average temperature variation (top) compared to the mean of the module PPK (bottom).

Compensation for temperature variations of SiPMs during measurements relies on the determination of the temperature coefficient k'_T. Usually this coefficient is determined by measuring the SiPM signal originating from a known number of photons n_{phn} at different temperatures. For SiPMs the coefficient k'_T is then determined with [12, 50]

$$k'_T = \frac{1}{A} \cdot \frac{\Delta A}{\Delta T} \ , \tag{7.4}$$

where $A = n_{phn} \cdot M$ represents the SiPM signal, with M the SiPM gain given by eq. (2.2), ΔA the change in SiPM signal and ΔT the temperature difference between both measurements.

On the other hand, the light output of scintillators also exhibits a temperature dependence [51, 52]. Thus to be able to apply a correction for the temperature requires to determine the temperature dependence of the full PET module, scintillator with SiPM array. A scatter plot was made of the PPK mean μ_{PPK} versus the average temperature of each measurement point, fig. 7.4. A linear fit is then applied to extract a temperature coefficient k_T which represent a linear dependence of the gain on temperature as follows

$$\mu_{\text{PPK}} = k_T \cdot T + C \ . \tag{7.5}$$

Based on eq. (7.5), the temperature correction for the PPK mean μ_{PPK} is then obtained with

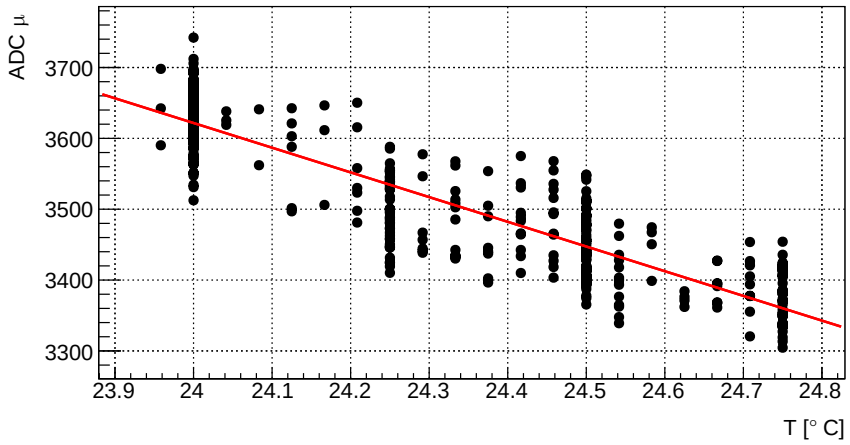

Figure 7.4: PPK mean μ_{PPK} for each measurement point as a function of average temperature for the measurement point.

$$\begin{aligned} \Delta\mu &= k_T \cdot \Delta T \\ \mu_{cor} &= \mu_{\text{PPK}} - \Delta\mu \ , \end{aligned} \tag{7.6}$$

where ΔT is the difference between the current temperature and the average temperature of the entire measurement. The average temperature is indicated with a green dashed line in the upper graph in fig. 7.3b. The green dashed line in the lower graph represents the average location of the PPK before temperature correction.

The results for the temperature correction applied to the PPK mean μ_{PPK} are shown in fig. 7.3b. The red data points are values of the original and thus uncorrected PPK mean μ_{PPK}, while the blue data point represent the temperature corrected values. The correction factor applied during temperature correction was obtained from the linear fit shown in fig. 7.4. Correction of the PPK values was applied using eq. (7.6). The remainder of the fluctuations are attributed to variations in light collection efficiency and gain fluctuations between the different SiPM channels.

7.2.2 Compensation of Gain Variation

Due to each individual SiPM channel having its own breakdown voltage, the individual channels will have different gain, see eq. (2.2). Additionally, there can be variations in light collection efficiency and amplification between the different SiPM channels. All effects combined could lead to inaccuracies in the measurement of the spread of the scintillation photons in the PET module which in turn results in errors in the reconstruction of the interaction point.

A histogram containing pedestal corrected ADC values for the individual channels is presented in fig. 7.5. This histogram is created by making a cut on the trigger PPK, while checking if the source was situated above a particular SiPM channel. Finding the SiPM channel is done by checking if the position of the measurement point falls within the boundaries of a particular channel. Boundaries for all channels were obtained in section 7.1.4. If the location of the measurement point can be associated to a channel, then the pedestal corrected ADC value for that channel is filled into the histogram.

These location cuts result in a clearly distinct PPK being present in the ADC histogram for each channel. Comparing the location of the PPK in each one of the ADC spectra for the different SiPM channels in fig. 7.5 (Y axis), it is clear that the above described issues are present.

Minimizing the influence of these inaccuracies are vital to the resolution of the interaction point reconstruction. The following calibration procedure is used to extract a set of 16 scaling parameters, $c_0, \ldots, c_{15}$, to scale the channel ADC values, $h_0, \ldots, h_{15}$, and equalize the measured light sharing. The mean signal sum $\overline{H}$ is extracted from the data of each measurement point by applying a Gaussian fit to the histogram containing the full measurement ADC H.

For the entire measurement, the χ^2 is defined as the sum of the squared difference between the mean signal sum $\overline{H}$ and the sum of scaled signals $c_{ch}h_{ch}$,

$$\chi^2 = \sum_{i=0}^{N} \left[\overline{H} - (c_0 h_0^i + c_1 h_1^i + \cdots + c_{15} h_{15}^i)\right]^2 , \tag{7.7}$$

index i runs over the number of events N having an H value within in the PPK. To obtain the scaling parameters $c_0, \ldots, c_{15}$, it is necessary to minimize the χ^2 distribution eq. (7.7). This requires the partial derivatives of eq. (7.7) to the scaling parameters $c_0, \ldots, c_{15}$

For j running over the 16 channels ($j = 0, \ldots, 15$) this becomes

$$0 = \frac{\partial\left(\chi^2\right)}{\partial c_j} = \sum_{i=1}^{N} \left[\overline{H} - \sum_{k=0}^{15} c_k h_k^i\right] \cdot (-h_j^i) \ . \tag{7.8}$$

Rearranging the terms in eq. (7.8) and making the following substitutions: $\sum_{i=1}^{N} h_j^i = b_j$ and $\sum_{i=1}^{N} h_j^i h_k^i = H_{jk}$ results in

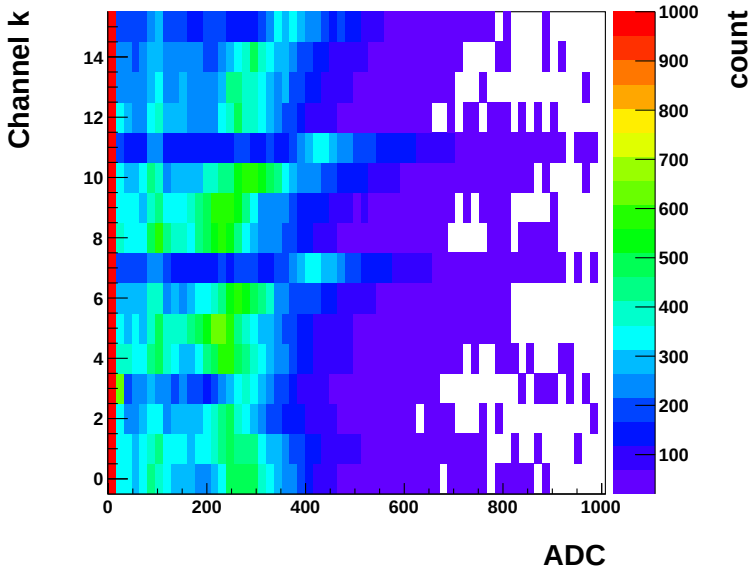

Figure 7.5: SiPM channel ADC histogram illustrating the variation in PPK location between the channels.

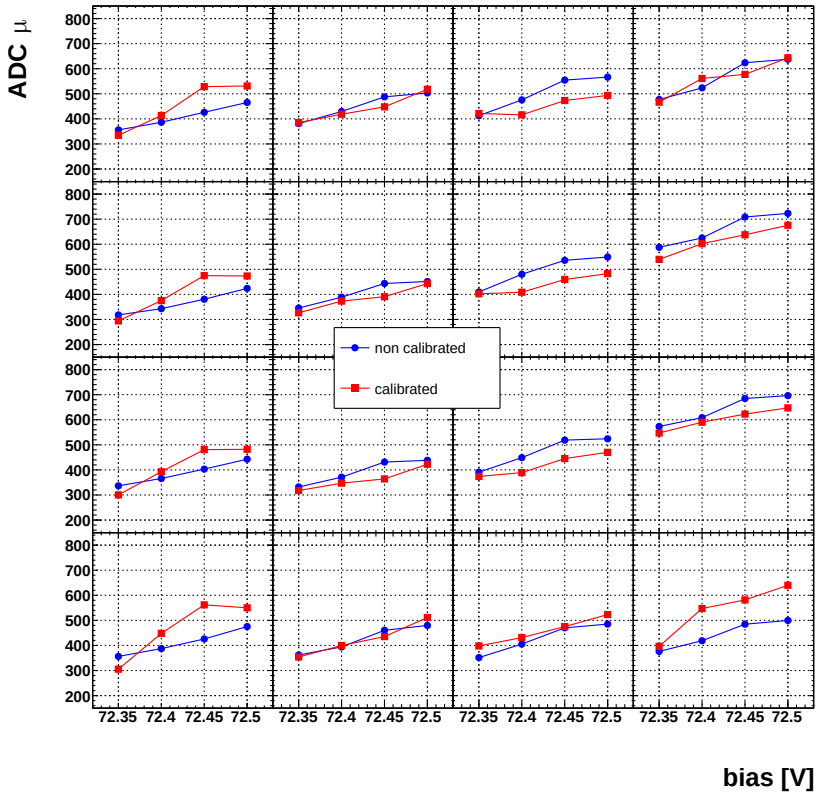

Figure 7.6: Comparison of channel PPK locations for various biases before (blue) and after (red) application of the scaling factors.

$$\overline{H} \cdot \sum_{i=1}^{N} h_j^i = \sum_{i=1}^{N} \left[h_j^i \cdot \left(\sum_{k=0}^{15} c_k h_k^i \right) \right] ,$$
$$\overline{H} \cdot b_j = \sum_{k=0}^{15} \left[c_k \cdot H_{jk} \right] . \tag{7.9}$$

Eventually this provides a set of 16 equations of the form eq. (7.9) that can be replaced by a matrix equation and solved by calculating the inverse matrix of $\mathcal{H}$

$$\overline{H} \cdot \vec{b} = \mathcal{H} \cdot \vec{c} \tag{7.10}$$
$$\vec{c} = \overline{H} \cdot \mathcal{H}^{-1} \cdot \vec{b} \, , \tag{7.11}$$

with $\mathcal{H}$ given by

$$\mathcal{H} = \begin{pmatrix} \sum_{i=1}^{N} h_{j=0}^i h_{k=0}^i & \cdots & \sum_{i=1}^{N} h_{j=0}^i h_{k=15}^i \\ \vdots & \ddots & \vdots \\ \sum_{i=0}^{N} h_{j=15}^i h_{k=0}^i & \cdots & \sum_{i=1}^{N} h_{j=15}^i h_{k=15}^i \end{pmatrix} . \tag{7.12}$$

From eq. (7.11) it follows that the mean value of the sum of signals $\overline{H}$ merely acts as a scaling constant to find the channel scaling factors.

Several measurements at varying bias have been performed. For each of the measurements the above described calibrations procedure was performed. After calibration, the data for each measurement was re-analysed and the obtained scaling factors were used to correct the channel ADC, using the measurement specific factors.

PPK locations for each channel before and after applying the scaling are compared in fig. 7.6. While the calibration procedure can not perfectly correct the variation in gain of all the SiPMs, it does manage to bring the gain levels of the majority of SiPMs to similar levels. Mostly notably the procedure has difficulties in bringing the SiPMs with the largest gain in line with the others.

7.3 Energy Resolution of the PET Module

After the preprocessing and calibration of the data, an analysis of basic PET performance is done by re-analysing the data. This limits the data to

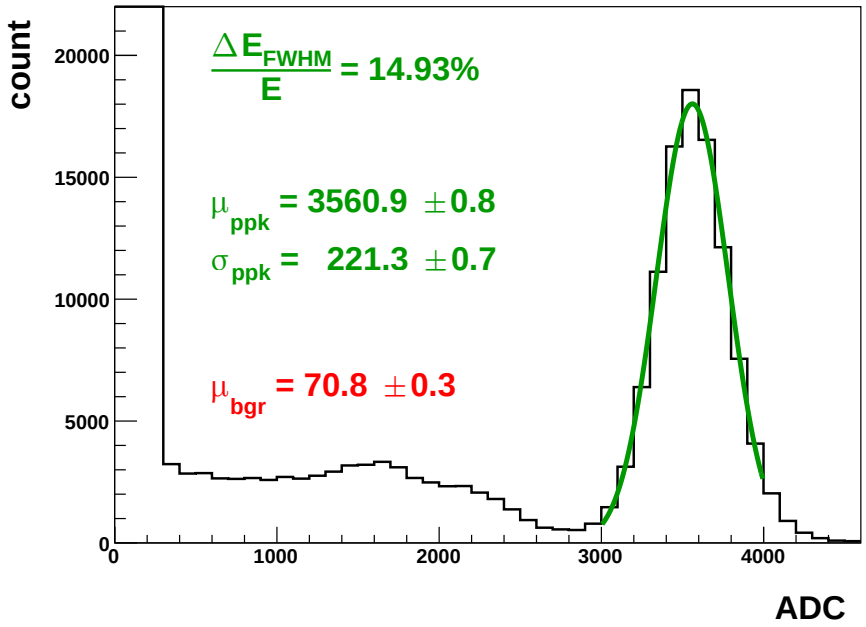

Figure 7.7: Energy spectrum of a full XY scan. Results of the fitting procedure are shown as well.

only include events that originate from a positron-electron annihilation. The parameter of interest in this section is the energy resolution.

The energy resolution is determined by recreating a histogram, with the calibrated full module measured energy, H_{cal}, an example is presented in fig. 7.7. To produce this new histogram, a cut to the trigger PPK was applied. A Gaussian fit was then applied to the resulting energy histogram. From the fit results the energy resolution, FWHM, is then extracted with the following equation

$$\frac{\Delta E}{E} = \frac{2.35 \cdot \sigma_{\text{PPK}}}{(\mu_{\text{PPK}} - \mu_{\text{PED}})} \ , \tag{7.13}$$

with μ_{PPK} and σ_{PPK} being the fit results corresponding to the PPK and μ_{PED} the location of the pedestal.

Measurements for the performance of the PET module ran over considerable amounts of time. During these measurements there were small variations in the environmental variables (temperature, bias, source position). In section 7.2.1 the importance of temperature corrections was already discussed. Section 7.2.2 then discussed the calibration procedure to ensure the optimal energy resolution for the PET module. This section explores the influence on the energy resolution of the following effects:

- applied bias fluctuations,

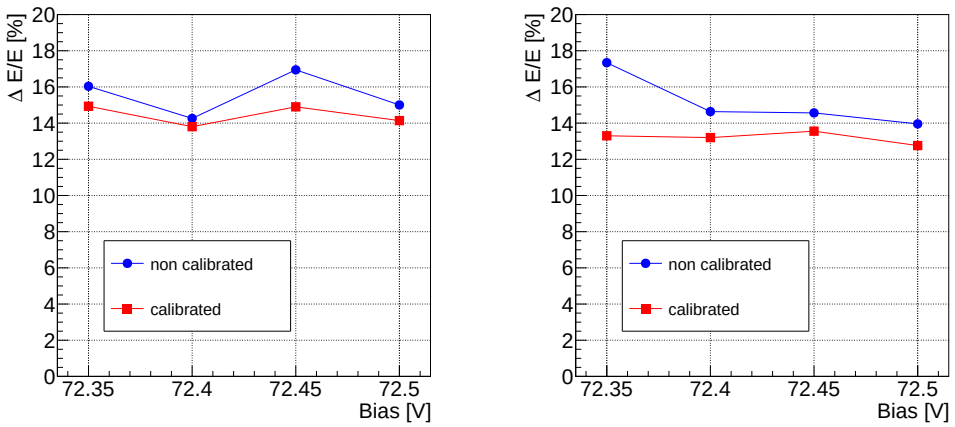

(a) **(b)**

Figure 7.8: Energy resolution, FWHM, of the module performed with bias ranging from 72.35 V to 72.5 V (non calibrated v.s. calibrated data): (a) FWHM as a function of bias for the XY scans, (b) FWHM as a function of bias for the DOI scans.

- overall position index, i.e. measurement progress.

7.3.1 Applied Bias Dependence

The SiPM gain is related to the applied bias, its breakdown voltage, and its capacitance, see eq. (2.2). Each SiPM in the array has a different breakdown voltage leading to the differences in optimal bias as presented in appendix C. In addition, each SiPM can have a different capacitance which acts as a scaling factor for the SiPM gain. Considering that a single bias is applied to the entire module, these difference in capacitance can result in a non-uniform variation of the gain between the SiPM channel during fluctuations of the applied bias.

Ultimately, the applied bias should be kept as stable as possible to reduce gain fluctuations. However, bias fluctuations can not be fully eliminated. To study the influence of bias fluctuation on the energy resolution, several measurements were performed at various bias values. These bias increments were chosen to be slightly larger, 50 mV, than the ripple of the power supply, <10 mV.

The results for the energy resolution for all the measurements with different bias are shown in fig. 7.8. Overall from the results presented in fig. 7.8a (XY scans) and fig. 7.8b (DOI scans) it is apparent that bias fluctuations hardly influence the energy resolution.

In additions the figures presented in fig. 7.8 provide a comparison between non-calibrated and calibrated (including temperature correction) of

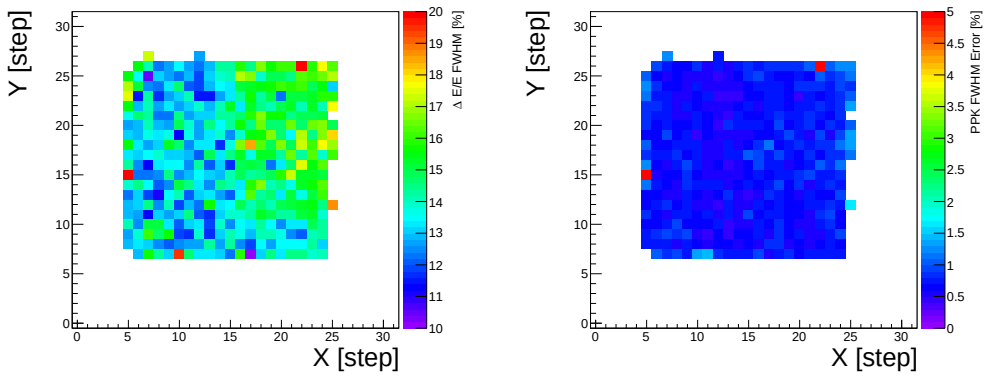

(a) **(b)**

Figure 7.9: Energy resolution, FWHM, for a measurement performed with a bias of 72.35 V: (a) FWHM as a function of XY source location (b) FWHM error as a function of XY source location.

the results. A slight improvement of ≈1 % in the energy resolution is obtained with the calibrated data.

7.3.2 Source Location

During the measurement, the location of the source is constantly moved over the entry surface of the PET module. Considering the non-symmetrical nature of the structure of the segmented scintillator crystal, 2D figures of the FWHM, for a single measurement, are presented in fig. 7.9. In both figs. 7.9a and 7.9b the limitation of the data to the ROI is apparent, resulting in only the location of the module being shown.

The variation of the FWHM as a function of the source location is shown in fig. 7.9a. From the figure it becomes clear that the energy resolution is not perfectly uniform over the entire scan surface. In particular the right hand side of the scan surface has a minor degradation of the energy resolution. This degradation coincides with the gain differences between the SiPM channels, see appendix C.

Similarly as for the energy resolution, the error for the FWHM for each position is presented in fig. 7.9b. Errors for the FWHM were calculated with

$$\delta\left(\frac{\Delta E}{E}\right) = \frac{\Delta E}{E} \cdot \sqrt{\left(\frac{\delta\sigma_{\text{PPK}}}{\sigma_{\text{PPK}}}\right)^2 + \left(\frac{\delta\mu}{\mu}\right)^2}\,, \tag{7.14}$$

with $\mu = \mu_{\text{PPK}} - \mu_{\text{PED}}$ being the pedestal corrected value of the PPK location of the summed signal H. The errors $\delta\mu$ and $\delta\sigma_{\text{PPK}}$ are obtained from the fit

results. The error $\delta\mu$ was obtained from combining the errors of μ_{PPK} and μ_{PED} as follows

$$\delta\mu = \sqrt{(\delta\mu_{\text{PPK}})^2 + (\delta\mu_{\text{PED}})^2} \ . \tag{7.15}$$

The resulting errors on the energy resolution are pretty uniform over the entire scan surface. Thus the non-uniformity of the energy resolution can mostly be attributed to differences in optimal operating biases of the SiPM channels. To compare the influence of the data calibration procedures, the energy resolution is plotted as a function of overall position index. The results are presented in fig. 7.10.

Each measurement point in the presented figures corresponds with a single line scan along the Y direction at a fixed X position. Effectively it presents the measurement progress of the full scan. For the XY scans, each line scan spans over four SiPM channels while for the DOI scans, these line scans provide the energy resolution at each step along the depth of the crystal.

XY Scans

The energy resolutions, at different bias, before applying the calibration procedure are shown in fig. 7.10a. It clearly reflects the degradation of the energy resolution which can be observed at the right hand side of fig. 7.9a. The SiPMs with the largest gain are situated on the right hand side of the module, see appendix C.

After applying the calibration procedure, the variation in gain between the SiPMs is reduced, see section 7.2.2. Thus it becomes possible to recover from the degradation of the energy resolution on the right hand side of the PET module. From fig. 7.10b it can be seen that the calibration procedure mostly removes the degradation.

DOI Scans

During the DOI scans, the orientation of the PET module was such that the gamma source was placed on the left side of the module (left side of fig. 6.8). This orientation results in the gammas entering the crystal on the side where the SiPMs with the lowest gain are situated. While the resulting energy resolution degrades during the scan, by calibration this can be successfully compensated as shown in fig. 7.10d. The result is a more uniform energy resolution along the entire depth of the crystal.

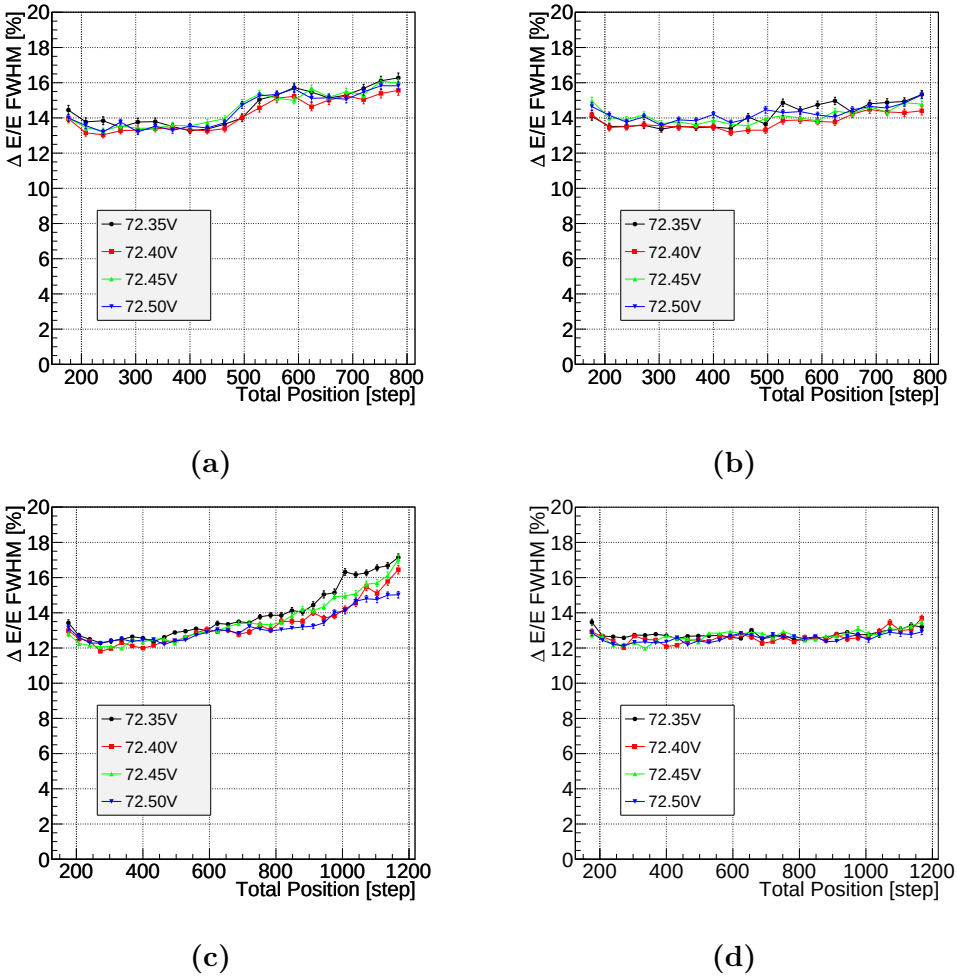

Figure 7.10: Energy resolution, FWHM, for the XY and DOI measurements performed with bias in the range from 72.35 V to 72.5 V (non calibrated v.s. calibrated data). The results are presented as a function of the scan position: (a) non calibrated data of the XY scans, (b) calibrated data of the XY scans, (c) non calibrated data of the DOI scans, (d) calibrated data of the DOI scans.

Chapter 8

Comparison of Simulation and Experiment

The simulations provided the full information for each of the gamma interactions in the scintillation crystal (i.e. deposited energy, position, etc.). Generally, during the experimental verification of the DOI reconstruction, a large part of this information is not available. In particular, the only information that is available during the measurements are the two dimensional position of the source relative to the PET module and the measured signals.

It would be ideal if one could employ simulations to obtain realistic sets of parameters that can be applied to reconstruction of real data. The focus of this chapter is to link the results from simulation to those obtained through measurements.

8.1 Simulation: Projected Distributions

Simulations provide channel fraction f_k distributions for all 64 cubes due to the availability of the location of the interaction point in 3D. During the measurements, on the other hand, the location of the interaction point is only approximately known in 2D, namely only in the plane of the scan. The third dimension, the position along the beam of gamma rays, will always be unknown. Two dimensional projections of simulated data are therefore produced to understand how the 2D channel fraction f_k distributions compare to the 3D distributions from the simulation data.

The starting positions for the gamma rays are uniformly generated in a plane parallel to one of the faces of the scintillator crystal. In total there were two planes which were chosen from which gamma rays were emitted towards the crystal.

Front: Gamma enters the scintillation crystal through the front face with a momentum direction towards the SiPM array.

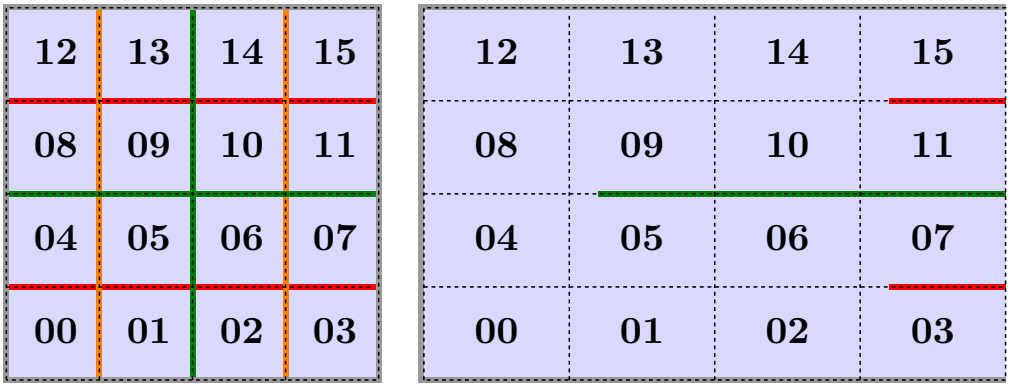

Figure 8.1: Schematic of the pillar mappings. (a) XY scans and (b) DOI scans. The reflectors are indicated with the following color codes: green (central), orange (long subsection reflectors), and red (short subsection reflectors).

Perpendicular: The plane was set to be parallel to one of the scintillator side faces, namely the side face illustrated in fig. 2.4c. The primary gamma rays, generated in this plane, were given a direction towards the scintillator crystal.

Similarly as before, the plane from which primary gamma rays were generated was always set at a distance of 5 mm from the edge of the scintillator crystal.

8.1.1 Pillar Mapping

While the simulation data contain the full information regarding the interaction points of the gammas inside the scintillation crystal, the measurements lack this 3D information. In particular, there is no information for the position of the gamma interaction along the axis of the collimated beam of gamma rays. As such, the cube reconstruction method needs adjustment to account for this lack of 3D information. This lack of information necessitates the adjustment of the cube mapping, as discussed in section 4.4.

For each type of scan a 4×4 grid is made in the plane of the scan. This results in a mapping which combines 4 cubes, from the original 64 cubes, together into a single so-called pillar. Each pillar consists of the 4 cubes which are in line with each other, from the point of view of the source. This mapping reduces the original 64 cubes to a grid of 4×4=16 pillars. The newly obtained mappings for the XY and DOI scans are illustrated in fig. 8.1.

To determine the pillar mapping in the measurement data for the XY scans, the information regarding the SiPM channel locations, see section 7.1.4, is used to construct the pillar map. The channel centers from the channel mapping are taken and around each center a 2D box is constructed. Dimensions of each box are $3.2 \times 3.2\,\mathrm{mm}^2$. The single side dimension of a pillar originates from dividing the module area into 4×4 equal parts resulting in sides with a $12.8/4 = 3.2\,\mathrm{mm}$.

This yields a mapping similar to the cube mapping in the simulations, section 4.4, with the main difference being the layer mapping. Essentially this mapping combines the cubes from the different layers but with same X, Y location, in the plane of the detector, into a single pillar.

8.1.2 ADC: Channel Fractions

The ADC channel fractions f_k are crucial for the cube reconstruction method as described in section 4.4. Distributions for the channel fractions f_k need to be made from which the sets of reconstruction parameters, $(\overline{f_k^j}, \sigma_k^j)$, are extracted. The channel fractions f_k are defined as

$$f_k = \frac{h_k}{H} \ . \tag{8.1}$$

where for the simulation data, h_k is the detected number photons by channel k, while for the measurement data it is the measured signal for that channel. H is the sum of either the total number of detected photons (simulation) or the signals of all the SiPM channels (measurement).

Projected distributions are produced, from the simulation data, by filling channel fraction f_k histograms for each pillar. These histograms are produced in a similar manner as described in section 4.4, where the cubes are now replaced by the pillars as described above.

The ADC fraction distributions for the measurement data are created in a similar manner as for the simulation data. For each measurement point, the pillar corresponding to the source position is determined. Then all the channel fractions f_k are filled into a histogram that corresponds to that pillar. This results in 16 histograms each containing 16 ADC distributions (one distribution for each channel). In fig. 8.2, the ADC fraction distributions for pillar 15 are shown for all the channels. Once the ADC channel fraction distributions are created, values for the mean channel fractions $\overline{f_k^j}$ and RMS σ_k^j are extracted from each distribution. This results in 16 sets of parameters $(\overline{f_k^j}, \sigma_k^j)$ for each pillar.

A separation is made between the XY and DOI type scans made for the experimental measurements. The *front* type simulations provides 2D projections to compare them with experimental scans in the XY plane. The

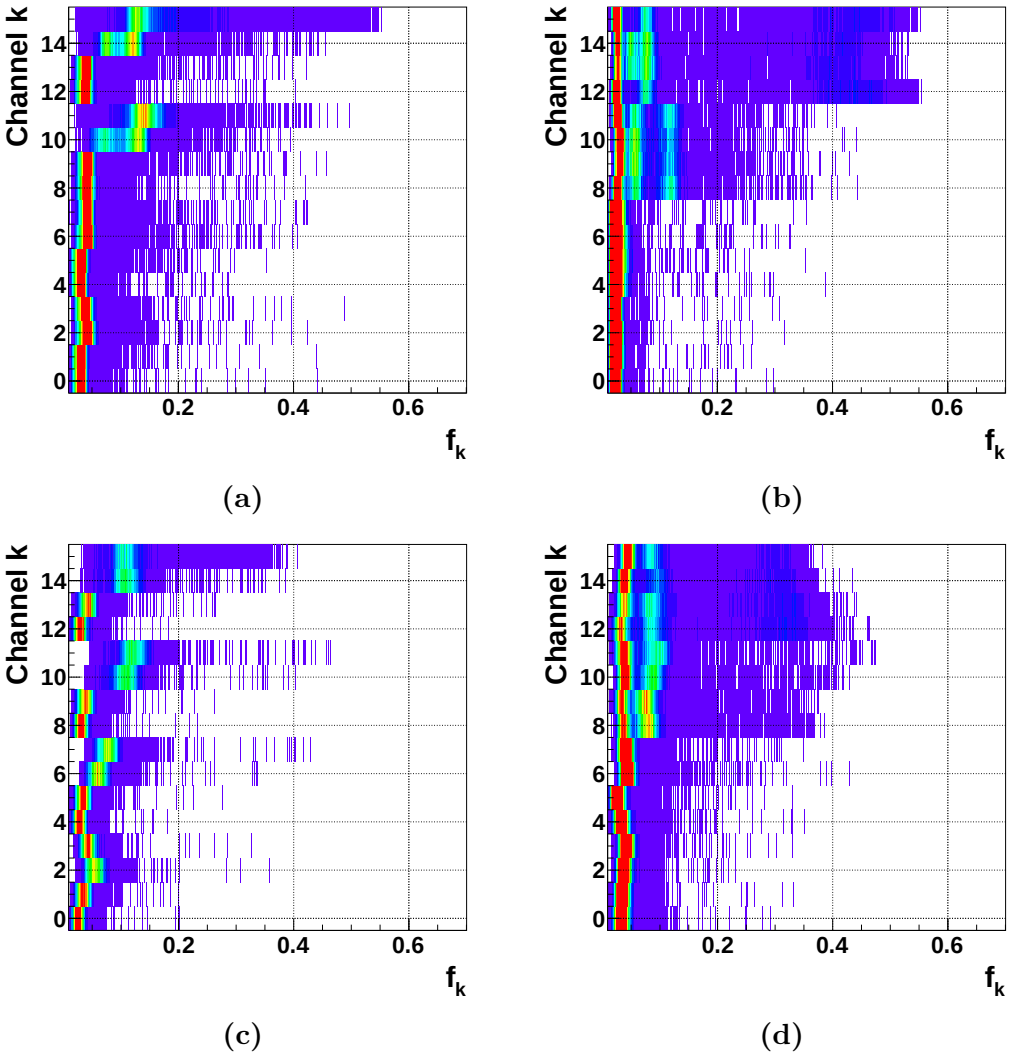

Figure 8.2: Example ADC fraction distributions for pillar 15 for simulation and measurement data for both types of scans. Distributions for the simulations: (a) *front* and (b) *perpendicular* type simulations. Distributions for the measurement data: (c) XY scans and (d) DOI scans.

2D projections of the *perpendicular* type of simulations are for comparison with experimental scans covering the side of the segmented crystal. The side scans are required to obtain DOI distributions for the ratios. Each of the two types of simulations provide projected distributions by grouping together the cubes which are stacked on top of each other, as seen from the source, similarly as described in section 8.1.1.

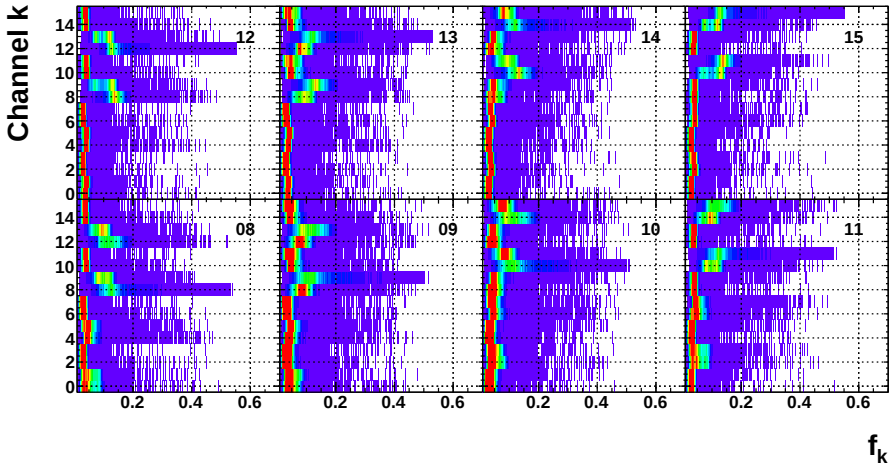

(a)

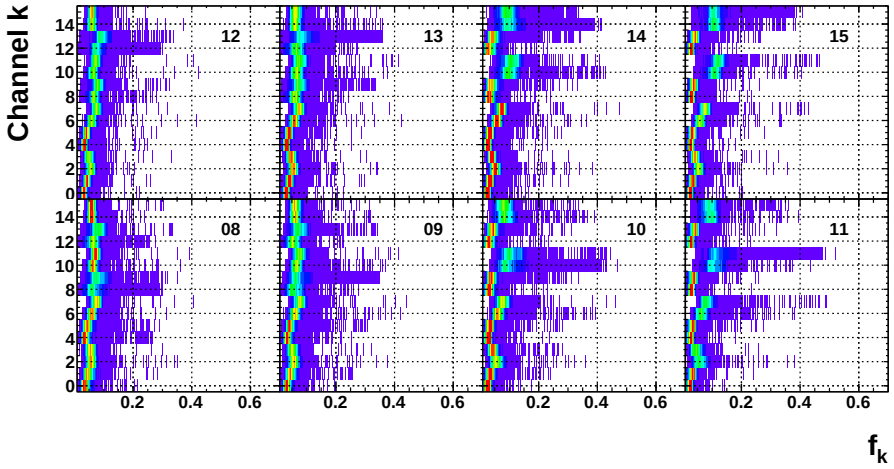

(b)

Figure 8.3: Comparison of the ADC channel fractions f_k, for the top two rows of pillars with indices 8–15 (see figures), between simulations and experimental data: (a) Simulation data with the first gamma interaction as reference point, (b) experimental data obtained at a bias of 72.35 V.

XY scans

During the experimental XY scans, the gamma rays enter the PET module from the front face. Thus, the comparison of experimental results for the XY scans is done with the *front* type of simulations. In fig. 8.3, histograms for the ADC channel fractions f_k are presented for the *front* type simulations and the experimental data performed at an applied bias of 72.35 V.

Only the upper two rows of pillars, i.e. 8–15 as seen in fig. 8.1a, are shown.

Due to symmetry of the segmented crystal, the results for the bottom two rows are similar and thus not presented. All histograms were scaled to their maximum and their range along the Z axis was limited to 0.5 which allows a direct comparison of the distributions. The ordering of histograms in each of the figures is according to the pillar mapping as presented in fig. 8.1a and is indicated with pillar index in each individual histogram.

The histograms in fig. 8.3a present the results for the projected distribution obtained from the simulation data. Each figure presents the channel fractions f_k for one particular pillar. One can see that the channel fractions f_k have their peak at larger f_k for all channels which are in the same quadrant, i.e. the quadrant where the gamma interaction occurred. As an example, the histogram for pillar 12 (upper left) shows channel fraction distributions shifted towards higher values f_k for the pillars 8, 9, 12 and 13. All those pillars belong to the same quadrant as can be seen in fig. 8.1a, i.e. the upper left quadrant.

The other channels clearly show channel fractions distributions situated around lower f_k values. Even more so, these fraction distributions at low f_k are nearly identical for all the channels. This indicates that the light sharing is strongly limited to a single quadrant, while in the other Qs, the sharing of scintillation light is more uniformly distributed.

Unfortunately, the mean values $\overline{f_k^j}$ of the distributions from the main pillars, i.e. the quadrant that got hit, are rather close to each other. The main distinguishing feature between the distributions for f_k for the pillars in a single quadrant is the shape of the distribution. In particular, the pillar in which the first gamma interaction occurred has a very narrow band around the mean $\overline{f_k^j}$, yet still exhibits a very long tail.

The results from the measurement data, presented in fig. 8.3b, reveals similar behaviour as in the simulations. However, the shifts of the main f_k distributions, i.e. the hit quadrant, clearly are not as pronounced as in the simulations. It indicates that the light sharing is more uniformly distributed over all the SiPM channels as opposed in the simulations. On the other hand the difference in shape between the main pillars is still present. Particularly the main pillar, i.e. the pillar above which the source was situated, shows considerable prolonged tails versus the other pillars.

By extracting the parameter sets $(\overline{f_k^j}, \sigma_k^j)$ for all pillars it is possible to directly compare the sets for simulation and experiment. In fig. 8.4 the parameter sets are plotted as a function of the channel numbers k for the top two rows of pillars.

The parameters $\overline{f_k^j}$ show a good correlation with the pillar that contained the first gamma interaction. Both the values of $\overline{f_k^j}$ and σ_k^j are consistently the largest for the main pillar. For the experimental data there is a consistent trend where the values of $\overline{f_k^j}$ and σ_k^j increase for the pillars surrounding the

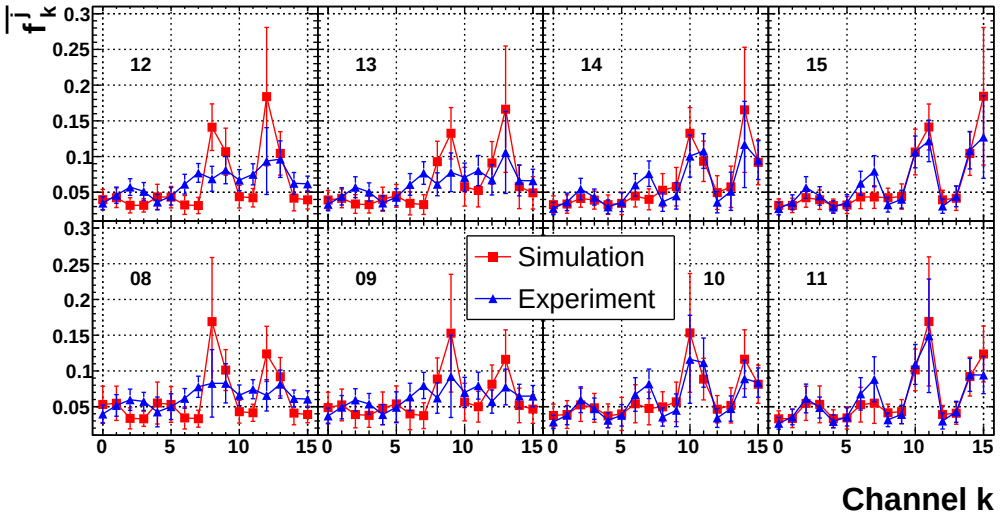

Figure 8.4: Direct comparison of the parameter sets $(\overline{f_k^j}, \sigma_k^j)$ between simulation and experimental data for one of the XY type scans (72.35 V) for the upper two rows of pillars (indices 8–15 in the figures).

main pillar. However, for the leftmost pillar, the increase is not very well pronounced, as opposed to the rightmost pillars. The most likely explanation for this effect are the larger gains of the SiPMs being situated under the rightmost pillars.

In addition to the influence of the gain on the parameter sets $(\overline{f_k^j}, \sigma_k^j)$, there is an additional effect where the values for $\overline{f_k^j}$ and σ_k^j show a minor peak at a SiPM channel which is not part of the quadrant over which the gamma source was situated. For instance, looking at the right quadrant (i.e. pillars 10, 11, 14 and 15) there is a small third peak present at SiPM channels 6 and 7 which are underneath pillars in the lower two rows of pillars. This indicates that for the PET module used during the measurements, there is more light sharing between quadrants as compared to the simulations.

DOI scans

For the DOI scan comparison, there are two different sides to the segmented crystal from where the gamma rays can come. In figs. 2.4b and 2.4c, a schematic was presented to illustrate the differences between the two directions. The PET module orientation during the measurement corresponds to the gamma rays entering the module from the *perpendicular* direction shown in fig. 8.1b. The non-identical segmentation between both directions leads to a difference in the light sharing among the SiPM channels which are correlated to the main pillar. For this reason it is necessary to compare results

Pillar IDs	Channel IDs k
12 to 15	12, 13, 14 and 15
8 to 11	8, 9, 10 and 11
4 to 7	4, 5, 6 and 7
0 to 3	0, 1, 2 and 3

Table 8.1: Mapping of DOI pillars to the channels of the SiPM array for the *perpendicular* type simulations.

from a *perpendicular* type simulation with the DOI measurement data.

In an identical manner as for the XY scans, channel fraction f_k histograms are produced for all pillars. The results are presented in fig. 8.5, again limited to the top two rows of pillars. Once again the histograms were scaled to their maximum and limited to 0.5 along the Z direction of the figure.

It is important to keep in mind how the 16 SiPM channels are related to each pillar. With the sideways type simulations and scans, the SiPM channels are not directly situated underneath the pillars anymore. Referring back to fig. 8.1b, the SiPM array is situated on the right side of the illustration (not shown in the figure).

While fig. 8.1a represents the pillar map for the XY scans, it has a one-to-one correspondence to the actual SiPM channels. Based on both illustrations and taking the crystal orientation into account, the correlations between pillars and SiPM channels can be determined. The rows of pillars in fig. 8.1b map directly to the rows of channels in fig. 8.1a. In other words, the top row of pillars correspond to the top row of channels.

In table 8.1, a listing of the pillar mapping is provided to aid the understanding of the results for the channel fraction f_k distributions. This lack of a one-to-one mapping of pillars to SiPM channel leads to the f_k distributions of the main pillar being spread out over at least four SiPM channels.

The f_k distributions of the main pillar and its neighbour have peaks at larger values of f_k for all channels correlated to these pillars. However, a split of the f_k distributions is clearly present for all the SiPM channels corresponding to these two pillars. These splits are a result of a combination of two effects: uncertainty regarding the DOI in the main pillar and scintillation light sharing towards inner pillars.

The DOI uncertainty for the gamma interaction in the main pillar results in distributions with large f_k values for all the channels associated to this pillar. For instance, a gamma interaction in pillar 15 will result in the value for f_k being largest for one of the channels associated to this pillar, i.e. in table 8.1 these channels are 12–15. After a large number of events, the

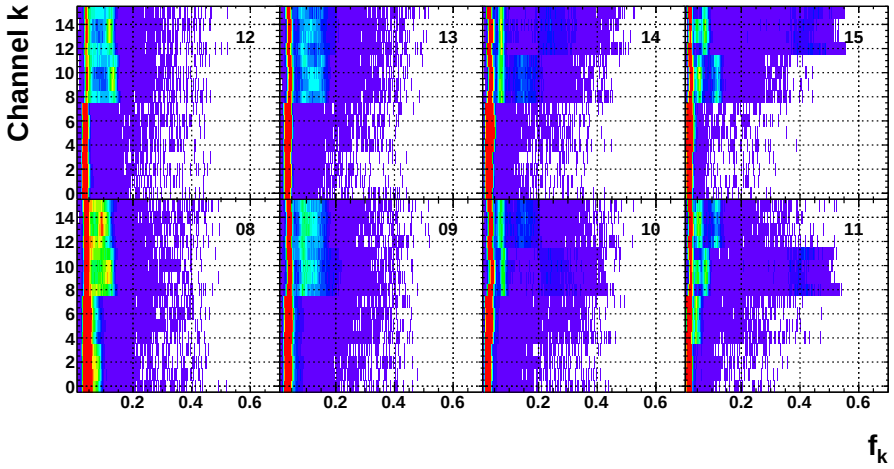

(a)

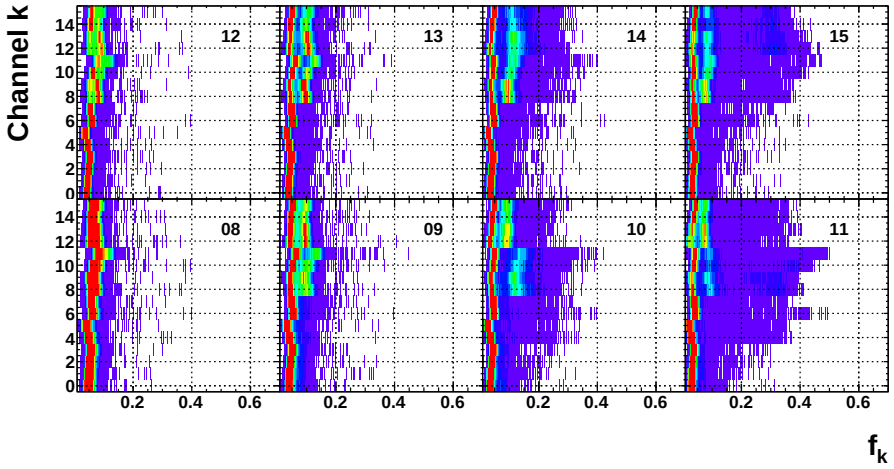

(b)

Figure 8.5: Comparison of the ADC channel fractions f_k, for the top two rows of pillars (indices 8–15), between simulations with gammas from the side and data for the DOI type scans: (a) perpendicular type simulation, (b) experimental data obtained at a bias of 72.35 V.

number of times a channel of the main pillar has the largest value f_k is determined by the attenuation length of the scintillator crystal.

The second effect arises due to the light sharing towards the inner pillars, which in turn results in increased values of f_k for the corresponding SiPMs of these inner pillars. For the pillars located closer to the SiPM array (right hand side), the light sharing is more restricted to the SiPMs associated to the main pillar. The resulting f_k distributions for these channels should thus contain larger values for f_k for all the channels in the relevant Q. This

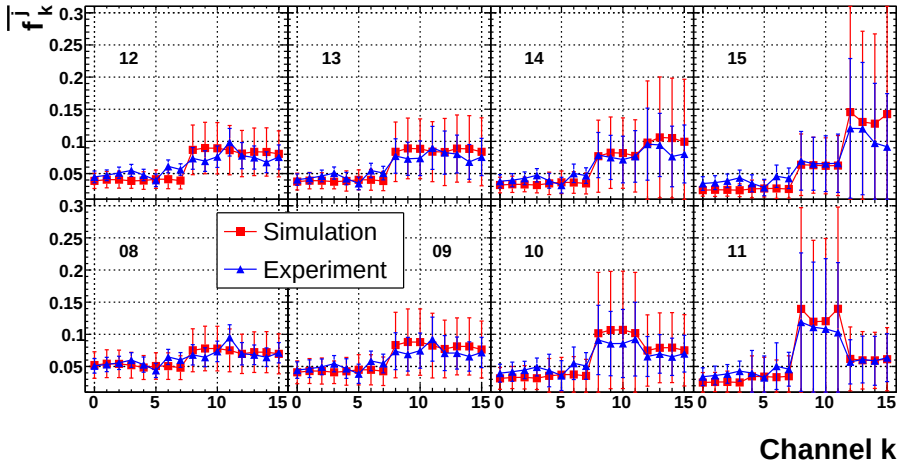

Figure 8.6: Direct comparison between the parameters sets $(\overline{f_k^j}, \sigma_k^j)$ for the simulation and the experimental data from one DOI type scan (72.35 V). Only the top two rows of pillars are presented (pillar indices 8–15).

is clearly the case as can be seen for the pillars on the right hand side. Obviously there is still a certain amount of light sharing, which is expected, towards the channels related to the neighbouring pillar.

The results for the experimental DOI scans are presented in fig. 8.5b. While the structure of these measured distributions looks similar, it is clear that they do not match perfectly. The splitting of the f_k distributions is not as pronounced as for the simulations. This is particularly apparent for the leftmost pillars, i.e. the pillars furthest from the SiPM array. It indicates that for these pillars, the light is spread more uniformly over the SiPM channels compared to the simulations.

In the results for the measured f_k distributions, the SiPM channels related to the main pillar detect large fractions of light. On the other hand, the structure of the distributions indicates that the light spread is not as much restricted to the Q associated to the main pillar. The distributions of the simulations show well defined peaks for all channels of the Qs, but they are shifted when comparing the Qs. The experimental data does not show such a clean shift between the neighbouring Qs.

In a similar way as for the XY scans, the parameter sets $(\overline{f_k^j}, \sigma_k^j)$ were extracted for comparison. In fig. 8.6 these extracted sets for the simulation are compared to sets for the experimental data. These results indicate that the parameter sets for the DOI type scans closely match each other, regardless of the more uniform light spread in the experimental data.

In both data sets, the effects of light sharing as a function of depth along the crystals can be seen. When the main pillar is situated on the front side

of the crystal, the values for $\overline{f_k^j}$ are nearly equal for all channels correlated to the main pillar and its neighbour. These pillars are situated furthest away from the SiPM array, thus it is to be expected that the fractions for those pillars are roughly equal.

Events occurring close to the SiPM array have their scintillation light more restricted to either a Q or SQ. Unfortunately, due to the nature of the side scans, the benefits of the crystal segmentation are less pronounced. As a consequence, the values for $\overline{f_k^j}$ of all channels correlated to the main pillar and its neighbour are nearly identical. Light channeling into Qs and SQs does show up for the pillars closest to the SiPM array, rightmost column in fig. 8.6.

8.1.3 χ^2 Distributions

During the reconstruction with the cube method the most likely cube, pillar for the 2D projections, is identified by selecting the cube (pillar) with the minimal χ^2 value. While performing the reconstruction, χ^2 distributions were made similarly as in previous chapters. This results in 16 χ^2 distributions per pillar. Ideally, for each pillar these χ^2 distributions should look similar for both the simulations and the measurements.

To compare these distributions, for each pillar j ($j = 0 \ldots 15$) the 16 mean values $\overline{\chi_j^2}$ of each χ^2 distribution, belonging to that pillar, were extracted. These values, for simulation and measurement, are then plotted together in a graph for the top two rows of pillars. This provides a direct comparison of the χ^2 distributions. In particular, for each pillar, the minimum values of $\overline{\chi_j^2}$ are of interest.

XY scans

The comparison graphs for the simulation data and the experimental data are presented in fig. 8.7. While the structure of the graphs for the experimental data are similar as for the simulations, the measurements consistently have lower values for $\overline{\chi_j^2}$.

Overall, the minimal values for $\overline{\chi_j^2}$ coincide with the pillars which are grouped together in the same quadrant. For instance, the two leftmost columns (i.e. pillars $j = 8$, 9, 12 and 13) should have minimal $\overline{\chi_j^2}$ at $j = 8$, 9, 12 and 13. The results do indicate that this is the case (similar for the other pillars). However, the results for the simulations can more clearly distinguish the main pillar and its Q compared to the measurements.

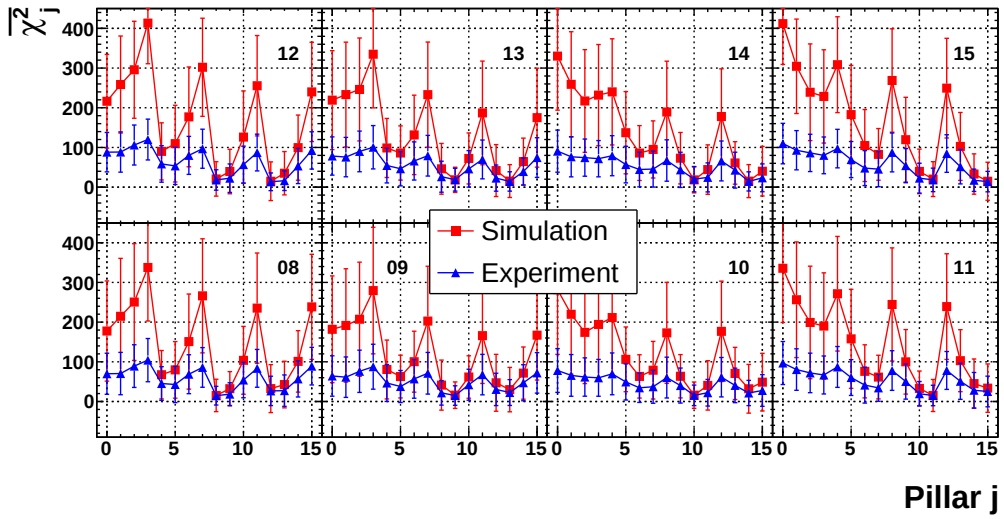

Figure 8.7: Results of the XY scans for the $\overline{\chi^2_j}$ extracted from the χ^2 distributions to compare the simulations and experimental data, for the top two rows of pillars (indices 8–15).

DOI scans

In fig. 8.8, the results for the extracted values $\overline{\chi^2_j}$ for the sideway scans and simulations reveal similar structures as well. Again the values for the measurements are consistently lower compared to those for the simulations.

Unfortunately, the sideway scans reveal that the cube reconstruction method produces very similar values over a relatively wide range of pillars. The three leftmost columns of pillars in fig. 8.8 have rather uniform values for $\overline{\chi^2_j}$ spanning over a wide range of pillars $j = 8$–15. It is only the last column of pillars which exhibit a minimal values for $\overline{\chi^2_j}$ at the expected pillar.

8.2 DOI Reconstruction

The DOI reconstruction which was introduced in section 4.3 offers an alternative to the cube reconstruction method to obtain the DOI along the segmented crystal. The method uses the following ratios,

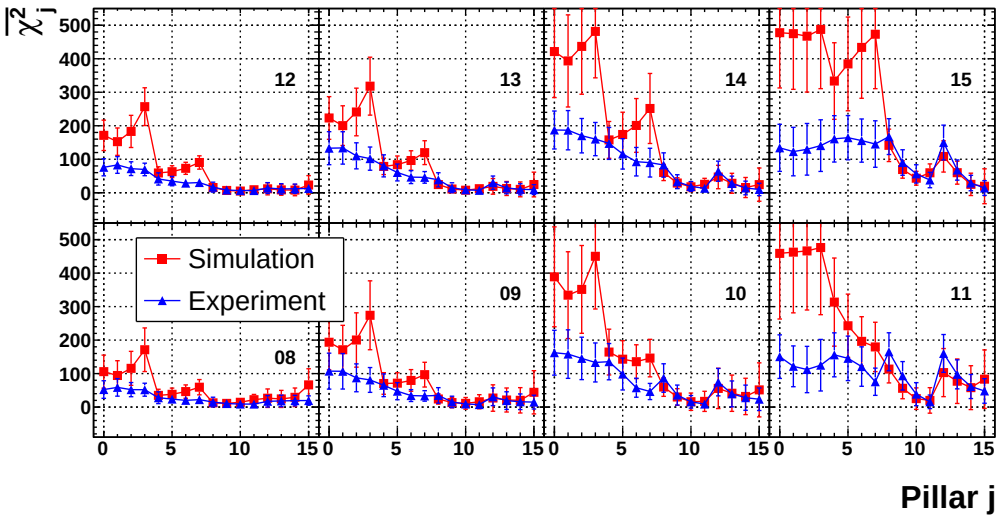

Figure 8.8: Results of the DOI scans for the $\overline{\chi^2_j}$ extracted from the χ^2 distributions to compare the simulations and experimental data. Only the results for the top two rows of pillars are shown (indices 8–15).

$$R_1 = \frac{Q_{max}}{\sum_{q \neq max} Q_q} \ , \tag{8.2}$$

$$R_2 = \frac{Q_{max}}{CH_{max}} \ , \tag{8.3}$$

$$R_3 = \frac{SQ_{max}}{SQ_{neighbour}} \ , \tag{8.4}$$

where Q_{max} (CH_{max} and SQ_{max}) are the values of the Q (CH and SQ resp.) with the maximum amount of detected scintillation light.

These ratios are calculated for each event and are subsequently filled into histograms. The measured ratio distributions are shown in fig. 8.9. The measurement data contains both the Y and Z positions of the source relative to the module. This position is assumed to be the 2D location of the gamma interaction and the Z position is used to fill the ratios into the ratio histograms. It is important to keep in mind that this does not account for multiple gamma interactions inside the scintillation crystal. Multiple gamma interactions, i.e. Compton scattering before the gamma undergoes the photo-electric effect, causes the measured location of the gamma interaction to diverge from the source location. While these measured ratio distributions have a similar structure as those from simulated data (see fig. 4.4), it is clear that they do not perfectly match.

Similarly as in section 4.3.1 and section 4.3.2, projections are made of

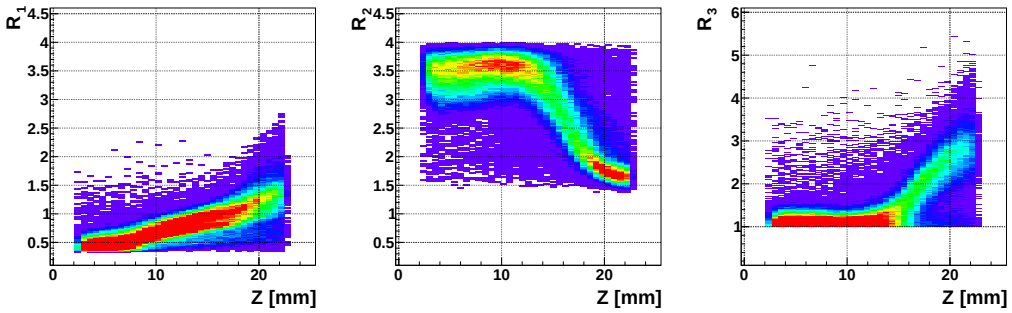

(a) **(b)** **(c)**

Figure 8.9: 2D histograms of the ratios as a function of DOI: (a) $R_1 = Q_{max}/\sum_{q \neq max}$, (b) $R_2 = Q_{max}/CH_{max}$,. (c) $R_3 = SQ_{max}/SQ_{neighbour}$.

the ratio data presented in fig. 8.9 to extract the parameters required for the χ^2 and weighted average DOI reconstruction methods. These extracted DOI reconstruction parameters from the simulated data (figs. 4.5a and 4.6a), are presented here again to directly compare those sets to those obtained from the measurements. Data for the ratio distributions of the measurements are not perfectly aligned to the front surface of the crystal. On the other hand, data for the simulations is quite well aligned to the front surface. Due to this slight misalignment between the measurement and simulation data, a minor offset (2 mm) along the depth of the crystal was applied to the measurement data.

8.2.1 Ratio χ^2

With this method, the χ^2 values for all pillars are calculated for each event according to the formula defined in eq. (9.7). The crystal is divided into equally sized slices along the length of the crystal. For each of slice p, three sets of parameters $(\overline{R_r^p}, \sigma_r^p)$ are extracted before the reconstructions stages. They are extracted from the distributions for the ratios presented in figs. 4.4 and 8.9 where $\overline{R_r^p}$ represents the mean value of R_r $(r = 1 \ldots 3)$ and σ_r^p the RMS for slice p. Then the slice with the minimal value for χ^2 is taken as the slice which most likely contained the gamma interaction.

In previous chapters extracted parameter sets were already presented separately for the simulations and measurements. Now these sets of parameters are compared directly for each ratio R_r $(r = 1 \ldots 3)$ in fig. 8.10.

From fig. 8.10a, it can be seen that R_1 follows the same pattern for both the simulations and measurements. All the R_1 parameters for the measurements do differ by a factor of ≈2 from the simulation parameters. Considering the definition for R_1, eq. (8.2), clearly during the measurements Q_{max} consistently receives a smaller fraction of the scintillation light if compared

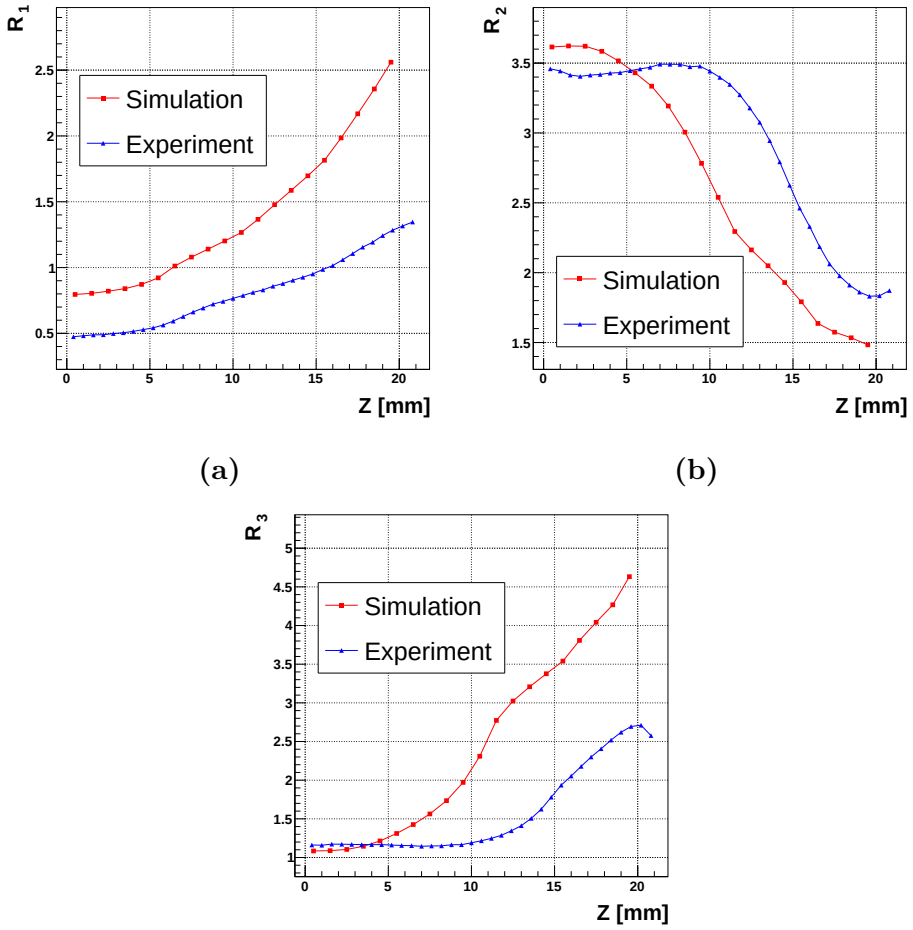

Figure 8.10: The ratios R_r $(r = 1 \ldots 3)$ as a function of depth along the crystal. Both parameters sets for simulation data and measurements are compared to each other for: (a) R_1, (b) R_2 and, (c) R_3.

to the simulations.

It clearly indicates that for the physical PET module, the scintillation light is less constricted in a single quadrant. This doesn't come as a surprise, because it can also be observed in the results for the channel fractions f_k, fig. 8.4. Those channel fractions f_k for the measurements show increased values of f_k for channels not associated to the main Q.

Both data sets follow an s-curve for the second ratio, R_2 in fig. 8.10b. While the s-curve of the parameter sets for simulation data is spread out over the full range of the crystal, the parameter sets for the measurement suffer from a rather long plateau on the front side of the crystal.

Considering the dimensions of the reflectors in between the crystal segments, it is possible to identify different sections in the graph for the sim-

ulations. At around 6 mm, the s-curve approaches a linear function which extends roughly towards 11 mm. From that point there is another linear segment that extends towards 16 mm, after which it changes into a last linear segment until the end of the crystal.

While the results for the measurements show nearly identical sections, those sections can not be related to the dimensions of the crystal sections. This mismatch, combined with previous findings, suggests that potentially the dimensions of the crystal segmentations utilised during the measurements does not conform to the design.

Similarly as for R_2, the results for R_3 in fig. 8.10c show an identical behaviour for both simulation and measurement. Here as well, the difference between both simulation and measurement seems to indicate that there is a mismatch in physical dimensions versus the design specification.

8.2.2 Weighted Average

Also the weighted average method requires parameter sets for the DOI reconstruction. Those parameter sets are extracted from the ratio distributions in a similar manner. However, now the range of ratios is divided into equal slices. For each ratio r and all slices p, a set of parameters is extracted which represent the mean position $\overline{Z_r^p}$ and the RMS σ_r^p corresponding to ratio r for that slice p.

The previously presented parameters sets are now compared to each other in fig. 8.11. Obviously the smaller values for the ratios have caused the parameter sets for the measurement to have a shorter range for the DOI reconstruction. For all the ratios, it is clear that the weighted average method has issues to correctly reconstruct the top most layer (i.e. L1).

Only the R_1 ratio has parameter sets which extend into the first layer (i.e. L1). In addition, the errors margins σ_r^p for all $\overline{Z_r^p}$ are considerable larger for the measurements as compared to simulation.

8.3 Investigating the DOI Ratio Mismatch

While the measurements with the prototype PET module show a similar behaviour as the simulation, there is a clear mismatch between the DOI ratios obtained from the simulations and the measurements. This mismatch warrants a closer investigation to find the underlying cause.

8.3.1 Reflector Dimensions

As already discussed above, an obvious suspect in the mismatch is the possibility that the crystal was not manufactured according to the specifications.

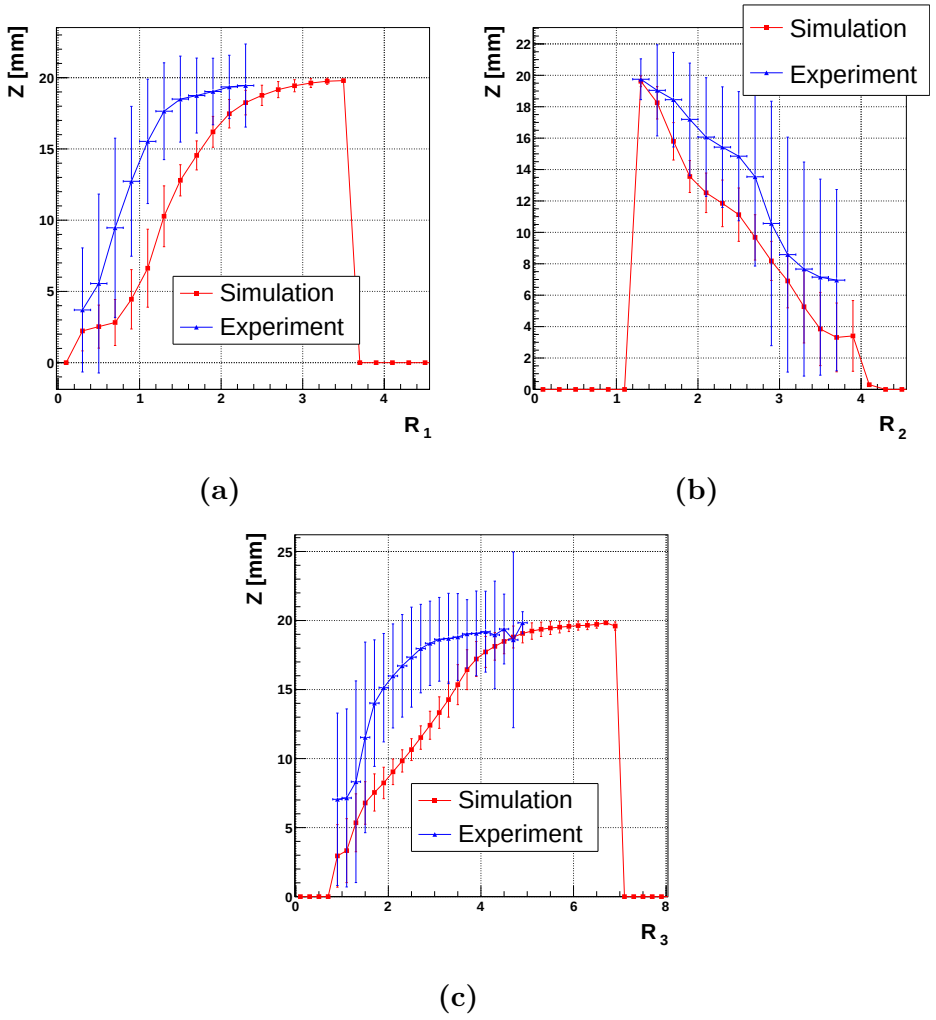

Figure 8.11: Relations of Z position and ratios for the weighted average method extracted from simulation and measurement data for: (a) R_1, (b) R_2 and, (c) R_3.

Therefore, an initial non-destructive investigation was performed to estimate the dimensions of the inner reflectors. With a simple setup consisting of a microscope to easily distinguish the reflector edges and a protractor, it was possible to get estimates for the reflector dimensions. The procedure works by aligning the outer edge of the crystal with a top edge of one inner reflector. Measuring the angle between the crystal and the table can then be used to calculate the reflector dimension along the depth of the crystal.

This procedure revealed that either one or both inner reflectors for the third and fourth layer were not machined according to the specification. Unfortunately, due to the high refractive index of LYSO, $n = 1.82$, and the dimensions of the smallest segment, the visual inspection was not sufficient, thus it was decided to remove the outer reflector from the crystal to perform

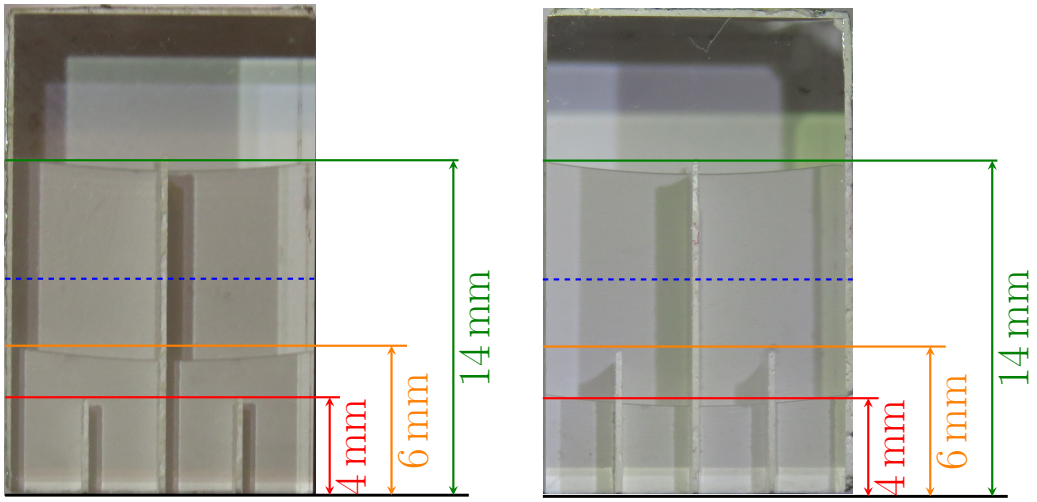

(a) **(b)**

Figure 8.12: Pictures of the segmented crystal array after removal of the outer reflective material. The inner reflector marked with a blue dashed line illustrates where the reflectors marked with orange should extend to according to the production specification.

a direct measurement of the inner reflectors.

As can be seen in fig. 8.12, the reflectors for layer 3 (L3), marked in orange, are only cut to a depth of 6 mm instead of the specified 9 mm. Another aspect which can be seen, is that none of the inner reflectors have straight edges. All reflectors have a curves edge which is a result of the method used to create the edges. These cuts for the reflectors were made with a thin wire cutting tool. Such a tool is prone to bending under the pressure applied during the making of the cuts.

8.3.2 Simulation with Updated Dimensions

New simulations were performed with the updated reflector dimension to crosscheck the DOI ratios. In the simulation software, the measured dimension were put in, although the curvature of the reflector edges was not implemented. Directions of the gammas were set to be perpendicular to the crystal according the perpendicular direction.

Extracted parameter sets for the χ^2 method are compared, fig. 8.13, to those obtained from the data of the initial simulations and the measurements. The newly obtained parameters sets, in green, are clearly closer to the measured ones, but do not fully match the experimental sets. Thus, there are still additional effects which are not accounted for in the present simulation.

For instance, the R_1 ratio is, for both the initial and the newly obtained

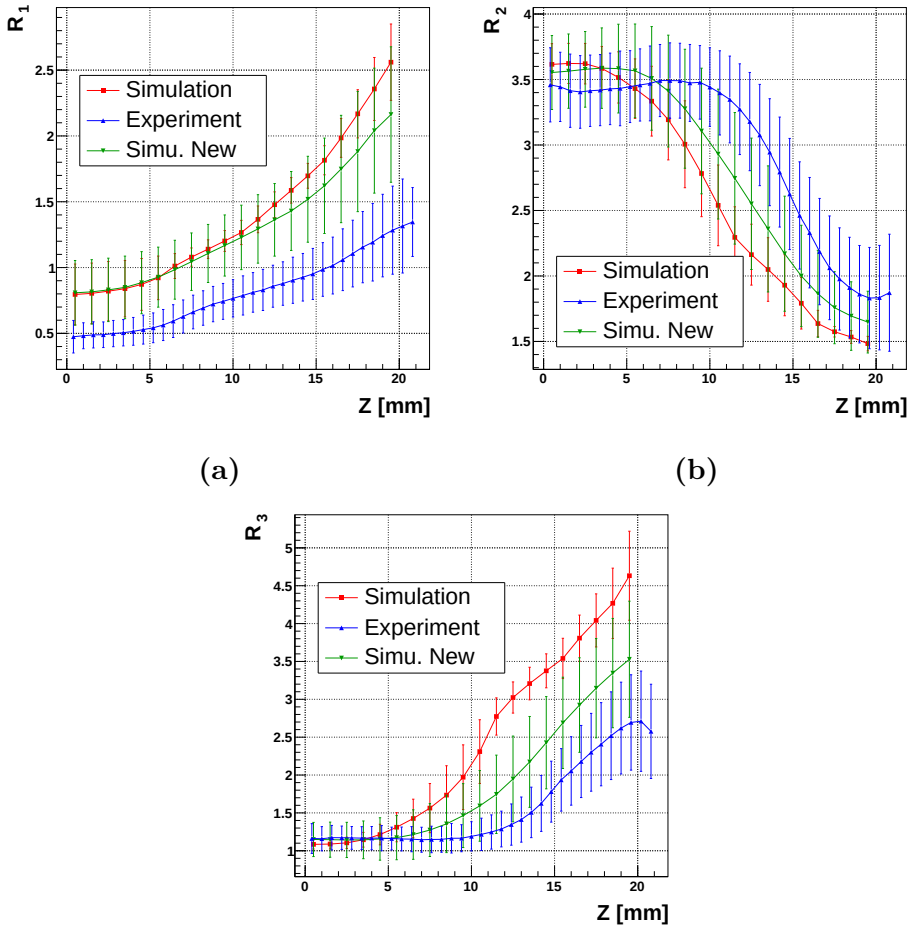

(a) **(b)**

(c)

Figure 8.13: Parameter sets for the ratios R_r ($r = 1 \ldots 3$) as a function of depth along the crystal. The newly obtained parameters sets from the updated simulation data are compared to those from the initial simulations and the measurement data: (a) R_1, (b) R_2 and, (c) R_3.

parameter sets, a factor of 2 larger, fig. 8.13a. This indicates that in the simulations, the light does not spread out over the Qs as much as this occurs under realistic conditions.

The results for the ratios R_2 and R_3 also support this conclusion. While for the top layer (L1), the light spread for all simulations and measurements agree within reasonable values, from the second layer and beyond the parameter sets start to diverge. From the parameter sets for R_2 (R_3) in fig. 8.13b (fig. 8.13c resp.), it follows that in the simulations, the light gets restricted sooner to the channels (SQs) compared to the measurements. One of the possible reasons could be that the reflectors between segments are partly transmitting light.

8.4 Summary

The results discussed above show that there is a reasonably good agreement between the reconstruction parameter sets from simulation and measurement. However, it was also illustrated that there are details of these parameter sets which are not identical. The underlying causes for these differences are partly understood as being the result of improperly machined segmented crystals. As a result of these differences, position reconstruction with the measurement data cannot at present rely on simulated parameter sets, but rather requires the use of parameter sets which are extracted from the measurement data itself.

Chapter 9

Measured Position Resolution

To finalise the proof of concept, resolutions for the position reconstruction are determined for the measurements. As discussed before, the reconstruction parameters have to be extracted from the measurement data itself. These extracted parameter sets for the XY and DOI scans were already presented in section 8.1.2 and section 8.2. With these parameter sets, the reconstruction resolutions for the X and Y directions are determined with the cube reconstruction method. The Z position resolution is determined with the cube and DOI ratios reconstruction methods.

9.1 Cube Reconstruction

Similarly as for the simulations, the cube reconstruction method is studied to determine the performance to reconstruct the gamma interaction point. For the measurements, information about the true interaction point is not available, but only the location of the source and trigger detector with respect to the module. For each event, this measurement location is used to determine the pillar above which the source is situated. The procedure how the locations of the pillars were extracted from the measurement data is described in sections 7.1.4 and 8.1.1. As a reference, the mapping of the pillars for the XY and DOI scans are provided in fig. 8.1.

9.1.1 Efficiency for X and Y Components

With the cube reconstruction method the X and Y coordinates of the gamma interaction are taken from the center of the reconstructed pillar. The efficiencies for obtaining the correct pillar along the X (Y) direction as a function of the source X (Y resp.) coordinate is determined. For each position of the source, the number of times the reconstructed pillar p and source pillar were at identical X (Y resp.) positions were counted. These counts were then normalized to the total number of events in the photopeak at the X (Y

resp.) positions, resulting in the efficiencies η for each X (Y resp.) position given by

$$\eta = \frac{N^p_{reco}(x)}{N_{\text{PPK}}(x)} \ , \tag{9.1}$$

where $N^p_{reco}(x)$ is the number of times the reconstructed pillar p was at the same X (Y resp.) location as the source pillar and $N_{\text{PPK}}(x)$ is the number of events with H within the photopeak (PPK) cutting range (i.e. $\mu_{\text{PPK}} \pm 2.355 \cdot \sigma_{\text{PPK}}$) at position x. The results for these efficiencies are presented in fig. 9.1 for both the X (left) and Y (right) directions for both the XY (top) and DOI (bottom) type scans.

From these result, the effects of light sharing between neighbouring pillars can clearly be seen. In particular, the outer pillars (columns and rows 0 and 3) have a substantial number of misidentifications of pillar. These misidentified pillars are nearly always reconstructed at the neighbouring pillar at the center of the module for both directions in the case of the XY scans and the Y direction for the DOI type scans.

For the DOI type scans, the efficiencies for the Z positions (fig. 9.1d) show a consistent reconstruction at pillar located deeper in the scintillation crystal. There is a clear preference to reconstruct the DOI position at the pillars situated in the bottom layer (near the SiPM array).

From the results in figs. 9.1a to 9.1c an estimate of the width of the gamma beam can be made. A fit with a `gaussian_cdf` (`gaussian_cdf_c`), similar as in section 3.2.4 for the Compton edge, was applied to the leading (trailing) edge of the results for the columns and rows 0 and 2 (1 and 3 resp.). From these fit results, the width is estimated to be $(0.9 \pm 0.2)\,\text{mm}$.

9.1.2 Reconstruction Resolution

To obtain a measure for the performance of the cube reconstruction, the following distances between reconstructed and source positions are defined,

$$\Delta X = X_{src} - X_p \ , \tag{9.2}$$
$$\Delta Y = Y_{src} - Y_p \ , \tag{9.3}$$
$$\Delta Z = Z_{src} - Z_p \ , \tag{9.4}$$

with X_{src} (Y_{src} and Z_{src} resp.) being the source position and X_p (Y_p and Z_p resp.) being the center of the reconstructed pillar p. Naturally for the XY (DOI resp.) scans, only data for the X and Y (Y and Z resp.) coordinates was available. For the analysis of the reconstruction resolution, no information regarding correctly or incorrectly reconstructed pillars was taken into account.

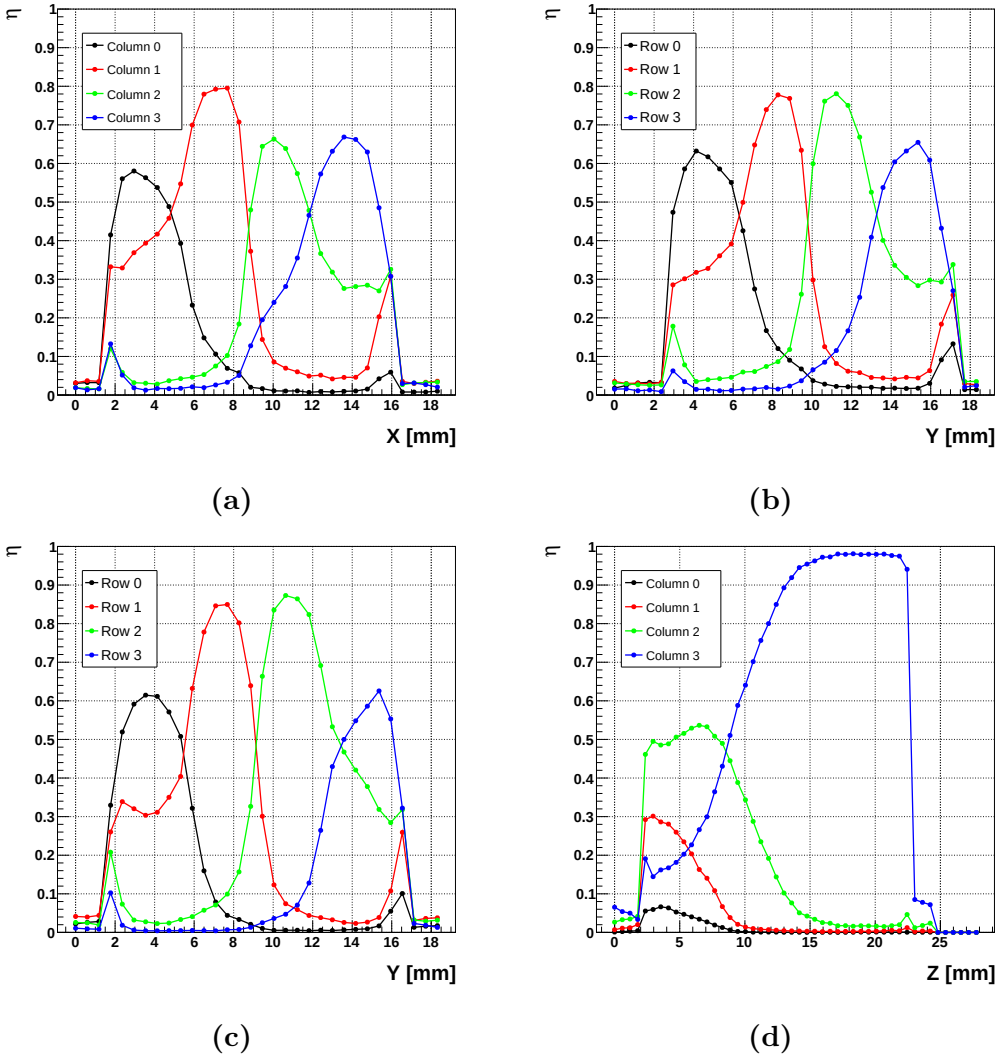

Figure 9.1: Efficiencies for the reconstruction of the column (row) index as a function of the X (Y resp.) position. From these results the width of the gamma beam was estimated as (0.9 ± 0.2) mm. Results for the XY scans are shown in the top two figures, (a) X and (a) Y direction. The bottom two rows are for the DOI scans, with (c) the Y and (d) the Z directions.

From fig. 9.2 a resolution for the reconstruction of the interaction point in the plane of the SiPM array can be determined. The difference between the ΔX and ΔY distributions in fig. 9.2 originates from the asymmetry in segmentation of the third layer for both directions. Fortunately, the difference in reconstruction resolution between both directions is negligible. A resolution of $\approx$3.5 mm at FWHM is obtained for both directions, which corresponds to the channel pitch.

The result for the resolution of the position reconstruction can be used

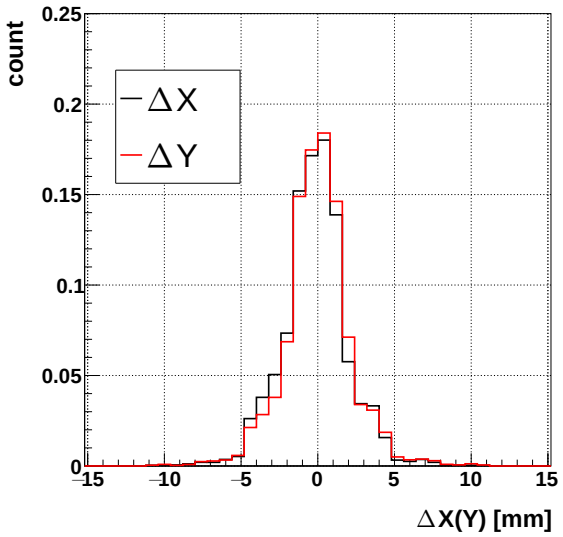

Figure 9.2: Distance between the position of the source and the center of the reconstructed pillar for an XY scan.

to get an estimate of the beam width of the source. In section 4.2.1 the resolution for the PET module, as a consequence of the discrete nature of the SiPM array, was estimated at 0.92 mm. Combining this discrete resolution (σ_{disc}) and the obtained resolution (σ_x) from the measurement data as follows

$$\sigma_{disc} = \frac{3.2\,\text{mm}}{\sqrt{12}} \qquad \& \qquad \sigma_x = \frac{3.5\,\text{mm}}{2.355}\ , \tag{9.5}$$

$$\sigma_{src} = \sqrt{(\sigma_x)^2 - (\sigma_{disc})^2}\ , \tag{9.6}$$

yields a beam width for the source (σ_{src}) of ≈1.4 mm which is consistent with the result obtained in section 9.1.1.

9.2 DOI Reconstruction

The distributions for the DOI ratios were presented for the measurement data, in section 8.2. From these distributions, parameter sets for both the χ^2 and weighted average methods were extracted and compared to similar sets obtained from simulation data. The differences between both sets resulted in the necessity to rely on the measured parameter sets to perform the DOI reconstruction with measurement data.

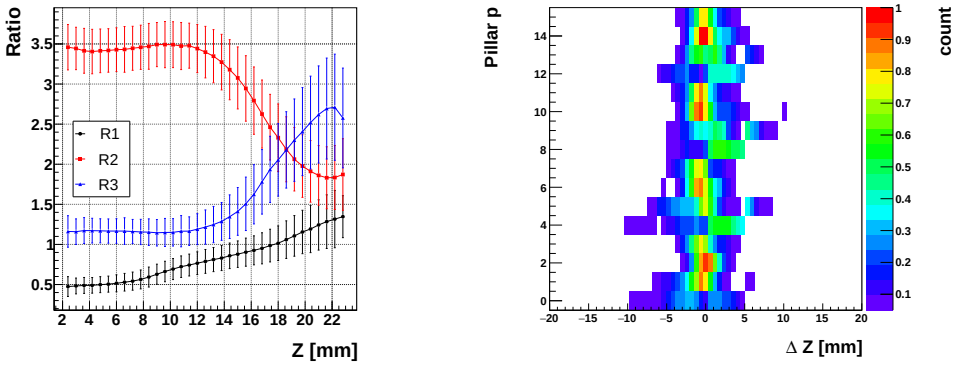

(a) (b)

Figure 9.3: Ratio projections for the χ^2 method: (a) projections of the DOI ratios data, (b) distance between the source location and the center of the reconstructed pillar.

Ratio χ^2

The χ^2 reconstruction method uses parameters sets which were extracted from the projections onto the Y axis of the data shown in fig. 8.9. For each position index p, the mean $\overline{R_r^p}$ and RMS σ_r^p values for the ratios $r = 1 \ldots 3$ are extracted from the projections. Results for these parameters are presented in fig. 9.3a.

During χ^2 reconstruction of the DOI, a χ_p^2 value is calculated for each position index p and ratio r, defined as

$$\chi_p^2 = \sum_{r=1}^{3} \left(\frac{R_r - \overline{R_r^p}}{\sigma_r^p} \right) \ . \tag{9.7}$$

The minimal value of all the χ_p^2 is chosen as the position index p where the gamma interaction occurred along the depth of the crystal.

Figure 9.3b presents the distance between the reconstructed DOI and the location of the source. The distance ΔZ, originally defined in eq. (9.4), is adjusted to account for the finer divisions of the DOI position slices compared to the pillars in the cube reconstruction.

$$\Delta Z = Z_{src} - Z_p \ , \tag{9.8}$$

where Z_p now represents the center of the position slice for the reconstructed position index p.

These distance distributions were separated as a function of the pillar above which the source was located. It provides an insight of the performance

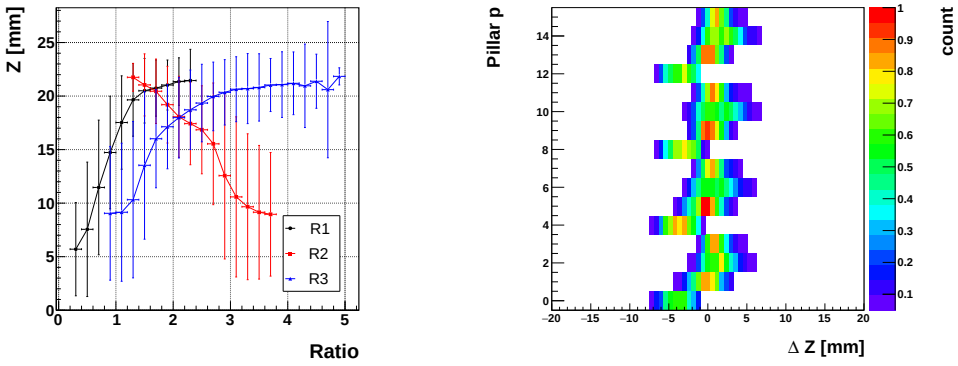

(a) **(b)**

Figure 9.4: Ratio projections for the weighted average method: (a) projections of the DOI ratios data, (b) distance between the source location and the center of the reconstructed pillar.

of the χ^2 reconstruction method, based on the location of the source. Overall, the distance distributions are centered around zero and mostly contained within a full layer depth (5 mm). Note that in the upper layer (pillars $0, 4, 8$ and 12, see fig. 8.1b) there is a tendency to reconstruct the DOI at a more shallow depth (towards the crystal entry face).

Weighted Average

The weighted average method extracts parameters from the projections of fig. 8.9 onto the X axis. Each bin projection onto the X axis is then used to extract the mean $\overline{Z_r^p}$ and RMS σ_r^p values for the DOI position. Results for the extraction of these parameters are shown in fig. 9.4a.

These parameters are then used to reconstruct the DOI location by calculating a Z_γ defined as

$$Z_\gamma = \frac{\sum_{r=1}^{3} \frac{\overline{Z_r^p}}{(\sigma_r^p)^2}}{\sum_{r=1}^{3} \left(\frac{1}{\sigma_r^p}\right)^2} \; . \tag{9.9}$$

For each PET event, Z_γ is calculated which is taken as the reconstructed DOI. Similarly as for the χ^2 method, the performance of the weighted average method was studied for each pillar by calculating the distance ΔZ,

$$\Delta Z = Z_{src} - Z_\gamma \; . \tag{9.10}$$

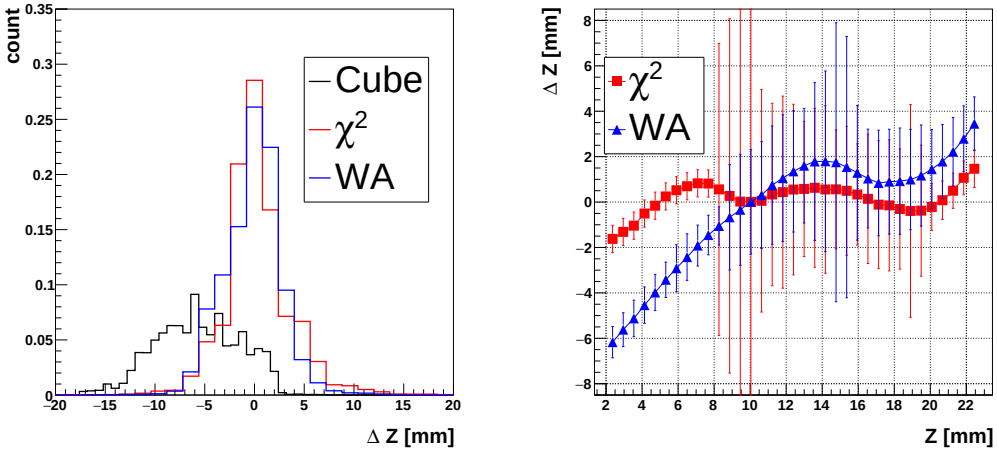

(a) **(b)**

Figure 9.5: Reconstruction resolution ΔZ for the ratio based reconstruction methods: (a) combined result for all the Z positions of the source, and (b) mean and FWHM values for ΔZ as a function of the Z position of the source.

The result is presented in fig. 9.4b where ΔZ is shown as a function of the pillar p above which the source was located.

From fig. 9.4b it is clear that the weighted average method has an issue with reconstructing the DOI location. In particular interactions in the top layer tend to be reconstructed at deeper locations in the scintillation crystal.

9.2.1 Reconstruction Resolution

Performance of the DOI reconstruction is estimated based on the distance between the source location and the reconstructed depth of interaction. A comparison is made between the various methods discussed above.

For each method we study $\Delta Z = Z_{src} - Z_{reco}$, with Z_{src} the position of the source relative to the PET module and Z_{reco} the reconstructed DOI, as described in the sections relating to the various methods. A DOI reconstruction is performed for each event using each of the three methods (cube, χ^2 and weighted average).

Both the χ^2 and weighted average method show promising results, with resolutions of 4.1 mm and 4.9 mm at FWHM. From the results for the three methods in fig. 9.5, it can be concluded that the cube reconstruction has a worse resolution of 11.6 mm at FWHM. In addition, it consistently reconstructs the DOI in deeper layers (negative ΔZ).

Similarly as for the slice reconstruction in sections 4.3.3 and 5.3.1, histograms for each Z position were produced containing the values for ΔZ. From these histograms, mean and FWHM values were extracted and are

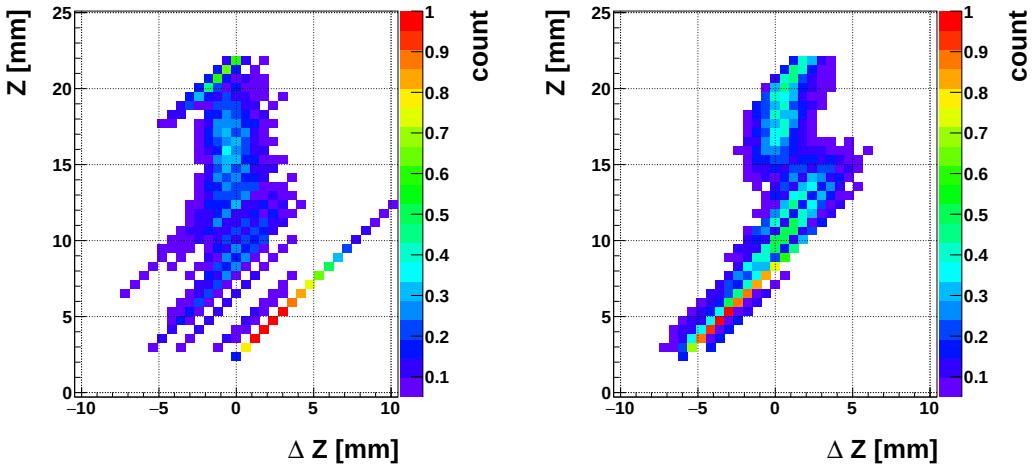

(a) (b)

Figure 9.6: Data for the values of ΔZ as a functions of the Z position of the source. From these results one can see that both methods consistently reconstruct the Z position at incorrect depths. A minor zero suppression of 5 % was applied to illustrate the narrow distributions for ΔZ in the top layer (L1). (a) χ^2 method, (b) weighted average method.

presented in fig. 9.5b. These results follow a similar pattern as the results from simulation. The notable exceptions are the FWHM values for Z positions in the first layer and the first half of the second layer ($Z < 8$).

To understand why the FWHM values for interactions in fig. 9.5b are so small, the histograms from which the mean and FWHM values were extracted are presented in fig. 9.6. One can see that both methods fail to correctly reconstruct the DOI for interactions occurring in the top layer (L1). As a consequence, both methods have very narrow distributions for ΔZ resulting in the small values for the FWHM. A small zero suppression (set to 5 %) was applied to the histograms in fig. 9.6 to illustrate these narrow distributions.

9.3 Summary

The obtained resolutions for the measurement data are in reasonable agreement with the results from the simulations. A resolution for the X and Y positions of 3.5 mm is obtained with the cube reconstruction. With the χ^2 DOI reconstruction method a resolution of 4.1 mm is achieved. The weighted average method achieves a resolution of 4.9 mm.

It was also demonstrated that the distributions for ΔZ follow an the same pattern as with the simulations. Unfortunately, the mismatch in the specified and real reflector dimensions have resulted in a degraded performance of the

DOI reconstruction methods. Regardless, it is expected that these results can be improved with a correctly machined crystal structure.

Chapter 10

Conclusion

In this work, a crystal segmentation was proposed to add a depth of interaction (DOI) encoding to the scintillation crystal of a PET module. Three methods were developed to reconstruct the interaction point of annihilation gammas inside the scintillator crystal. All the developed reconstruction methods rely on predetermined sets of parameters which are correlated to the light distribution over the channels of an array of photodetectors (SiPM array). As a consequence of the crystal segmentation, the distribution of the scintillation light depends on the location of the interaction point in the scintillator crystal. Through the use of Monte Carlo simulations the performance of the reconstruction methods was studied while taking into account how the parameter sets were obtained, i.e. single point of photon emission, first gamma interaction, or the energy weighted position.

These simulations demonstrated that an XY position resolution of 3.1 mm (FWHM) is achieved. This result is comparable to the resolution which can be obtained with a non-DOI encoded crystal array. In addition, the results indicate that the reconstruction of the XY position is minimally influenced by the choice of the parameter sets for the cube reconstruction.

On the other hand, the resolution along the depth of the crystal was shown to depend on the used reconstruction method and the choice of parameter sets. With the ratios based reconstruction methods, the best case DOI reconstruction resulted in an improved resolution of 2.3 mm (χ^2 method) and 2.5 mm (WA). This best case reconstruction was obtained for gamma rays while using the parameter sets obtained from simulation data with the ideal single point photon emission.

The quality of PET imaging is strongly correlated to the resolution in the tube of response (TOR). Therefore, simulations were used to study the performance of the module, in terms of the TOR, by varying the angle between the annihilation gamma rays and the normal of the entry surface. This study provides an estimate of the field of view (FOV) which can be achieved with this crystal design. The maximum angle of 30° roughly corresponds to an-

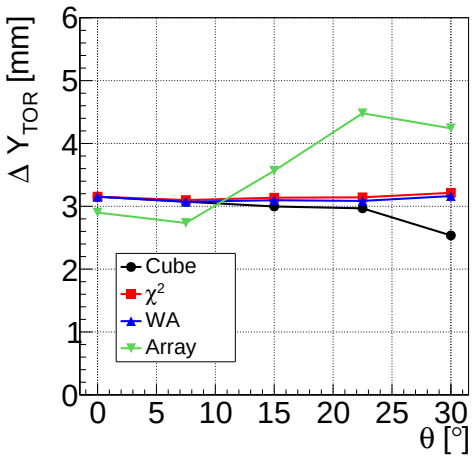

Figure 10.1: Comparison of the resolution for the TOR reconstruction with the proposed crystal segmentation versus a more traditional crystal structure.

nihilation gamma rays originating from points at halfway the center and the outer edge of a PET scanner ($d/r = sin(\theta)$). It was shown that the resolution for the TOR remains constant, at around ≈3.2 mm, over this range. In contrast, it was demonstrated that with a more traditional crystal array the resolution suffers from a deteriorated TOR resolution for locations outside the central region of a scanner.

The TOR resolutions for the proposed segmentation versus a more traditional crystal are compared to each other in fig. 10.1. While the proposed crystal structure has a similar performance in the central part of the scanner, i.e. θ <10°, a clear improvement can be observed for positions outside the central region of the scanner.

To provide a proof of concept, measurements with a prototype PET module were performed and the results were compared with those from simulation. Despite a mismatch in the dimensions of the segmentations between simulation and the prototype crystal, there is a reasonable agreement in the behaviour of the reconstruction parameter sets. Resolutions for the X and Y positions were shown to be 3.5 mm for both directions. The obtained resolutions for the Z position were 4.1 mm for the χ^2 method and 4.9 mm for the weighted average method.

During the measurements, the module positions relative to the source were of a discrete nature. From the simulation data, slice reconstructions were performed for the ratios based DOI reconstructions, providing a Z position reconstruction of a similar discrete nature. Both in simulation and measurement, parameter sets were obtained relative to the first gamma interaction points. With these parameter sets and for the χ^2 method, the obtained resolutions ΔZ are 3.8 mm (simulation) and 4.1 mm (measurement). Resolutions of 4.3 mm (simulation) and 4.9 mm (measurement) are achieved

for the weighted average method. Considering the mismatch between the geometry of the prototype and simulated crystals, these results are in good agreement with each other. It is expected that with the correct dimensions for the segmentations, an even closer match would be obtained.

There are several possible ways how to further improve the methods discussed in this thesis. In addition to an optimization of the segmentation scheme and reconstruction algorithms, one could also turn the module around, and thus profit from the fact that the best resolution is achieved for gamma rays converting in the most segmented layer.

Chapter 11

Povzetek

11.1 Pozitronska tomografija

Pozitronska tomografija (PET) je neinvazivna metoda medicinskega slikanja za in vivo slikanje živega tkiva. Omogoča tridimenzionalno slikanje, ki se lahko uporablja za spremljanje fizioloških procesov v telesu. Pri tej vrsti slikanja v pacienta vbrizgamo radioaktiven izotop β^+, najpogosteje ^{18}F kot sestavni del florodeoksiglukoze (FDG). Radioaktivni flor pri razpadu odda pozitron, ki se na razdalji tipično enega milimetra znotraj tkiva anihilira z elektronom, pri tem pa nastaneta dva kolinearna žarka gama z energijo 511 keV. Detekcija obeh žarkov gama določa premico v pacienti, na kateri leži izvor žarkov gama, iz velike množice takih premic pa lahko rekonstruiramo porazdelitev izvorov v telesu [1, 2].

Te anihilacijske žarke gama žarki običajno detektiramo posredno preko t.i. gama kamere. Tipično gama kamere za PET slikanje sestavljajo anorganski kristal, v katerem se gama žarka pretvorita v scintilacijsko svetlobo, in senzor svetlobe, običajno fotopomnoževalka, v katerem se svetloba pretvori v električni impulz. Eden ali več obročev takih gama kamer zložimo okoli pacienta.

Medtem ko je kakovost obstoječih naprav za PET slikanje že zelo dobra, je še vedno precej možnosti za izboljšave, predvsem pri izboljšanju razmerja signal/šum, ki bi omogočil zmanjšanje doze, ki jo pri preiskavi prejme pacient. Obstoječe aparature za pozitronsko tomografijo trpijo zaradi tako imenovanega paralaksne napake. Ta napaka izhaja iz pomanjkanje podrobnih informacij o točki absorpcije žarka gama v scintilacijskem kristalu.

11.1.1 Napaka zaradi paralakse

Večina gama kamer lahko mesto interakcije žarka gama z detektorjem rekonstruira samo v dveh dimenzijah, to je v ravnini, ki jo določa detektor. V primeru žarkov gama, ki v detektor priletijo pravokotno na to ravnino, to

običajno ne predstavlja težav (slika 11.1.). Pri slikanju razsežnega objekta, kot je to pacient, pa je radioaktivna snov porazdeljena bolj ali manj po celotni notranjosti obroča. V gama kameri zato pogosto zaznavamo tudi žarke gama, ki vanjo vstopajo pod velikim kotom glede na normalo na kristal kot je razvidno iz slike 11.1.

Žarki gama, ki priletijo v scintilacijskega kristal, se bodo v njem absorbirali na poljubni globini; verjetnost za interakcijo v dani globini je podana z eksponentno porazdelitvijo, povprečna globina pa je določena z absorpcijsko dolžino. Običajne gama kamere ne morejo izmeriti te razdalje, ki je poznana kot globina interakcije (DOI). Kot je razvidno iz slike 11.1, moramo pri taki kameri pri rekonstrukciji položaja izvora za žarke daleč od sredine detektorja dopustiti močno razširjeno linijo odziva (sivo šifrirano področje), kar privede do t.i. paralaksne napake. Slika 11.1 tudi ponazarja, kako bi lahko ta problem rešili s kristalom, ki bi omogočal vsaj grobo merjenje globine interakcije.

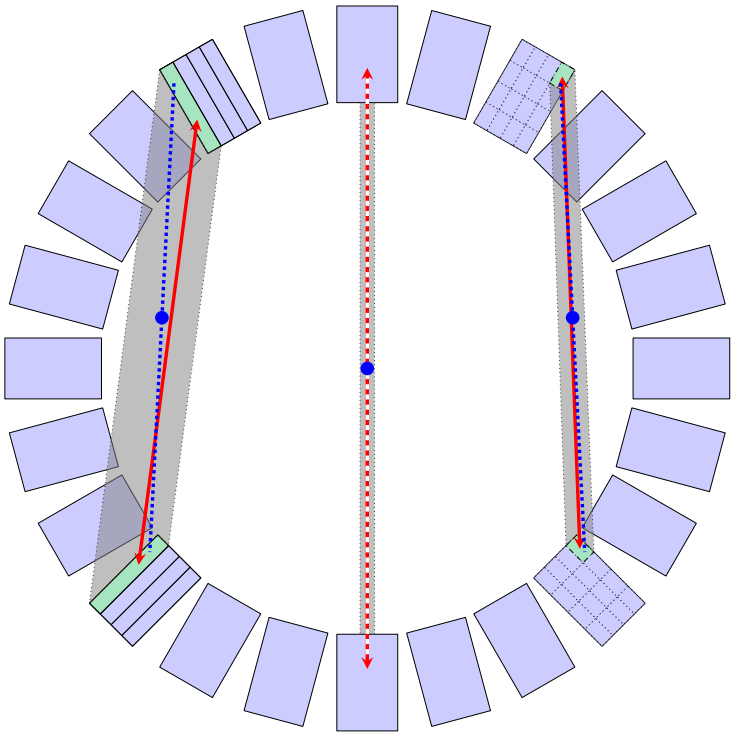

Slika 11.1: Shematski prikaz paralaksne napake zaradi nepoznavanja globine interakcije (DOI). Modra pika in modre črte prikazujejo pravo pot žarkov gama. Rekonstruirana linija odziva (LOR) je označena z rdečo črto. Na desni strani slike je prikazano, kako je mogoče zmanjšati paralaksno napako če uporabimo detektor s segmentacijo v treh dimenzijah.

11.2 Scintilator s kodirano informacijo o globini interakcije

V pričujočem doktorskem delu sem razvil in preučeval novo vrsto detektorskega modula s segmentiranim kristalom in s silicijevo fotopomnoževalko kot senzorjem scintilacijske svetlobe. Princip delovanja modula temelji na določanju globine interakcije preko porazdelitve svetlobe na svetlobnih senzorjih. Oblika porazdelitve svetlobe na senzorjih je zaradi globinsko odvisne segmentacije določena z mestom, v katerem je žarek gama interagiral.

DOI kodiran scintilacijski kristal, kot sem ga razvil v tem delu, je sestavljen iz monolitnega bloka, kristala LYSO. Kristal ima štiri različne plasti (slika 11.2):

- L1: vrhnja plast debeline 6 mm ni segmentirana
- L2: drugi sloj je sestavljen iz 2x2 enako velikih kvadrantov (Q), debelina te plasti je 5 mm.
- L3: V tretji, 5 mm debeli plasti je vsak od kvadrantov razdeljen na pol (subkvadrant, SQ).
- L4: Četrti in zadnji sloj ima 4x4 segmentacijo in je debel 4 mm. Spodnja stran te plasti je izstopna ploskev in je spojena matriko SiPM senzorjev.

11.3 Rekonstrukcijske metode

Za tridimenzionalno rekonstrukcijo točke interakcije žarka gama potrebujemo metodo, ki bo iz velikosti signala na šestnajstih senzorjih (ki je odvisen od števila zaznanih scintilacijskih fotonov) omogočila sklepanje na tri koordinate mesta interakcije. Za segmentiran kristal sem v okviru svoje raziskave razvil tri metode.

11.3.1 Rekonstrukcija kocke

Kristal je razdeljen na 64 enako velikih kock, ravnina svetlobnega senzorja je razdeljena na 16 enako velikih polj. Za vsako kocko j smo s simulacijo določili dva kompleta 16 parametrov, povprečno velikost signala v posameznem kanalu senzorja k, normiran na vsoto vseh signalov,

$$f_k = \frac{h_k}{\sum_{c=0}^{15} h_c} \ , \tag{11.1}$$

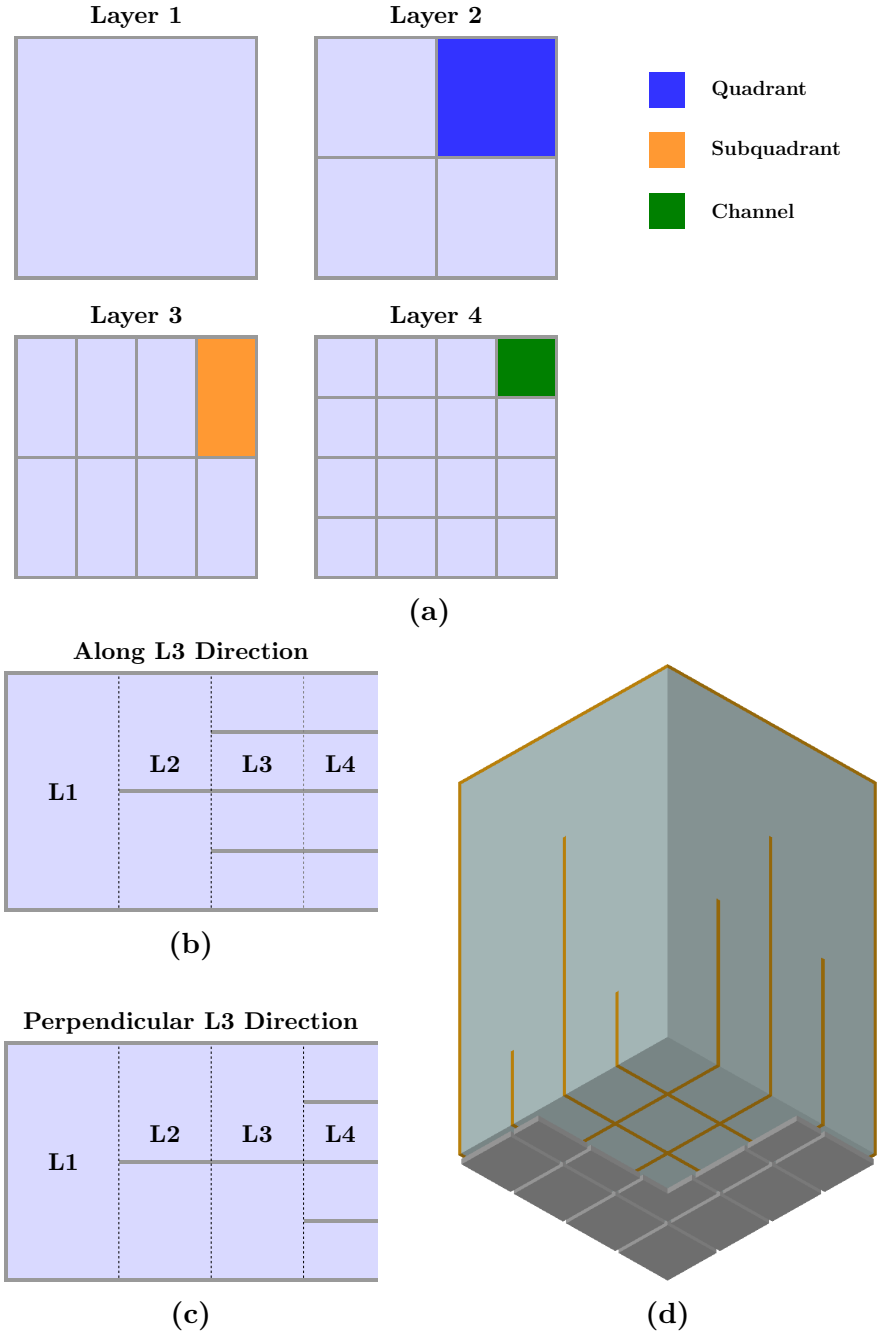

Slika 11.2: Segmentacija za štiri različne plasti: (a) tloris štirih plasti, (b) in (c) stranska pogleda, (d) 3D model segmentiranega kristala za PET modul.

in širino porazdelitve velikosti signalov v tem kanalu; s h smo označili velikost signala z odštetim pedestalom.

Pri rekonstrukciji uporabimo te parametre za določanje vrednosti χ^2,

$$\chi^2_j = \sum_{k=0}^{15} \left(\frac{f_k - \overline{f_k^j}}{\sigma_k^j} \right)^2 , \tag{11.2}$$

ki jo izračunamo za vsako kocko. Kot rekonstruirano kocko izberemo tisto, pri kateri je vrednost χ^2 najmanjša.

11.3.2 Rekonstrukcija DOI

Pri dekodiranju DOI uporabimo tri različna razmerja kanalov signalov SiPM. Po tem, ko izračunamo vsoto kanalov za posamezen kvadrant (Q_q) in subkvadrant (SQ_s), določimo še kanal z najvišjim signalom (CH_{max}), kvadrant z najvišjim signalom (Q_{max}), in subkvadrant z najvišjim signalom (SQ_{max}), lahko izračunamo naslednja razmerja

$$R_1 = \frac{Q_{max}}{\sum_{q \neq max} Q_q} , \tag{11.3}$$

$$R_2 = \frac{Q_{max}}{CH_{max}} , \tag{11.4}$$

$$R_3 = \frac{SQ_{max}}{SQ_{neighbour}} . \tag{11.5}$$

kjer je $SQ_{neighbour}$ vsota signalov subkvadrantu, sosedu subkvadranta z najvišjo vsoto.

Razmerje χ^2

Pri tej metodi razdelimo globino kristala v enako debele rezine. Za vsako rezino p določimo iz simuliranih podatkov povprečje razmerij podanih v enačbah 11.3-11.5 ($\overline{R_r^p}$) in širino porazdelitve razmerja za to rezino (σ_r^p). Slika 11.3a prikazujo za vsako od teh treh razmerij odvisnost od globine (oziroma indeksa rezine).

Pri rekonstrukciji za vsako rezino izračunamo vrednost χ^2_p,

$$\chi^2_p = \sum_{r=1}^{3} \left(\frac{R_r - \overline{R_r^p}}{\sigma_r^p} \right)^2 , \tag{11.6}$$

In kot rekonstruirano globino interakcije izberemo položaj rezine z najmanjšim χ^2.

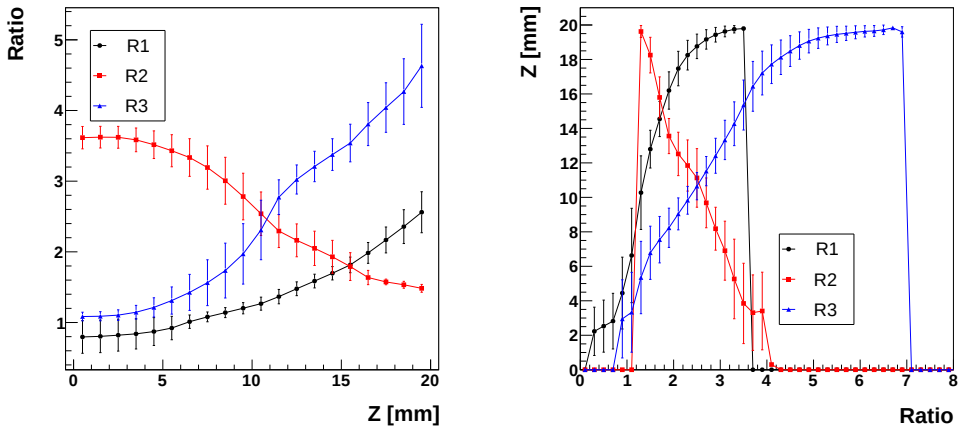

(a) **(b)**

Slika 11.3: Povzeto vrednosti za srednje razmerje $\overline{R_r^p}$ z RMS σ_r^p (bari napak): (a) χ^2 metoda, (b) tehtano povprečje metoda.

DOI z obteženim povprečjem

Pri tej metodi razdelimo na rezine razmerja 11.3-11.5, vsaki rezini p v razmerju r pa na podlagi simuliranih podatkov pripišemo povprečen Z ($\overline{Z_r^p}$) in širino porazdelitvepo Z za dano rezino v R (σ_r^p). Globino interakcije nato ocenimo iz

$$Z_\gamma = \frac{\sum_{r=1}^{3} \frac{\overline{Z_r^p}}{(\sigma_r^p)^2}}{\sum_{r=1}^{3} \left(\frac{1}{\sigma_r^p}\right)^2} \,. \tag{11.7}$$

11.4 Ločljivost pri rekonstrukciji

Ločljivost rekonstruiranih koordinat točke interakcije smo najprej preučevali z Monte Carlo simulacijo. Primerjali smo ločljivost pri posameznih rekonstrukcijskih metodah, in za dve različni segmentaciji kristala. Kot zaključni test metode smo konstruirali prototip detektorja PET in z njim izvedli meritve resolucije.

11.4.1 Rezultati za simulirane podatke

Z Monte Carlo simulacijo smo proučevali natančnost rekonstrukcije pri treh različnih predpostavkah za vrednosti parametrov rekonstrukcije: izsevanje

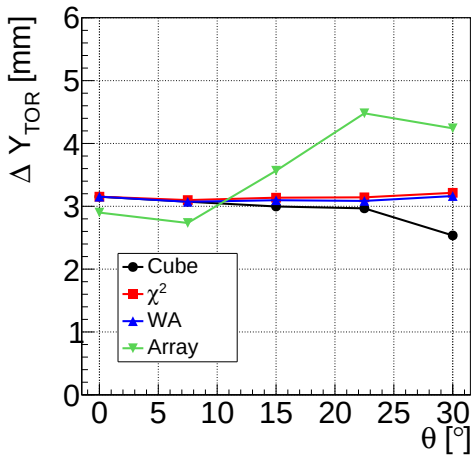

Slika 11.4: Primerjava resolucije za tube-of-response (TOR) za različne metode rekonstrukcije in za tradicionalno segmentiran signal (označen kot 'Array', s segmentacijo samo v ravnini detektorja X,Y).

vseh scintilacijskih fotonov v eni točki, glede na prvo interakcijo žarka gama in energijsko obteženo mesto interakcij žarka gama. Te simulacijske študije so pokazale, da je resolucija položaja interakcije v ravnini detektorja (X,Y) enaka 3,1 mm (FWHM, širina na polovični višini). Takšna resolucija je primerljiva z vrednostjo, ki jo dobimo s kristalom brez DOI kodiranja. Rezultati simulacijskih študij kažejo tudi na to, da je resolucija neodvisna od konkretne izbire parametrov rekonstrukcije (izsevanje vseh scintilacijskih fotonov v eni točki, glede na prvo interakcijo žarka gama ali energijsko obteženo mesto interakcij žarka gama).

Po drugi strani pa se je izkazalo, da je resolucija v globini mesta interakcije (koordinata Z) odvisna od uporabljene rekonstrukcijske metode in izbire parametrov. Najboljšo natančnost dobimo pri rekonstrukcijo, ki temelji na uporabi razmerij, in sicer 2,3 mm za metodo χ^2 in 2,5 mm za metodo WA. Ta najboljša natančnost je bila dobljena s parametri, ki so temeljila na predpostavki, da se vsi fotoni izsevajo iz iste točke.

Kakovost slikanja pri pozitronski tomografiji je tesno povezana z resolucijo v t.i. tube-of-response, TOR (slika 11.1), torej s prečno dimenzijo telesa, ki ga določata kristala, v katerih smo zaznali žarka gama. Zato smo simulirali odziv detektorja in študirali rekonstrukcijo za različne kote vpadnih žarkov glede na ravnino detektorja. Ta študija je pokazala, da je ločljivost – širina TOR – v našem globinsko segmentiranem kristalu do kota 30 stopinj konstantna, medtem ko za tradicionalno segmentiran kristal raste od 10 stopinj dalje (slika 11.4).

11.4.2 Rezultati za izmerjene podatke

Kot dokončni dokaz delovanja koncepta smo izvedli meritve s prototipom PET modula s segmentiranim kristalom. Pri meritvam smo uporabili močno kolimiran snop žarkov gama iz izvora ^{22}Na. Rezultati meritev so se zadovoljivo ujemali rezultati simulacije. Resolucija v meritvi prečnih koordinat X in Y je bila 3,5 mm. V smeri Z je resolucija 4,1 mm za metodo χ^2, in 4,9 mm za obteženo povprečje. Najpomembnejši razlog za nepopolno ujemanje s simulacijo je segmentacija kristala, za katero smo ob zaključku dela z destruktivnim pregledom ugotovili, da je bila drugačna, kot so bile proizvodne specifikacije, in seveda drugačna kot v simulaciji.

11.5 Zaključek

Metoda, ki sem jo razvil v pričujočem delu, predstavlja obetavno rešitev problema meritve globine interakcije pri detekciji anihilacijskih žarkov gama. Izkorišča dobre lastnosti silicijeve fotopomnoževalke, novega tipa svetlobnega senzorja, in možnosti, ki jo ponuja globinska segmentacija scintilacijskega kristala. Obstaja več možnih načinov, kako dodatno izboljšati metode obravnavane v tem delu. Poleg možnosti, ki jih ponuja optimizacija segmentacije in rekonstrukcijskih algoritmov, bi lahko detektorski modul obrnili v nasprotno smer in tako izkoristili dejstvo, da je najboljša resolucija za žarke gama, ki interagirajo v najbolj segmentirani plasti.

Bibliography

[1] D L Bailey et al. *Positron emission tomography: basic sciences*. Berlin: Springer, 2003.

[2] Mario Quarantelli and Anna Prinster. *PET: physics, instrumentation and scanners*. English. Ed. by Michael E. Phelps. Vol. 34. 5. Springer-Verlag, 2007, pp. 799–799. DOI: 10.1007/s00259-006-0353-6. URL: http://dx.doi.org/10.1007/s00259-006-0353-6.

[3] R. Vinke et al. "Time walk correction for TOF-PET detectors based on a monolithic scintillation crystal coupled to a photosensor array". In: *Nuclear Instruments and Methods in Physics Research Section A: Accelerators, Spectrometers, Detectors and Associated Equipment* 621.1–3 (2010), pp. 595–604. ISSN: 0168-9002. DOI: http://dx.doi.org/10.1016/j.nima.2010.05.034. URL: http://www.sciencedirect.com/science/article/pii/S0168900210011356.

[4] Yong Hyun Chung et al. "Preliminary experimental results of a quasi-monolithic detector with DOI capability for a small animal PET". In: *Nuclear Instruments and Methods in Physics Research Section A: Accelerators, Spectrometers, Detectors and Associated Equipment* 621.1–3 (2010), pp. 590–594. ISSN: 0168-9002. DOI: http://dx.doi.org/10.1016/j.nima.2010.04.039. URL: http://www.sciencedirect.com/science/article/pii/S0168900210008880.

[5] H. Liu et al. "Development of a depth of interaction detector for -rays". In: *Nuclear Instruments and Methods in Physics Research Section A: Accelerators, Spectrometers, Detectors and Associated Equipment* 459.1–2 (2001), pp. 182–190. ISSN: 0168-9002. DOI: http://dx.doi.org/10.1016/S0168-9002(00)00939-6. URL: http://www.sciencedirect.com/science/article/pii/S0168900200009396.

[6] V.V. Nagarkar et al. "Continuous Phoswich™; detector for molecular imaging". In: *Nuclear Science Symposium Conference Record (NSS/MIC), 2010 IEEE*. Oct. 2010, pp. 4–9. DOI: 10.1109/NSSMIC.2010.5873707.

[7] Tomoaki Tsuda et al. “A four-Layer depth of interaction detector block for small animal PET”. In: *Nuclear Science, IEEE Transactions on* 51.5 (Oct. 2004), pp. 2537–2542. ISSN: 0018-9499. DOI: 10.1109/TNS.2004.835739.

[8] Fumihiko Nishikido et al. “Four-layer DOI PET detectors using a multi-pixel photon counter array and the light sharing method”. In: *Nuclear Instruments and Methods in Physics Research Section A: Accelerators, Spectrometers, Detectors and Associated Equipment* 729 (2013), pp. 755–761. ISSN: 0168-9002. DOI: http://dx.doi.org/10.1016/j.nima.2013.08.031. URL: http://www.sciencedirect.com/science/article/pii/S0168900213011571.

[9] Haim Azhari, Robert R. Edelman, and David Townsend. *Multimodal Imaging and Hybrid Scanners*. Article ID 45353, 2 pages. DOI: doi:10.1155/2007/45353.

[10] BerndJ. Pichler, MartinS. Judenhofer, and Christina Pfannenberg. *Multimodal Imaging Approaches: PET/CT and PET/MRI*. English. Ed. by Wolfhard Semmler and Markus Schwaiger. Vol. 185/1. Handbook of Experimental Pharmacology. Springer Berlin Heidelberg, 2008, pp. 109–132. ISBN: 978-3-540-72717-0. DOI: doi:10.1007/978-3-540-72718-7_6. URL: http://dx.doi.org/10.1007/978-3-540-72718-7_6.

[11] Stéphane Callier et al. “EASIROC, an Easy & Versatile ReadOut Device for SiPM”. In: *Physics Procedia* 37 (2012). Proceedings of the 2nd International Conference on Technology and Instrumentation in Particle Physics (TIPP 2011), pp. 1569–1576. ISSN: 1875-3892. DOI: http://dx.doi.org/10.1016/j.phpro.2012.02.486. URL: http://www.sciencedirect.com/science/article/pii/S1875389212018688.

[12] D. Renker and E. Lorenz. “Advances in solid state photon detectors”. In: *Journal of Instrumentation* 4.04 (2009), P04004. URL: http://stacks.iop.org/1748-0221/4/i=04/a=P04004.

[13] S. Agostinelli et al. “Geant4 simulation toolkit”. In: *Nuclear Instruments and Methods in Physics Research Section A: Accelerators, Spectrometers, Detectors and Associated Equipment* 506.3 (2003), pp. 250–303. ISSN: 0168-9002. DOI: http://dx.doi.org/10.1016/S0168-9002(03)01368-8. URL: http://www.sciencedirect.com/science/article/pii/S0168900203013688.

[14] J. Allison et al. “Geant4 developments and applications”. In: *Nuclear Science, IEEE Transactions on* 53.1 (2006), pp. 270–278. ISSN: 0018-9499. DOI: 10.1109/TNS.2006.869826.

[15] Geant4. *Geant4 data libraries*. URL: http://geant4.web.cern.ch/geant4/support/datafiles_origin.shtml.

[16] CLHEP. *A Class Library for High Energy Physics*. URL: http://proj-clhep.web.cern.ch/proj-clhep/.

[17] Geant4 Low Energy Electromagnetic Physics Working Group. *Geant4 Low Energy Electromagnetic Physics*. URL: https://twiki.cern.ch/twiki/bin/view/Geant4/LowEnergyElectromagneticPhysicsWorkingGroup.

[18] Geant4. *Citations for data files distributed with Geant4*. URL: http://www.geant4.org/geant4/support/datafiles_origin.shtml.

[19] M. Janecek and William W. Moses. "Simulating Scintillator Light Collection Using Measured Optical Reflectance". In: *Nuclear Science, IEEE Transactions on* 57.3 (June 2010), pp. 964–970. ISSN: 0018-9499. DOI: 10.1109/TNS.2010.2042731.

[20] M. Janecek and William W. Moses. "Measuring Light Reflectance of BGO Crystal Surfaces". In: *Nuclear Science, IEEE Transactions on* 55.5 (Oct. 2008), pp. 2443–2449. ISSN: 0018-9499. DOI: 10.1109/TNS.2008.2003253.

[21] M. Janecek. "Reflectivity Spectra for Commonly Used Reflectors". In: *Nuclear Science, IEEE Transactions on* 59.3 (June 2012), pp. 490–497. ISSN: 0018-9499. DOI: 10.1109/TNS.2012.2183385.

[22] Inc. Saint-Gobain Ceramics & Plastics. *PreLude™ 420*. URL: http://www.detectors.saint-gobain.com/PreLude420.aspx.

[23] Jianming Chen, Liyuan Zhang, and Ren-yuan Zhu. "Large size LSO and LYSO crystal scintillators for future high-energy physics and nuclear physics experiments". In: *Nuclear Instruments and Methods in Physics Research Section A: Accelerators, Spectrometers, Detectors and Associated Equipment* 572.1 (2007). Frontier Detectors for Frontier Physics - Proceedings of the 10th Pisa Meeting on Advanced Detectors, pp. 218–224. ISSN: 0168-9002. DOI: http://dx.doi.org/10.1016/j.nima.2006.10.213. URL: http://www.sciencedirect.com/science/article/pii/S0168900206020675.

[24] NIST. *X-Ray Mass Attenuation Coefficients*. URL: http://physics.nist.gov/PhysRefData/XrayMassCoef/tab3.html.

[25] National Physical Laboratory. *X-ray absorption edges, characteristic X-ray lines and fluorescence yields*. URL: http://www.kayelaby.npl.co.uk/atomic_and_nuclear_physics/4_2/4_2_1.html.

[26] G. Audi and A. H. Wapstra. "The 1995 update to the atomic mass evaluation". In: *Nuclear Physics A* 595 (Feb. 1995), pp. 409–480. DOI: 10.1016/0375-9474(95)00445-9.

[27] N. A. Benatar, B. F. Cronin, and M. J. O'Doherty. "Radiation dose rates from patients undergoing positron emission tomography: implications for technologists and waiting areas". English. In: *European Journal of Nuclear Medicine* 27.5 (2000), pp. 583–589. ISSN: 0340-6997. DOI: 10.1007/s002590050546. URL: http://dx.doi.org/10.1007/s002590050546.

[28] A.Robert Schleipman et al. "Occupational radiation dose associated with Rb-82 myocardial perfusion positron emission tomography imaging". English. In: *Journal of Nuclear Cardiology* 13.3 (2006), pp. 378–384. ISSN: 1071-3581. DOI: 10.1016/j.nuclcard.2006.03.001. URL: http://dx.doi.org/10.1016/j.nuclcard.2006.03.001.

[29] Andrew L. Goertzen, Joon Young Suk, and Christopher J. Thompson. "Imaging of Weak-Source Distributions in LSO-Based Small-Animal PET Scanners". In: *Journal of Nuclear Medicine* 48.10 (2007), pp. 1692–1698. DOI: 10.2967/jnumed.107.040584. eprint: http://jnm.snmjournals.org/content/48/10/1692.full.pdf+html. URL: http://jnm.snmjournals.org/content/48/10/1692.abstract.

[30] *Geant4 User's Guide for Application Developers*. GEANT4 Collaboration. Dec. 2014. URL: http://geant4.cern.ch/support/userdocuments.shtml.

[31] U. Fano. "Ionization Yield of Radiations. II. The Fluctuations of the Number of Ions". In: *Physical Review* 72 (July 1947), pp. 26–29. DOI: 10.1103/PhysRev.72.26.

[32] M. Moszyriski et al. "Energy Resolution of Scintillation Detectors - New Observations". In: *Nuclear Science, IEEE Transactions on* 55.3 (June 2008), pp. 1062–1068. ISSN: 0018-9499. DOI: 10.1109/TNS.2007.908580.

[33] William W Moses. "Current trends in scintillator detectors and materials". In: *Nuclear Instruments and Methods in Physics Research Section A: Accelerators, Spectrometers, Detectors and Associated Equipment* 487.1–2 (2002). 3rd International Workshop on Radiation Imaging Detectors, pp. 123–128. ISSN: 0168-9002. DOI: http://dx.doi.org/10.1016/S0168-9002(02)00955-5. URL: http://www.sciencedirect.com/science/article/pii/S0168900202009555.

[34] Rihua Mao, Liyuan Zhang, and Ren-Yuan Zhu. "Emission Spectra of LSO and LYSO Crystals Excited by UV Light, X-Ray and -ray". In: *Nuclear Science, IEEE Transactions on* 55.3 (June 2008), pp. 1759–1766. ISSN: 0018-9499. DOI: 10.1109/TNS.2008.921877.

[35] A. Vacheret et al. "Characterization and simulation of the response of Multi-Pixel Photon Counters to low light levels". In: *Nuclear Instruments and Methods in Physics Research Section A: Accelerators, Spectrometers, Detectors and Associated Equipment* 656.1 (2011), pp. 69–83. ISSN: 0168-9002. DOI: http://dx.doi.org/10.1016/j.nima.2011.07.022. URL: http://www.sciencedirect.com/science/article/pii/S0168900211014513.

[36] REXON. *RX688 Silicon Grease*. URL: http://www.rexon.com/Scint[1].Catalog.pdf.

[37] *Geant4 Physics Reference Manual*. GEANT4 Collaboration. Dec. 2014. URL: http://geant4.cern.ch/support/userdocuments.shtml.

[38] J. Felsteiner, S. Kahane, and B. Rosner. "Effect of the electron-momentum distribution on the shape of the Compton edge of Si(Li) detectors". In: *Nuclear Instruments and Methods* 118.1 (1974), pp. 253–255. ISSN: 0029-554X. DOI: http://dx.doi.org/10.1016/0029-554X(74)90711-3. URL: http://www.sciencedirect.com/science/article/pii/0029554X74907113.

[39] D.E. Cullen, J.H. Hubbell, and L. Kissel. *EPDL97: the evaluated photo data library '97 version*. Sept. 1997. DOI: 10.2172/295438. URL: http://www.osti.gov/scitech/servlets/purl/295438.

[40] F.A. Danevich et al. "Impact of geometry on light collection efficiency of scintillation detectors for cryogenic rare event searches". In: *Nucl.Instrum.Meth.* B336 (2014), pp. 26–30. DOI: 10.1016/j.nimb.2014.06.015. arXiv: 1404.7846 [physics.ins-det].

[41] Claus Grupen and Boris Shwartz. *Particle Detectors; 2nd ed.* Cambridge monographs on particle physics, nuclear physics, and cosmology. Cambridge: Cambridge Univ. Press, 2008. ISBN: 9780521187954.

[42] O. Klein and T. Nishina. "Über die Streuung von Strahlung durch freie Elektronen nach der neuen relativistischen Quantendynamik von Dirac". In: *Zeitschrift fur Physik* 52 (Nov. 1929), pp. 853–868. DOI: 10.1007/BF01366453.

[43] Texas Instruments. *LM73: 11-14 bit Temperature Sensor*. URL: http://www.ti.com/product/lm73.

[44] Eckert & Ziegler. *High Resolution Marker 55-0-0490NMA, model MMS06-022-25u, ISO rating: C22212*. URL: http://www.ezag.com.

[45] Intersil. *EL8102 500MHz Rail-to-Rail Amplifier*. URL: http://www.intersil.com/content/intersil/en/products/amplifiers-and-buffers/all-amplifiers/amplifiers/EL8102.html.

[46] CAEN. *V792 32 Channel Multievent QDC*. URL: http://www.caen.it.

[47] DIMAX. *SUB-20 multi interface USB adapter*. URL: http://www.xdimax.com/sub20/sub20.html.

[48] W-IE-NE-R Plein & Baus GmbH. *MPOD Universal Low and High Voltage Power Supply System*. URL: http://www.wiener-d.com/.

[49] iseg Spezialelektronik GmbH. URL: http://iseg-hv.com.

[50] Yuri Musienko. "Advances in multipixel Geiger-mode avalanche photodiodes (silicon photomultiplies)". In: *Nuclear Instruments and Methods in Physics Research Section A: Accelerators, Spectrometers, Detectors and Associated Equipment* 598.1 (2009). Instrumentation for Collding Beam Physics Proceedings of the 10th International Conference on Instrumentation for Colliding Beam Physics, pp. 213–216. ISSN: 0168-9002. DOI: http://dx.doi.org/10.1016/j.nima.2008.08.031. URL: http://www.sciencedirect.com/science/article/pii/S0168900208012291.

[51] C.L. Kim. "A study on the temperature characteristics of LYSO PET detector". In: *Nuclear Science Symposium Conference Record, 2005 IEEE*. Vol. 4. Oct. 2005, p. 4. DOI: 10.1109/NSSMIC.2005.1596728.

[52] Rihua Mao, Liyuan Zhang, and Ren-Yuan Zhu. "Optical and Scintillation Properties of Inorganic Scintillators in High Energy Physics". In: *Nuclear Science, IEEE Transactions on* 55.4 (Aug. 2008), pp. 2425–2431. ISSN: 0018-9499. DOI: 10.1109/TNS.2008.2000776.

Glossary

APD avalanche photodiode. 8

CH channel. 12, 15, 60, 119, 161

DOI depth of interaction. vii, 2, 3, 6, 11, 12, 14, 16, 17, 19, 21, 26, 27, 35, 36, 40–45, 49, 50, 54–57, 62, 64, 70–73, 76, 77, 79, 80, 86–89, 94, 102, 104, 105, 107–110, 113–116, 118–120, 122, 124, 127–135, 137, 138, 163

DUT device under test. 79

ENF excess noise factor. 31

FDG fluorodeoxyglucose. 1

FOV field of view. 1, 137

FSR full scale range. 85

FWHM full width at half maximum. 23, 31, 44, 45, 55, 56, 60, 63–65, 70, 76, 78, 101–103, 105, 129, 133, 134, 137

FWTM full width at tenth maximum. 44, 45, 63, 64, 70, 76

G-APD Geiger-mode avalanche photodiode. 7–9

HPK Hamamatsu Photonics K.K.. 25, 81, 82, 167

LOR line of response. 2, 3, 5, 31, 57, 72–74, 76, 77

LUT lookup table. 20, 25

LYSO Cerium-doped Lutetium Yttrium Orthosilicate. 11, 19, 21–30, 79–82, 95, 123, 157

MMI multimodal imaging. 6

MPPC multi pixel photon counter. 7

MRI magnetic resonance imaging. 7

PCB printed circuit board. 84, 85, 167

PDE photon detection efficiency. 9, 10, 24, 25, 29, 31, 33

PET positron emission tomography. vii, 3, 5–7, 12, 13, 15, 19, 21, 31, 35, 36, 46, 57, 58, 60, 72–74, 77, 79–87, 90, 92, 95–97, 100, 101, 103, 104, 107, 111, 113, 121, 122, 130, 132, 133, 137, 138

PMT photomultiplier tube. 1, 5–8

PPK photopeak. 23, 57, 60, 81, 91–101, 103, 128

Q quadrant. 11, 12, 14, 15, 60, 112, 115–117, 119, 121, 125, 161

QE quantum efficiency. 9

ROI region of interest. 94, 95, 103

SiPM Silicon photomultiplier. vii, 3, 7–12, 15–17, 19, 21, 22, 24–26, 29, 31, 32, 35–37, 39, 40, 46, 47, 51, 79–82, 84–89, 91, 92, 94–100, 102–104, 107, 109, 112–117, 128–130, 137, 157, 159, 161, 167, 168

SQ subquadrant. 12, 14, 15, 47, 60, 117, 119, 125, 161, 163, 164

SUB-20 SUB-20 multi interface USB adapter. 86, 89, 169

TOF time of flight. 5

TOR tube of response. vii, 3, 72–77, 137, 138

Appendix A

Angular Boundaries

The fraction of the emitted photons which will be detected by a particular Silicon photomultiplier (SiPM) channel, is estimated by approximating the solid angles for all channels. These solid angles are calculated for two 2D planar models of the segmented crystal. Both planar models consist of four channels separated by reflectors as defined in figs. 2.4b and 2.4c. Formulas are derived to calculate the angular boundaries for each channel as a function of the point of emission in these 2D planar modules. Photons which are emitted within the boundaries of a particular channel will be considered as detected by that channel.

Due to difference in refractive index between the LYSO scintillator material ($n_{\text{LYSO}} = 1.81$) and the optical coupling grease ($n_{\text{coupl}} = 1.46$) a substantial amount of photons will undergo total internal reflection at the exit face of the scintillator crystal. The critical angle is given by $\theta_{crit} = \arcsin\left(\frac{n_{\text{coupl}}}{n_{\text{LYSO}}}\right) = 53.82°$. Photons emitted under an angle that, in absolute value, is in between 53.82° and 126.18°, with respect to the surface normal of the exit face of the scintillator crystal, will be totally internally reflected and are thus considered not to be detected.

A distinction is made between downwards (towards the SiPM array) and upwards oriented photons (away from the SiPM array). This distinction is made due to the upwards oriented photons presenting additional complexities as a result from multiple reflections.

A.1 Downwards Direction

For the calculation of the angular boundaries for the downwards oriented photons, the following assumptions were made:

- The reflector is considered to be a perfectly smooth reflector such that the reflected angle equals to the incident angle

- No losses at the reflective surface
- All photons emitted under an angle greater than θ_{crit} are discarded due to total internal reflection
- Downward photons are not reflected back into the upward direction

In fig. A.1 a diagram is shown to aid in calculating the various angular boundaries. The red area of the circle indicates the angles under which the photons will undergo total internal reflection and thus are unable to exit the crystal array. The green areas correspond to photons that can exit the crystal array. Photons emitted under angles that fall in the white areas will be reflected on the small areas of the top of the reflectors that segment the crystal. As can be seen from fig. A.1 the white areas contribute only a negligible portion of the total number of photons, and thus can can safely be neglected.

Based on the diagram in fig. A.1 one can easily obtain the angles that mark the white areas from the following formula

$$\alpha = \arctan\left(\frac{q_2 - y}{q_1 - x}\right) . \tag{A.1}$$

By replacing the locations for each of the top corners from the three reflectors into $\vec{Q} = (q_1, q_2)$, six angles will be obtained leading to the three white areas.

To find the angular boundaries in the case of a reflection, an arbitrary emission point $\vec{P} = (x, y)$ is chosen in the upper half of the crystal. Due to symmetry considerations, the lower half of the crystal behaves in an identical way. To find the angles under which the photons need to be emitted to be reflected at $\vec{A} = (a_1, a_2)$ and eventually reach $\vec{Q} = (q_1, q_2)$ can be found with the following equations,

$$\vec{A} = \vec{P} + l \cdot (\cos(\alpha), \sin(\alpha)) , \tag{A.2}$$

$$\vec{Q} = \vec{A} + k \cdot (\cos(-\alpha), \sin(-\alpha)) , \tag{A.3}$$

$$\vec{Q} - \vec{P} = l \cdot (\cos(\alpha), \sin(\alpha)) + k \cdot (\cos(-\alpha), \sin(-\alpha)) . \tag{A.4}$$

From eq. (A.4) we obtain the following set of equations:

$$q_1 - x = (l + k) \cdot \cos(\alpha) , \tag{A.5}$$

$$q_2 - y = (l - k) \cdot \sin(\alpha) . \tag{A.6}$$

Dividing eq. (A.6) by eq. (A.5) yields:

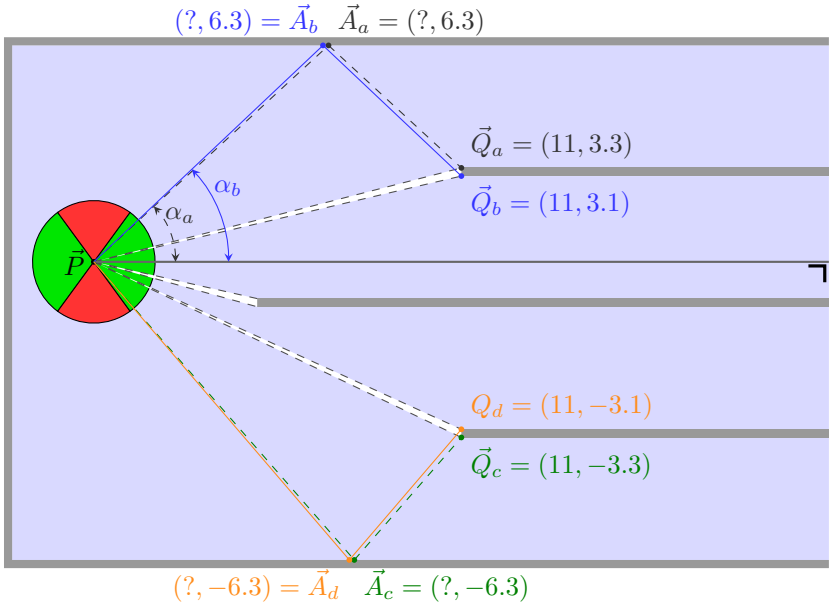

Figure A.1: Diagram used to calculate the various angular boundaries associated to each SiPM channel for the photons that are initially emitted into the downwards direction. The range of angles shown in red correspond to photons which will be totally internally reflected at the exit face and thus remain trapped inside the crystal.

$$\tan\alpha = \frac{q_2 - y}{q_1 - x} \cdot \frac{l + k}{l - k} \ . \tag{A.7}$$

From fig. A.1 it is clear that the y-coordinates of $\vec{A}$ and $\vec{Q}$ are known because they are situated on features of the crystal structure. This allows to solve eq. (A.7) by substituting l and k in terms of a_2 and $\vec{Q}$ as follows

$$l \cdot \sin\alpha = a_2 - y \ , \tag{A.8}$$

$$-k \cdot \sin\alpha = q_2 - a_2 \ , \tag{A.9}$$

resulting in eq. (A.7) becoming

$$\tan\alpha = \frac{q_2 - y}{q_1 - x} \cdot \frac{a_2 - y - q_2 + a_2}{a_2 - y + (q_2 - a_2)} \ , \tag{A.10}$$

$$\alpha = \arctan\left(\frac{2 \cdot a_2 - y - q_2}{q_1 - x}\right) \ . \tag{A.11}$$

By replacing the values for $\vec{P}$, $\vec{A}$ and $\vec{Q}$ into eq. (A.11) as shown in fig. A.1 it is possible to calculate the angular boundaries for each channel for a particular

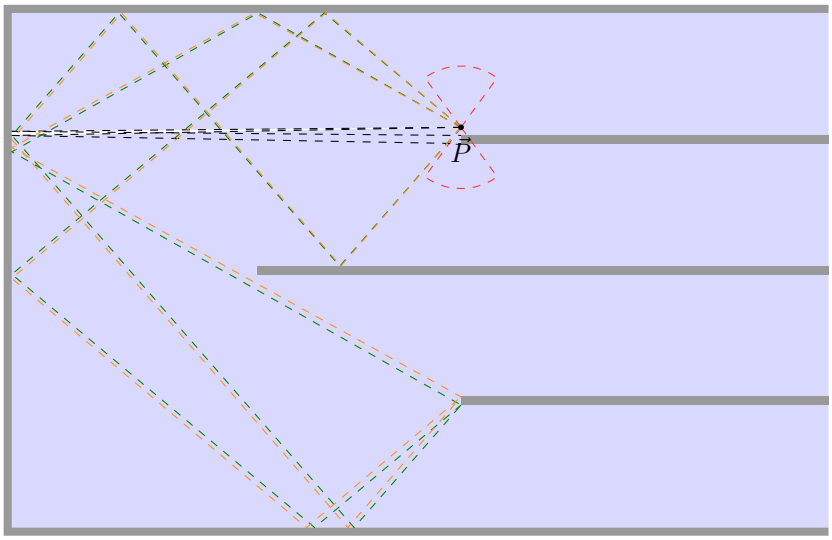

Figure A.2: Illustration of some of the possibilities for multiple reflections.

emission point $\vec{P}$. The white areas in fig. A.1 were drawn by calculating the angles using eq. (A.11).

A.2 Upwards Direction

The upwards direction is considerable more complicated due to the possibility for the photons to undergo multiple reflections before being detected. In particular, the following list and in fig. A.2 presents some of the complexities introduced due to the possible ways the upwards photons can reflect:

- Single reflection: Photon goes upwards, but the angle after reflection is too shallow to lead to an additional reflection on one of the sides of the crystal structure (black dashed lines in fig. A.2)
- Double reflection (orange and green lines in fig. A.2):
  - First reflection is on the crystal entry surface while the second reflection is on a side wall of one of the reflector of the crystal structure
  - First reflection is on a side wall of one of the reflector of the crystal structure while the second reflection is on the entry surface of the crystal structure.

The complexities these various types of reflections introduce are presented in fig. A.2. Accounting for all the variations of reflections in calculating the solid angles quickly becomes problematic. As a result, another approach is taken for the upwards directed photons.

The fraction of the solid angle corresponding to the upwards directed photons is divided over the various elements (quadrant (Q), subquadrant (SQ), channel (CH)). For each point of emission, the layer in which the emission point is situated is determined. Depending in which layer and element the emission point is situated, a particular division of the solid angle is made.

Layer 1 The solid angle is divided equally over all the channels, i.e. 25 % each.

Layer 2 55 % of the solid angle is divided equally over the channels which are part of the quadrant in which the point of emission was situated. The remainder of the solid angle (45/2 % per channel) is spread out equally over the two channels of the other quadrant.

Layer 3 65 % of the solid angle is limited to the channel above which the emission point is situated. The remainder of the solid angle (35/3 %) is spread out equally over the other three channels.

Layer 4 80 % of the solid angle is limited to the channel above which the emission point is situated. The remainder of the solid angle (20/3 %) is spread out equally over the other three channels.

A.3 Downwards and Upwards Combined

The ratios defined in eqs. (2.5) to (2.7) are calculated for a wide range of locations of the emission points over the 2D planar models. For each emission point and each 2D model, the fraction of light detected by each channel is calculated by summing the solid angle, using the methods described before, corresponding to the channel and dividing it by the full solid angle. This yields 4 values for each 2D planar module.

To convert these values for the 2D models to a 3D model, these values are multiplied with each other to obtain 4×4 new values, each one corresponding to a single channel of the SiPM array. These 16 values are then used to determine the channel which has the largest fraction of detected photons (CH_{max}), the Q (SQ) with the maximum sum Q_{max} (SQ_{max} resp.) and $SQ_{neighbour}$ being the neighbouring SQ of SQ_{max}. From these obtained values for CH_{max}, Q_{max}, SQ_{max}, and $SQ_{neighbour}$, the ratios are then calculated.

After this procedure, the values the ratios are plotted, shown in fig. 2.5, as a function of the point along the depth of the segmented crystal.

Appendix B

Center of Gravity: Details

It was demonstrated in chapter 4 that the center of gravity calculation for the (X, Y) position exhibit severe aftifacts. In this appendix, the relationship between the generated and calculated mean positions X and Y is discussed in more detail.

Figure B.1 presents the correlation between the reconstructed and generated mean positions X and Y. To this end the calculated X v.s. the generated X position of the generated emission point, is plotted in fig. B.1a while fig. B.1b shows the results for Y. The difference in these correlations between X and Y are attributed to the asymmetry in segmentation of the third layer for the depth of interaction (DOI) encoded crystal.

The calculated mean for the Y position remains mostly constant around $\pm 1.5\,\text{mm}$ which closely corresponds to the channel center at 1.6 mm along the Y direction (e.g. channel 10 shown in fig. 4.3c). The calculated X mean on the other hand has a clear change while the point of emission moves over the boundary between the 2 SQs. Unfortunately, for both X and Y the relation between the generated and calculated position is a multivalued function. As a result, one can not unambiguously make corrections to the mean calculated positions to reduce the error.

To understand where this multivalued function, shown in figs. B.1a and B.1b, originate from, the mean of X (Y) versus X (resp. Y) are plotted for 1 mm steps along the depth of the crystal. The results are shown in fig. B.2 (resp. fig. B.3). As a reminder, the depth for each of the 4 layers is as follows:

Layer 1: $0\,\text{mm} \leq Z < 6\,\text{mm}$, i.e. figs. $1 \rightarrow 6$

Layer 2: $6\,\text{mm} \leq Z < 11\,\text{mm}$, i.e. figs. $7 \rightarrow 11$

Layer 3: $11\,\text{mm} \leq Z < 16\,\text{mm}$, i.e. figs. $12 \rightarrow 16$

Layer 4: $16\,\text{mm} \leq Z < 20\,\text{mm}$, i.e. figs. $17 \rightarrow 20$

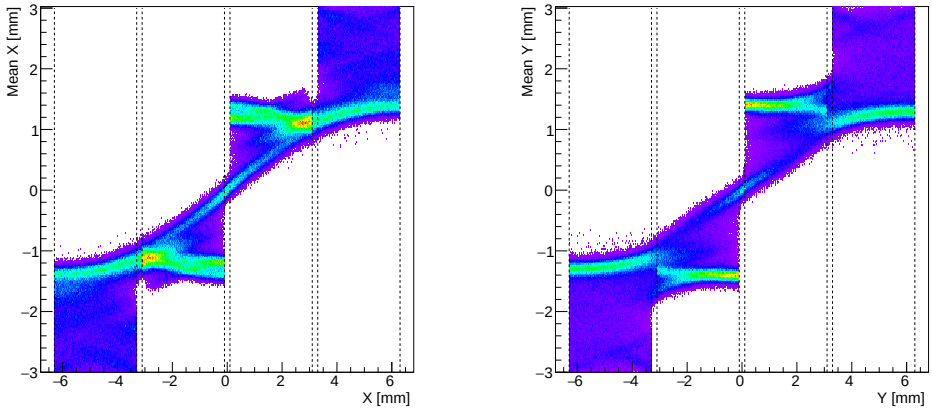

(a) **(b)**

Figure B.1: Calculated mean positions as a function of the position of emission. (a) X direction, (b) Y direction. Black dashed lines are added at the locations of the channel edges to provide points of reference.

In the top part of the first layer there is a nearly linear dependence of the mean position on the point of emission. However as the emission point gradually occurs deeper in the crystal, a knee in the distribution comes into existence which gradually moves towards the center of the module.

Once the emission point approaches the interface between layer 1 and 2 (figs. 6 and 7) the knee nearly disappears before flipping upside down. While the emission point occurs deeper into the second layer the upside down knee moves away from the center. Unfortunately due the upside down knee there is an overlap in calculated mean X for emission points originating near the center of the module versus the outer region. This means that there is no reliable method to determine where the point of emission is situated. On the other hand, the calculated mean Y remains nearly constant over the entire Y range, but it gravitates towards the center of the innermost channel.

Near the interface of layer 2 and 3 (figs. 11 and 12) the calculated mean X shows a distinct split at the border of the innermost and outermost channels. This allows to place the point of emission at either the center of an inner- or outermost channel depending on the value of the mean X. For the mean Y on the other hand this clear split is absent until the emission point approaches the interface between layer 3 and 4, which is consistent with the segmentation of the SQ in the third layer.

Both for the calculated mean X and Y there is a clear distinct split in layer 4, making it straightforward to determine above which channel the emission point is situated.

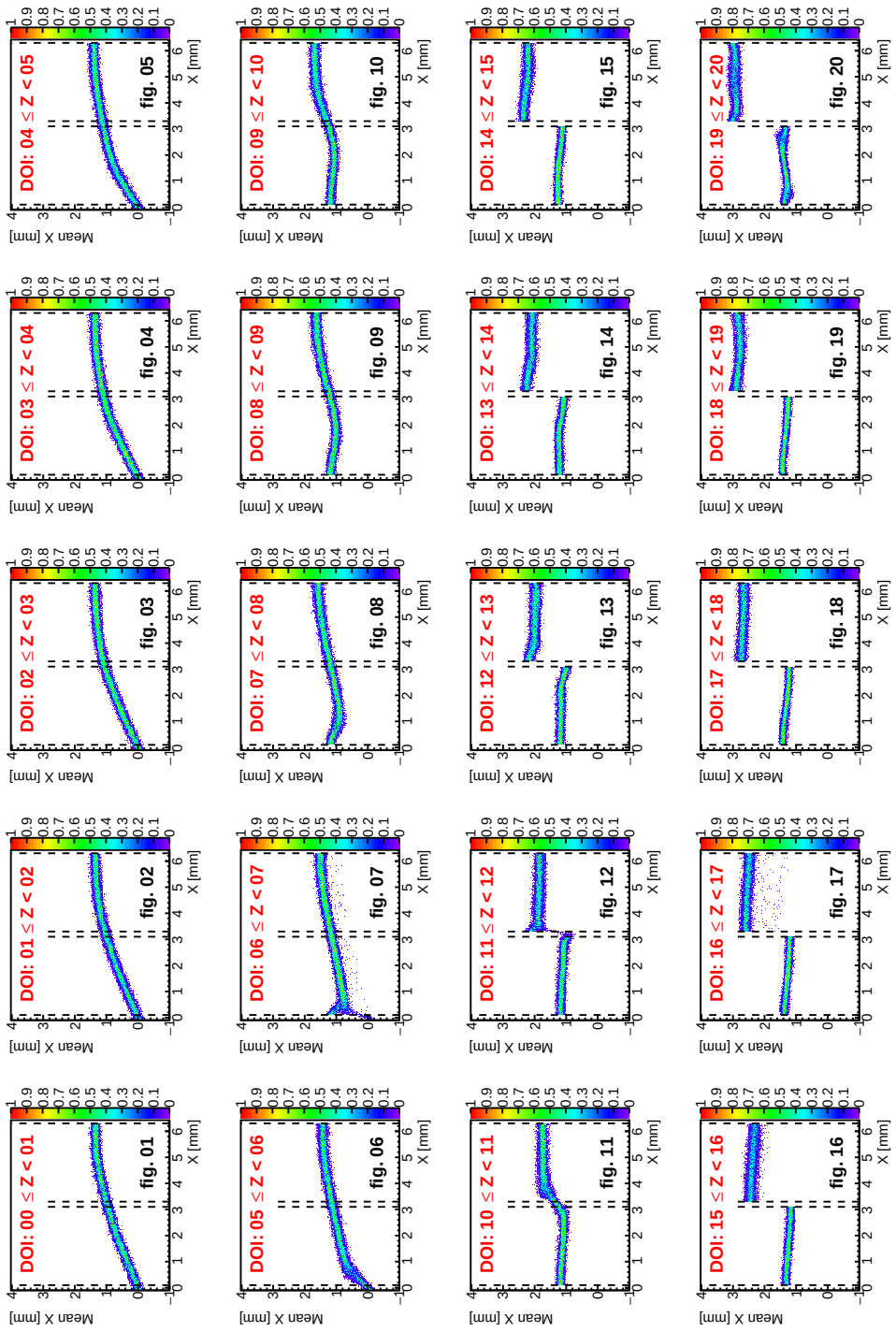

Figure B.2: Calculated mean X positions in function of the position of emission in 1 mm steps along the depth (Z) of the crystal.

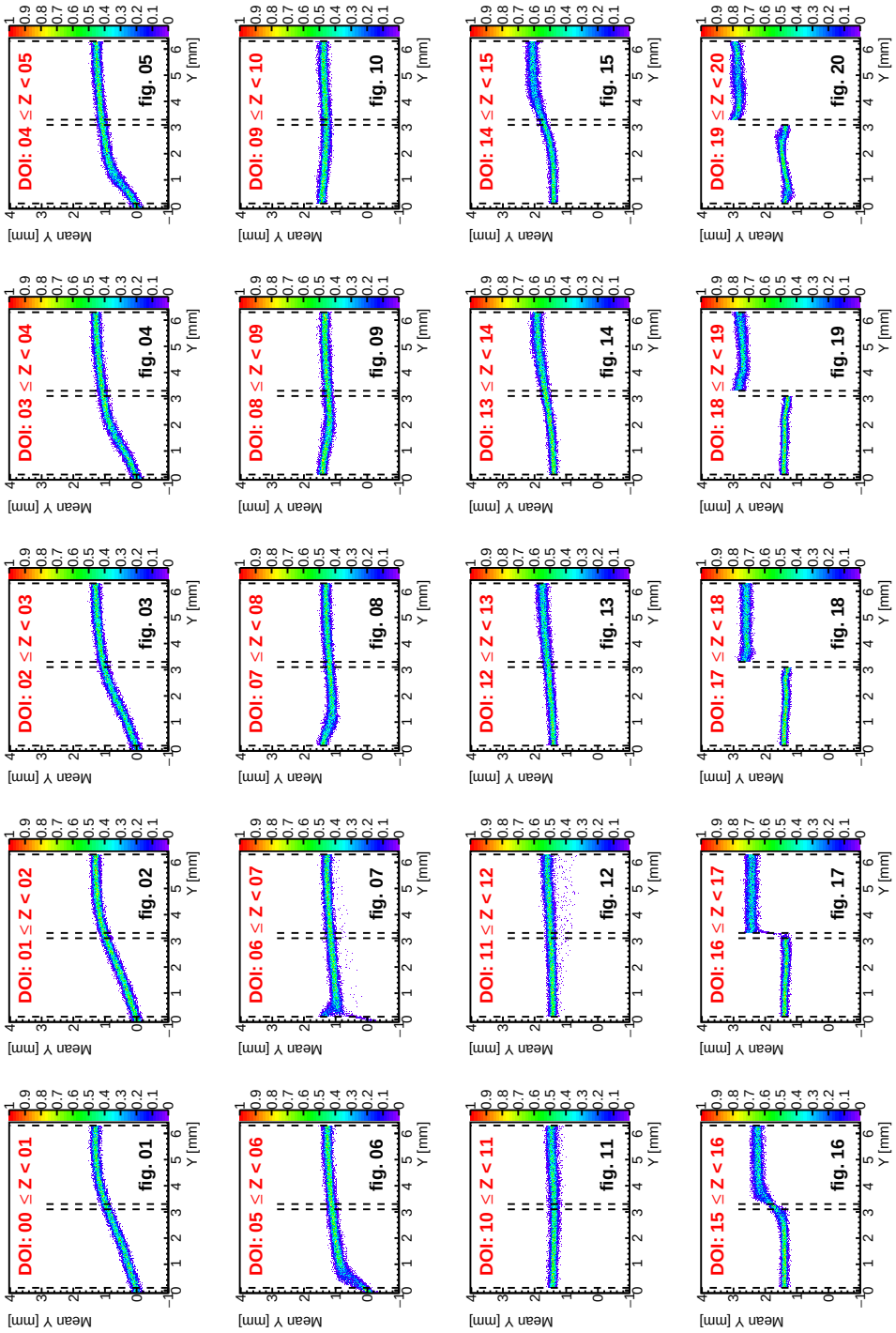

Figure B.3: Calculated mean Y positions in function of the position of emission in 1 mm steps along the depth (Z) of the crystal.

Appendix C

SiPM Array Details

This appendix lists details of the SiPM array that was used in the measurements. The recommended bias V_o and dark currents I_d are provided by the producer for each individual SiPM. In addition, a layout of the channels and their mapping to the signal lines of the flat flexible cable are provided as well.

The SiPM array was calibrated by HPK and for each SiPM channel of the array, a recommended operating bias was determined. The recommended operating bias V_{op} was estimated as the bias for which the gain of the channel was in the range of M =6.5–8.5 $\times 10^5$. These calibrations were performed at a temperature of 25 °C.

The data provided by HPK is presented in fig. C.1 in a schematic resembling the physical layout of the SiPM array. Each SiPM channel in the figure is marked with the channel ID, its recommended bias V_o, and its dark current I_d.

From the data provided by HPK, the mean value of the recommended operating bias was determined to be V_{op} = 72.29 V with RMS spread of 0.05 V. Considering that during most of the measurements the temperature remained mostly in the range of 23 °C to 24 °C, the applied bias during the measurements was kept in the neighbourhood of the mean recommended bias V_{op}.

In fig. C.1, the flat cable is illustrated on the right hand side of the figure. It illustrates how the SiPM channels are mapped to the signal extraction, SiPM array → amplifier PCB → CAEN V792.

In section 6.5.3 the remapping of the channels of the array was discussed, this appendix provides more details regarding the channel remapping. Similarly, the remapped channels are shown in white, i.e. the bottom two rows, while their original (remapped) mappings are marked with red (green resp.) numbers. The remapping of the channels are also indicated next to the flat cable outputs, see the right hand side of fig. C.1.

The SiPM array also has an LM73 temperature sensor mounted to the back side of the device. It is an I^2C device which requires a separate readout

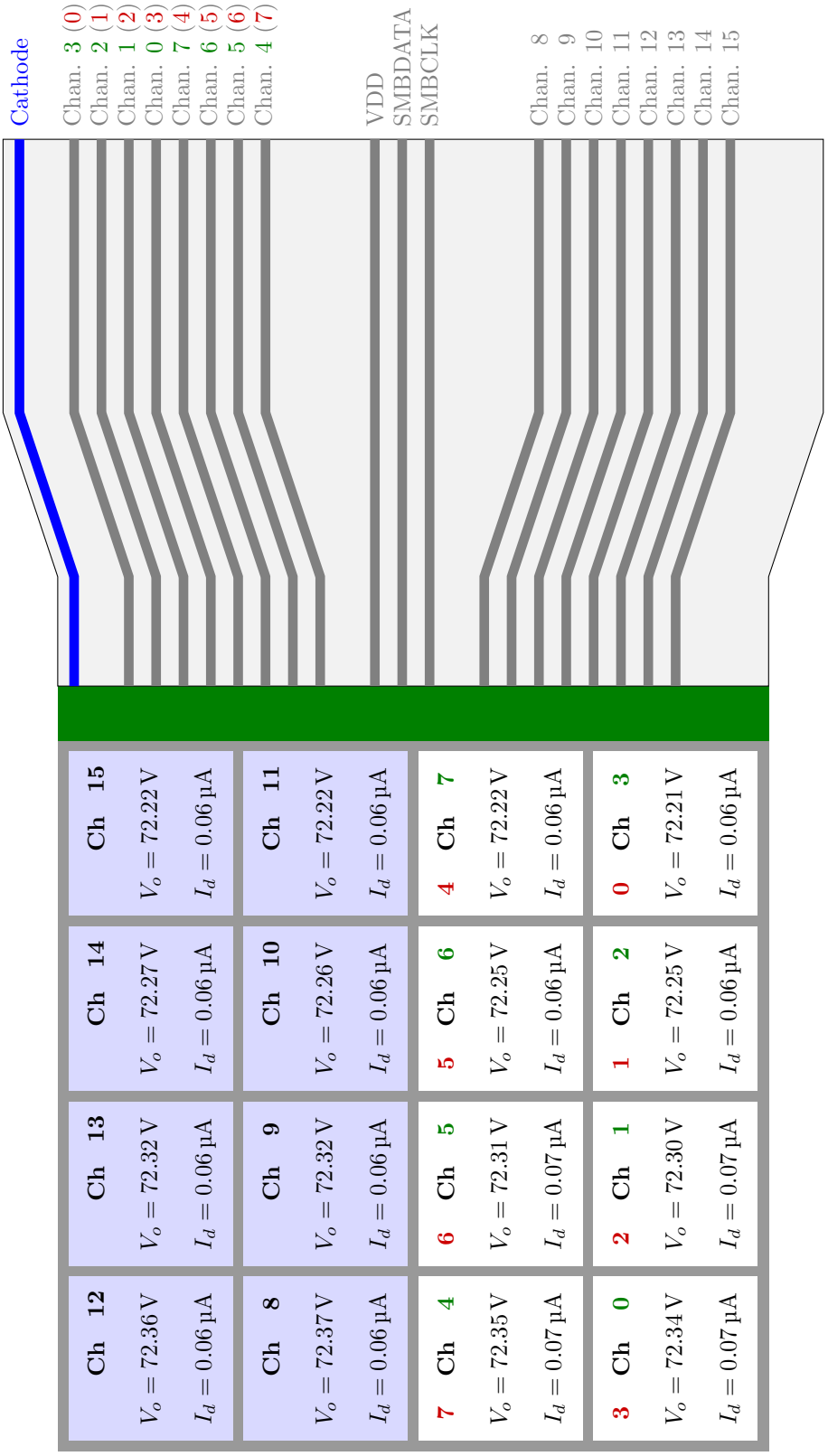

Figure C.1: Schematic of the SiPM array with details regarding the recommended V_o and I_d for each individual SiPM channel. Remapped SiPM channels are represented by white squares with their original channel IDs given in red and their remapped IDs in green.

from the general digital acquisition. Three lines on the flat cable are reserved for the communication with the temperature sensor.

The line VDD is reserved to deliver power (VDD) to the device and is provided by the SUB-20 adapter. SMBDATA and SMBCLK are for the communication with the sensor. The SMBCLK clock line is takes a clock signal, provided by SUB-20, while data is send over the SMBDATA line.